HAFNIA-RICH MIXED OXIDE CERAMICS OF THE SYSTEM HfO_2-ZrO_2-TiO_2 FOR HEATERS AND HEAT EXCHANGERS IN ELECTROTHERMAL THRUSTERS

Final Report, Vol. I
NAG 3-495

The Effects of Titania on Selected Electrical and Mechanical Properties of Hafnia-Rich Mixes Oxides in the System Hafnia-Zirconia-Titania

by

P. R. Staszak, G. P. Wirtz, M. Berg and S. D. Brown

Department of Materials Science and Engineering
204 Ceramics Building
105 So. Goodwin Avenue

University of Illinois at Urbana-Champaign
Urbana, IL 61801

May 1988

THE EFFECTS OF TITANIA ON SELECTED ELECTRICAL AND MECHANICAL PROPERTIES OF HAFNIA-RICH MIXED OXIDES IN THE SYSTEM HAFNIA-ZIRCONIA-TITANIA

Paul Russell Staszak, Ph.D.
Department of Ceramic Engineering
University of Illinois at Urbana-Champaign, 1988

ABSTRACT

A study of the effects of titania on selected properties of hafnia-rich mixed oxides in the system hafnia-zirconia-titania (HZT) was made in the region 5 to 20 mol% titania. The studied properties included electrical conductivity, thermal expansion, and fracture strength and toughness. The electrical conductivity was measured using a two-point probe with 10 kHz ac current on bars over the temperature range 400 to 1700°C and oxygen partial pressure range 10^{-31} to 21 kPa (10^{-33} to 0.21 atm). The thermal expansion was measured using a dilatometer from room temperature to 1700°C. Fracture strengths were determined using a four-point bend fixture on nonindented bars at room temperature and on triple Vickers indented bars at room temperature, 1000°C, and 1400°C. Fracture toughness (K_{1c}) values were also determined from the indented bars.

The effects of titania on the properties were studied for the reduced state as well as the oxidized state of the sintered mixed oxides. X-ray analyses showed that the materials were not always single phase. The oxidized compositions went from being monoclinic solid solutions at low titania additions to having three phases (two monoclinic and a titanate phase) at high additions of titania. The reduced compositions showed an increasing cubic phase presence mixed with the monoclinic phase as titania was added. The grains of all the samples were nominally 1 μm. Microcracking regions varying from 16 μm to 3000 μm were also observed in the

microstructures. The wide variability in phases and microcracking regions accounted for the majority of the observed property trends.

The electrical conductivity increased with temperature to approximately 10^{-1} mhos/cm at 1700°C for all compositions. For low temperatures at high oxygen partial pressures, higher concentrations of titania lowered the conductivity suggesting that the titanium ions go into interstitial positions thereby reducing oxygen ion conductivity. For all temperatures at low oxygen partial pressures, the materials became highly anion deficient leading to higher conductivities suggesting that Ti^{4+} is being converted to Ti^{3+} and Ti^{2+} thereby enhancing electronic conductivity.

The thermal expansion coefficient decreased with increasing titania (6.2×10^{-6}/°C at 5 mol% to 5.0×10^{-6}/°C at 20 mol% titania) as did the monoclinic to tetragonal transformation temperature. A hysteresis between the heating and cooling curves in the 15 and 20 mol% compositions suggested extensive microcracking. The low thermal expansion coefficient of the second phase titanate partially accounted for the decrease in thermal expansion in these higher titania compositions.

The fracture strength of the oxidized bars tended to decrease with the addition of titania owing to the presence of the second phase titanate. The fracture strengths of the reduced bars exhibited a minimum corresponding to a two-phase region of monoclinic and cubic phases. When the second phases were suppressed, the titania tended to increase the fracture strength slightly in both the oxidized and reduced states. The fracture toughness followed similar trends.

TABLE OF CONTENTS

1. INTRODUCTION

Hafnia-rich mixed oxides in the system hafnia-zirconia-titania (HZT) possess many properties which are ideal for a number of applications including heat exchangers, electrothermal thrusters, and fuel cells. They have high melting temperatures (>2200°C), moderate (< 4 x 10^{-6}/°C) to zero thermal expansion coefficients, and high thermal shock resistance.[1-5] Owing to their similarity to hafnia and zirconia (they are isomorphous), they possess the potential to exhibit many of the property benefits of their parent oxides. Among these benefits are good high-temperature electrical conductivity and strength.

The high electrical conductivity of zirconia (>10^{-2} mhos/cm at temperatures above 800°C) and its remarkable strengths (>300 MPa) have led to many studies of the electrical and mechanical properties of materials with the fluorite structure. Included among these studies have been investigations of the properties of hafnia, zirconia, and their binary system. In addition, the effects on the properties of various additives to these materials have been examined in an effort to improve the material characteristics. Included among the list of additives that have been investigated is titania.

From studies of the zirconia-hafnia system, the material properties have been shown to follow the rule of mixtures (i.e., the properties of the mixtures vary proportionally to the amounts of the pure phases present). Such a correlation would be expected since hafnia and zirconia form a complete solid solution with one another. From studies of the zirconia-titania and the hafnia-titania systems, solid solutions have been shown to result with additions of several mole percent titania. Beyond the solubility limit, a titanate phase forms. The effect of titania in these systems has been to increase the electrical conductivity, lower the thermal expansion, and increase the strength. In the regions of the phase diagram where the titanate phase is present, the strength of the material has been observed to decrease with titania additions.

Although the HZT system has been investigated by several authors[1-5], a thorough study of the entire system has never been made. Solid solutions have been shown to exist in the hafnia-rich region of the ternary system; however, the amount of titania as well as the processing parameters govern whether the material remains a solid solution or becomes a mixture of a titanate phase in a monoclinic solid solution. The amount of titania also affects whether the system will duplicate the properties of its parent oxides. The exact effect of titania in the HZT system and the effect of titania on the electrical and mechanical properties of the system are two areas this research examines.

2. LITERATURE REVIEW

This review will be divided into two sections. The first will examine the structure and systems of hafnia, zirconia, and titania. The second will survey selected electrical and mechanical properties in the systems; namely, electrical conductivity, thermal expansion, and fracture strength and toughness. From the review, certain insights and knowledge of the effects that titania has on the structure and properties in the HZT system will be gained.

2.1 Structure and Systems of Hafnia, Zirconia, and Titania

2.1.1 Structure

Three crystalline structures are encountered in the systems of hafnia, zirconia, and titania. They are the fluorite, the rutile, and the titanate. The more important of the three in the hafnia-rich region of the HZT system are the fluorite and the titanate structures.

2.1.1.1 Fluorite

Both hafnia and zirconia have distorted fluorite crystal structures whereas titania has the rutile structure. From considerations of ionic radii and Pauling's rules, however, all three oxides should have the rutile structure.[6] Most AX_2 compounds with high cation to anion radius ratios (approaching 1.0) have the fluorite structure, while those with intermediate ratios (0.43 to 0.73) have the rutile structure and those with low ratios (< 0.4), one of the silica structures.[7] The difference in the structures lies in the coordination of anions to cations. For the fluorite structure, there is eightfold coordination. For the rutile structure the coordination is sixfold, and for the silica structures, fourfold. Cation to anion radius ratios for typical fluorite structures are CeO_2 0.68, UO_2 0.70, ThO_2 0.75, CaF_2 0.84, HgF_2 0.88, SrF_2 0.94, etc..[7] Table 1 shows the ionic radii for hafnia, zirconia, and titania along with the cation to anion

radius ratios, coordination numbers, and crystal structures. Even though ionic radius ratios suggest the opposite, the degree of covalency that exists in HfO_2 and ZrO_2 apparently causes the fluorite structure to be more stable than the rutile.[8] Covalency in the structure was suspected to exist due to the sevenfold coordination of anions about cations in the low temperature monoclinic phase. Although the degree of covalency in the monoclinic phase of the ZrO_2 fluorite structure was not calculated, the covalency of the high temperature forms was found to be 28 and 22%, respectively, for the tetragonal and cubic phases.[7] The monoclinic form should have a similar degree.

Table 1. Ionic Radii, Radius Ratios, Coordination Numbers, and Crystal Structures for HfO_2, ZrO_2, and TiO_2.

Ion	Ionic Radii (Ref. 9)			M^{4+}/O^{2-}			Crystal
	8CN	7CN	6CN	8CN	7CN	6CN	Structure
Hf^{4+}	.83	.76	.71	.58	.54	.51	Fluorite
Zr^{4+}	.84	.78	.72	.59	.56	.51	Fluorite
Ti^{4+}	.74	-	.605	.52	-	.43	Rutile
Ti^{3+}	-	-	.810				
Ti^{2+}	-	-	1.00				
O^{2-}	1.42	-	1.40				

As mentioned, three polymorphs of fluorite exist for HfO_2 and ZrO_2. The low temperature phase is monoclinic. The higher temperature phases are tetragonal and cubic. Figure 1 shows the three polymorphic phases of the fluorite structure.

The monoclinic phase is stable at all temperatures below 1650°C for HfO_2 and 1170°C for ZrO_2. The coordination of anions about cations is sevenfold having a range of bond lengths and angles. Triangularly coordinated and distorted tetrahedrally coordinated O-M^{4+} layers with different thicknesses result.[8] The lattice sites of monoclinic ZrO_2 are shown in Figure 2. The movement off normal fluorite positions can be seen. HfO_2 (being isomorphous with ZrO_2) has a similar lattice configuration.

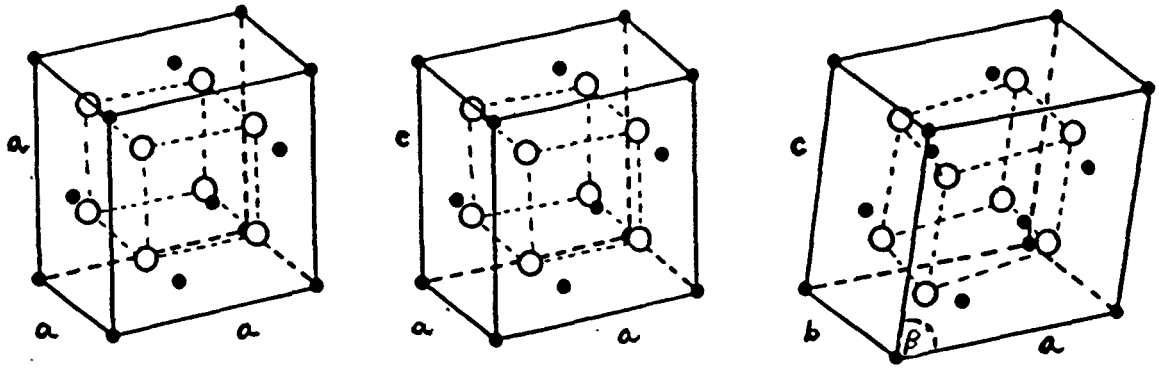

(a) (b) (c)

Figure 1. Polymorphic phases of the fluorite structure (a) cubic, (b) tetragonal, and (c) monoclinic. Solid circles: Zr^{4+}. Open circles: O^{2-} (Ref. 7).

The tetragonal phase is stable at temperatures between 1650°C and 2700°C for HfO_2 and 1170°C and 2370°C for ZrO_2. The monoclinic to tetragonal transformation has a thermal hysteresis of approximately 200°C between heating and cooling. The coordination of anions to cations is eightfold with two sets of four oxygens at slightly different bond lengths.[8] Figure 3 shows the tetragonal lattice sites.

The cubic phase is stable above 2700°C for HfO_2 and 2370°C for ZrO_2 to their respective melting temperatures, 2900°C and 2680°C. Eightfold coordination exists having equidistant cation-anion bond lengths. The lattice sites of the cubic fluorite structure are shown in Figure 4. The slight distortion from the ideal fluorite structure is illustrated.

The lattice parameters of the three polymorphs of HfO_2 and ZrO_2 are given in Table 2. Also included are the cell volumes and theoretical densities.

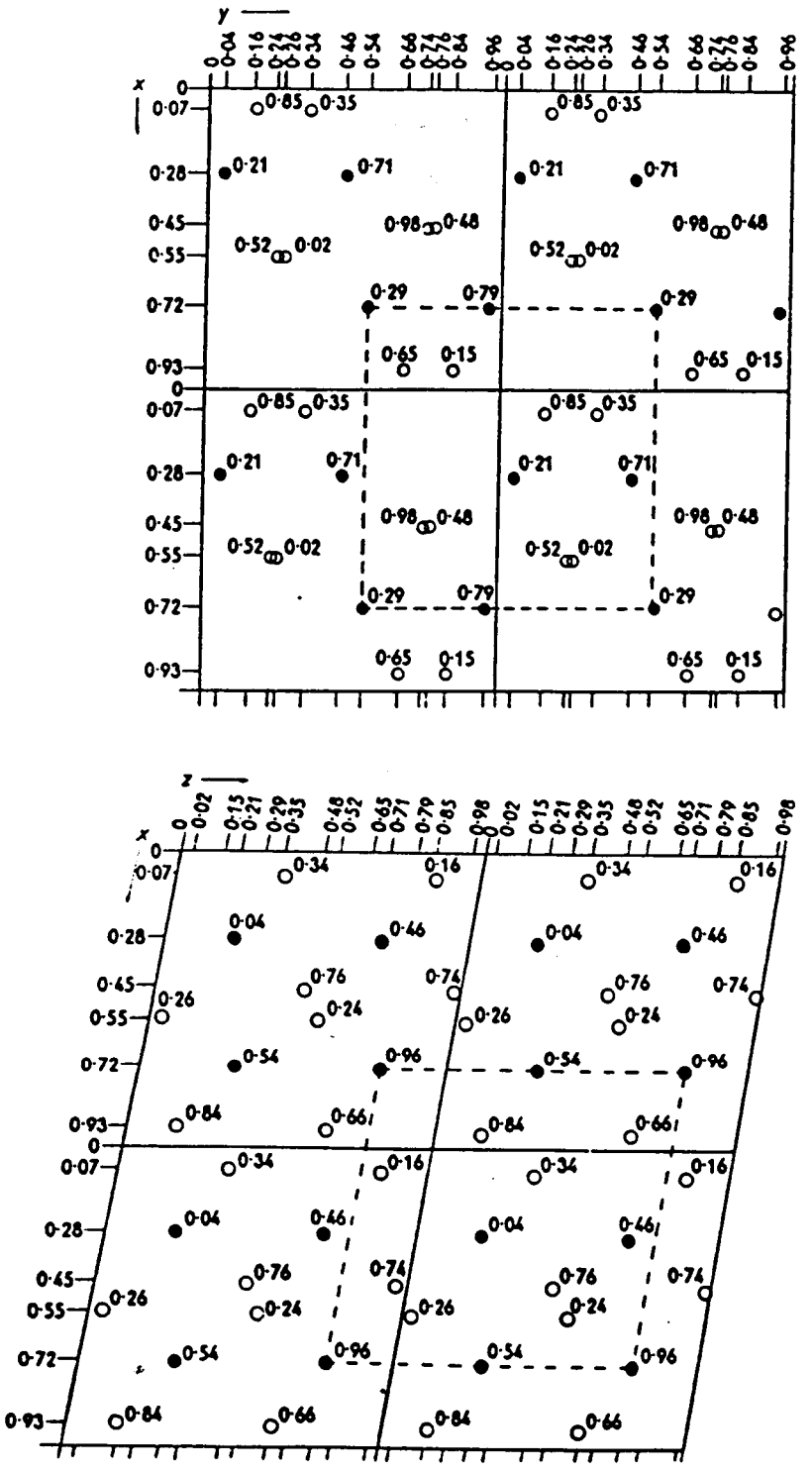

Figure 2. Lattice positions of the monoclinic cell of ZrO_2. Solid circles: Zr^{4+}. Open circles: O^{2-}. Broken lines become tetragonal cell after transformation (Ref. 10).

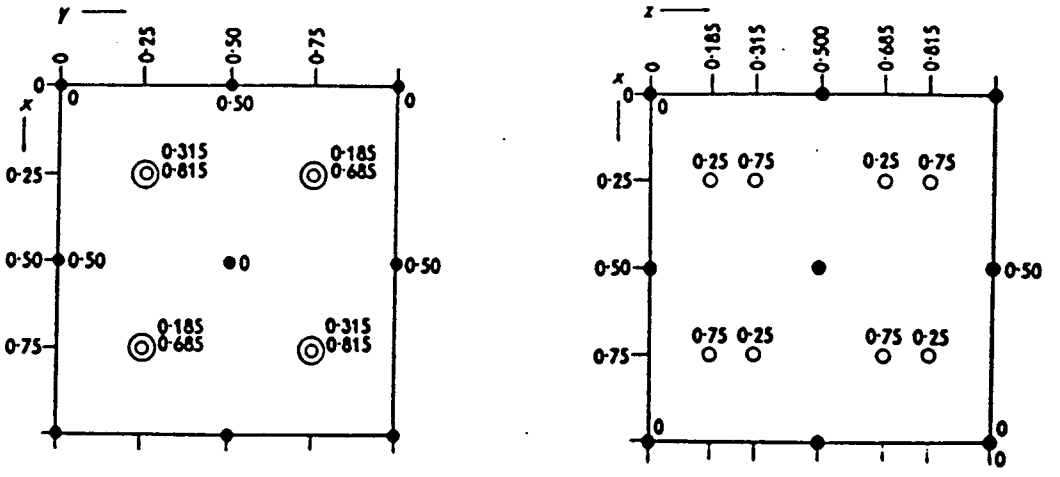

Figure 3. Lattice positions of the tetragonal cell of ZrO_2. Solid circles: Zr^{4+}. Open circles: O^{2-} (Ref. 10).

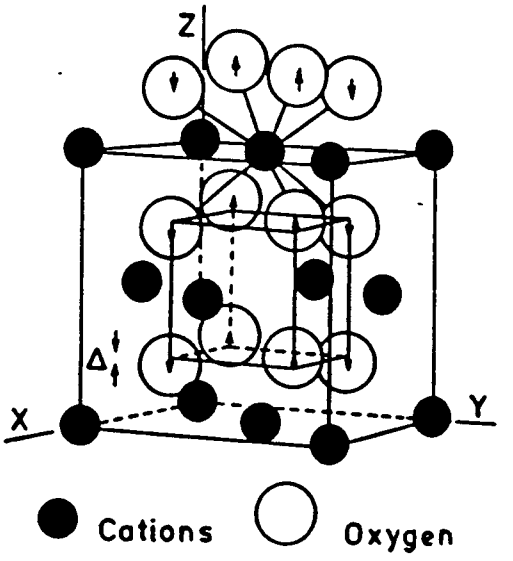

Figure 4. Distortion of cubic lattice sites of ZrO_2 from ideal fluorite crystal structure (Ref. 8).

Table 2. Summary of Lattice Parameters for HfO_2, ZrO_2, TiO_2, $HfTiO_4$, and $ZrTiO_4$.

	Phase	a (Å)	b (Å)	c (Å)	ß (degrees)	V (Å^3)	ρ (g/cm^3)	Measurement Temperature	Ref.
HfO_2	m	5.116	5.172	5.295	99.18°	138.3	10.11	RT	11
	t	5.140		5.25		138.7	10.08	1865°C	12
	c	-				-	-	-	-
ZrO_2	m	5.145	5.208	5.311	99.23°	140.5	5.826	RT	11
	t	5.166		5.298		141.4	5.790	1400°C	13
	c	5.070				130.3	6.283	RT	14
TiO_2	t	4.5933		2.9592		62.43	4.250	RT	15
$HfTiO_4$	o	4.750	5.043	5.573		133.5	7.223	RT	16
$ZrTiO_4$	o	4.806	5.032	5.447		131.7	5.123	RT	17

2.1.1.2 Titanate

In the study of the hafnia-rich portion of the HZT system, the fluorite structure plays a main role since it tends to be the dominating phase structure. The rutile structure, on the other hand, is not encountered. Therefore, an elaboration of the structure is not warranted in this review. A structure that is encountered, however, is that of the titanate phase. Beyond the solubility limit of titania in monoclinic solid solutions of hafnia and zirconia, hafnium titanate and zirconium titanate form as second phases. The titanate phases will presently be discussed for completeness of the structure review.

Figure 5 shows the titanate crystal structure. The unit cell is orthorhombic with sixfold coordination of anions about cations. Lattice parameters and unit cell volumes for $HfTiO_4$ and $ZrTiO_4$ are given in Table 2. The $HfTiO_4$ solid solution range is between 35 and 55 mol% titania at room temperature and is stable to 1980°C.[18] The $ZrTiO_4$ solid solution range is 42 to 50 mol% titania and extends to 1900°C.[19]

2.1.2 Systems

Several investigations of the three binary systems of the HZT ternary have been

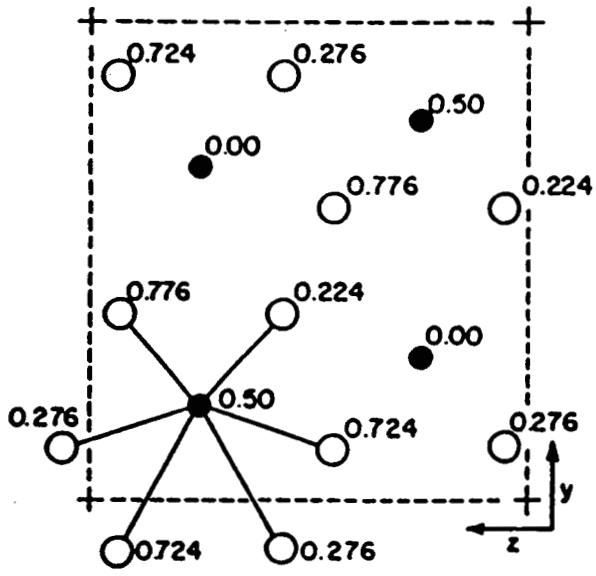

Figure 5. Lattice positions in the titanate crystal structure. Open circles: O^{2-}. Solid circles: Zr^{4+} (Ref. 20).

made. A thorough investigation of the ternary, however, has never been done. Nonetheless, a good deal of insight into the ternary can be gained from information on the solubility limits, two-phase regions, and phase transformations of the binaries.

2.1.2.1 HfO_2-ZrO_2

Hafnia and zirconia form a complete solid solution with one another.[12,21-22] The zirconium ions substitute homogeneously and directly for the hafnium ions in the fluorite structure.[22] As zirconia is added, the lattice parameters increase smoothly,[22] the densities decrease,[21] and the monoclinic to tetragonal, tetragonal to cubic, and cubic to liquid transformation temperatures decrease.[22] Figure 6 is the binary HfO_2-ZrO_2 phase equilibrium diagram constructed by Ruh et. al..[22] The triangles in the diagram represent the experimental liquid to cubic transformation temperature. (The

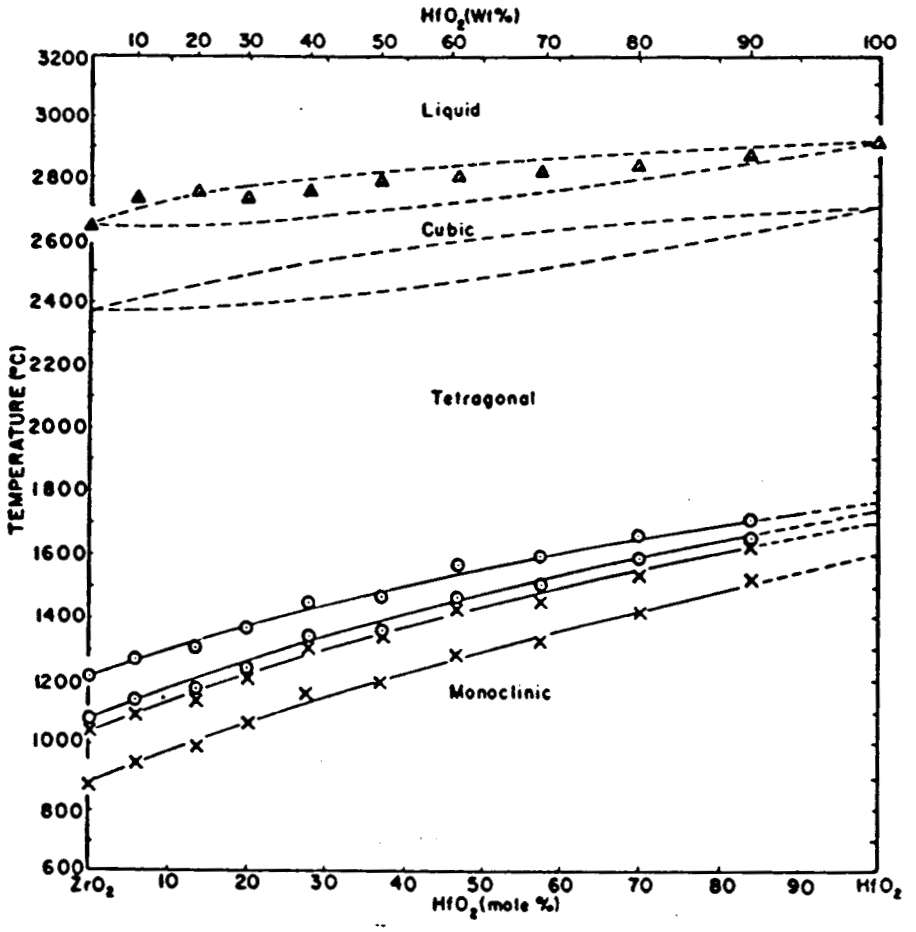

Figure 6. Phase equilibrium diagram for the HfO_2-ZrO_2 system (Ref. 22).

solidus and liquidus temperatures as well as the tetragonal to cubic inversions are estimated.) The open circles represent the monoclinic to tetragonal heating inversions while the X's represent the tetragonal to monoclinic cooling inversions.

2.1.2.2 HfO_2-TiO_2

The solubility limit of TiO_2 in HfO_2 is 10 to 13 mol% at 1600°C.[18,23] Beyond this limit, $HfTiO_4$ in a monoclinic solid solution occurs up to the $HfTiO_4$ solid solution region

which begins at 30 mol%.[18] The most recent phase equilibrium diagram (by Coutures and Coutures[18]) for the HfO_2-TiO_2 system is shown in Figure 7 along with the older Ruh et. al.[24] diagram. (The results of Coutures and Coutures agree with the findings of Schevchenko et. al..[25]) Coutures and Coutures explain the discrepancy in the diagrams to be the qualitative rather than quantitative determination of the $HfTiO_4$ melting temperature in the Ruh et. al. work.

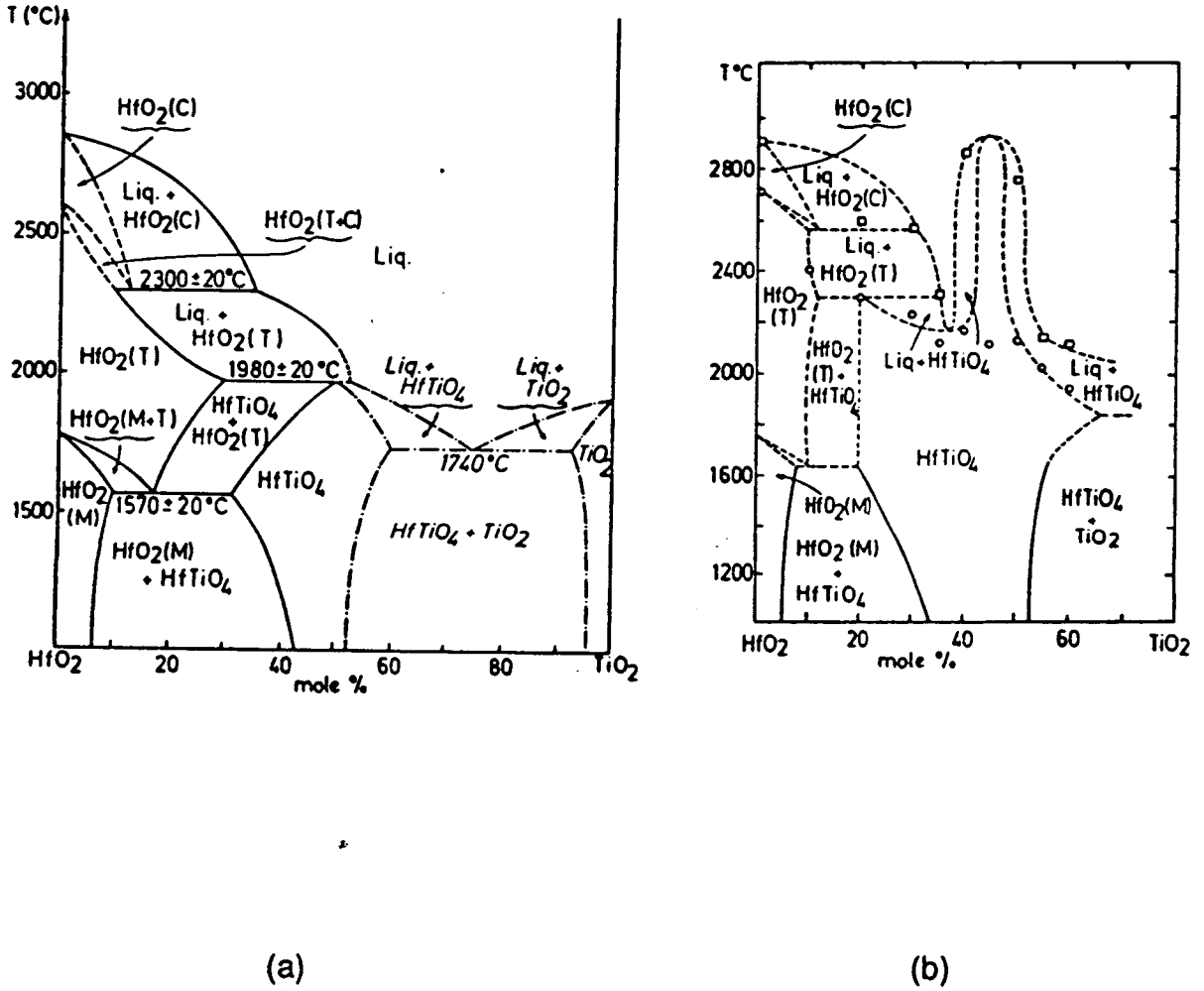

(a) (b)

Figure 7. Phase equilibrium diagrams for the HfO_2-TiO_2 system (a) (Ref. 18) and (b) (Ref. 24).

The phase boundaries of the equilibrium diagram of Coutures and Coutures were determined by examining both the transformation temperatures and the changes in lattice spacings of the titanate and monoclinic phases. Compositional limits of the phases were determined knowing: (1) The interplanar spacings of the monoclinic HfO_2 lattice decrease with TiO_2 additions in the solid solution region.[23] (2) Beyond the solubility limit (in the two-phase region), the spacings become constant with increasing TiO_2 as the titanate forms. (3) The titanate lattice parameters are constant in the two-phase regions and decrease with TiO_2 in the titanate solid solution region.[24] Using lattice parameter measurements and phase transformation temperatures, Coutures and Coutures constructed the HfO_2-TiO_2 phase diagram accordingly. The phase diagram shows that the the monoclinic to tetragonal and tetragonal to cubic inversion temperatures decrease with TiO_2 concentration and become constant in the two-phase region.

Concluding on the HfO_2-TiO_2 system, both Ruh et. al. and Coutures and Coutures observed that under certain thermal treatments, a second monoclinic phase formed in addition to the normal monoclinic and orthorhombic phases in the 0 to 50 mol% TiO_2 range. For samples annealed at 1600°C and above, traces of the second monoclinic phase appeared at 15 mol% TiO_2 and became the only monoclinic phase by 30 mol%. For samples annealed at 1300°C, the second monoclinic phase was not observed. Coutures and Coutures suggest that the lower volume second monoclinic phase has a higher TiO_2 concentration and that it decomposes to monoclinic HfO_2 and orthorhombic $HfTiO_4$.

2.1.2.3 ZrO_2-TiO_2

The solubility limit of TiO_2 in ZrO_2 is about 10 to 15 mol%.[26] Beyond this limit, $ZrTiO_4$ in a monoclinic solid solution results. Figure 8 shows the ZrO_2-TiO_2 phase diagrams of Brown and Duwez,[19] Coughanour et. al.[17] and Noguchi and Mizuno.[26]

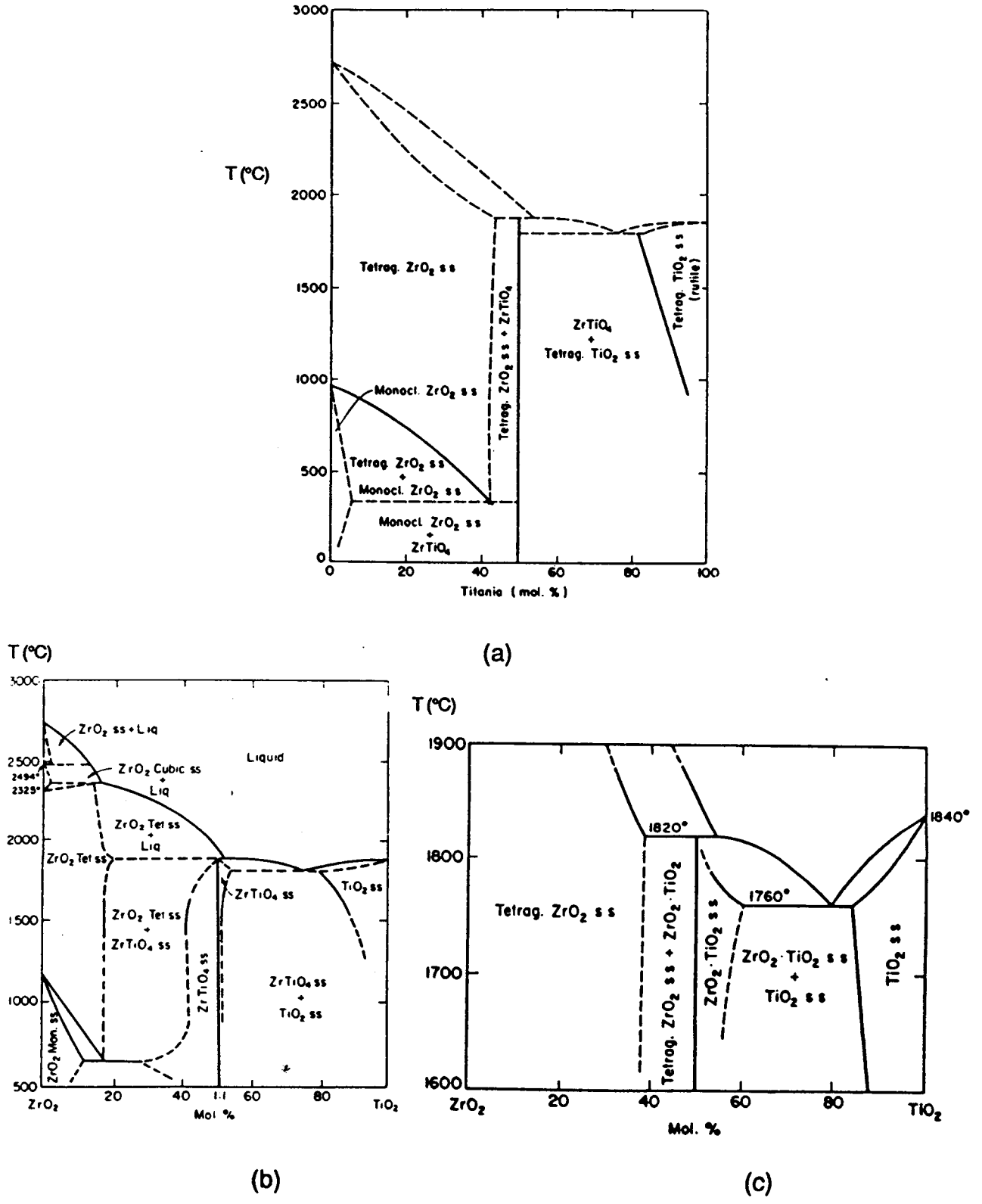

Figure 8. Phase equilibrium diagrams for ZrO_2-TiO_2 (a) (Ref. 19), (b) (Ref. 26), and (c) (Ref. 17).

Many anomalies exist between the diagrams, probably as a result of the advancements in zirconia studies between 1954 and 1968. A comparison with the HfO_2-TiO_2 phase diagrams suggests that the phase equilibrium in the ZrO_2-TiO_2 system is best depicted by Noguchi and Mizuno. The larger Noguchi and Mizuno TiO_2 solubility limit is probably more reliable than the lower value predicted by Brown and Duwez since the latter was based on less than accurate lattice parameter calculations. The tetragonal to cubic transformation in the Noguchi and Mizuno diagram probably needs to be redrawn such that the transformation temperature increases with increasing TiO_2 (similar to the HfO_2-TiO_2 system). In addition, the diagrams show that a decrease in the monoclinic to tetragonal transformation temperature with increasing titania occurs and a $ZrTiO_4$ solid solution range exists. Unlike in the HfO_2-TiO_2 studies, none of the studies of the ZrO_2-TiO_2 system showed a second monoclinic phase.

2.1.2.4 HfO_2-ZrO_2-TiO_2

The HZT ternary has been investigated by a number of authors;[1-5] however, the overwhelming task of producing a complete phase diagram has never been attempted. The primary difficulty in attempting such a task from literary information arises from the failure of most authors to specify the phases and compositions that they studied. Simpson[1] investigated the range of compositions 60 to 100 mol% HfO_2, 0 to 13 mol% ZrO_2 and 0 to 64 mol% TiO_2, generally referring to all compositions as hafnium titanates. (No phase analyses were performed.) Skaggs[5] in summarizing the HZT studies of Holcombe et. al.[27] (compositions in the range 16 to 47 mol% HfO_2, 16 to 47 mol% ZrO_2 and 37 mol% TiO_2), also recognized the failure of the authors to state the exact phases of the materials they were examining. Monoclinic solid solutions of 60 to 85 mol% HfO_2, 10 to 30 mol% ZrO_2, and 10 to 30 mol% TiO_2 were reported by Brown et. al.,[4] however, only a select few compositions were specified exactly. Complicating the situation further, Schroeder[3] concluded that compositions

with 32 mol% or greater TiO_2 formed titanates in hafnia-rich mixed oxides which is contrary to the findings of Ruh et. al.[24] and Coutures and Coutures.[18] Basically, the degree of solubility of TiO_2, the two-phase regions, and the effect of TiO_2 on the lattice parameters and transformation temperatures in the HZT system have never been reported conclusively.

2.2 Property Studies of Hafnia, Zirconia, and Titania

In the last section, a basic understanding of the structures and systems of hafnia, zirconia, and titania was given. This section will describe selected electrical and mechanical properties, then cite typical property values and compositional effects in the various hafnia, zirconia, and titania systems.

2.2.1 Electrical Conductivity

The electrical conductivity is a measure of the ability of a material to transport a charge. For typical ionically bonded ceramics, point defects are primarily responsible for charge transport. Ionic solids contain point defects at all temperatures above 0°K. The presence of ionic defects gives rise to ionic conductivity, while that of electronic defects results in electronic conductivity. The total electrical conductivity is given by the equation:

$$\sigma_T = \sum_i n_i (z_i e) \mu_i \qquad (1)$$

where n_i, z_i, and μ_i are the concentration, valency, and mobility, respectively, of the i^{th} charge carrying species and e is the electronic charge.[28] Ionic and electronic defects in ionic solids are presented using Kröger-Vink notation which specifies the kind, location, and effective charge of a defect.[29] Some of the typical defects for a MO_2 fluorite ionic crystal are given in Table 3 along with a basic description. Which of the point defects is the main mobile species depends on temperature, oxygen partial pressure, and dopant concentration. Figure 9 shows an example of the kinds of

pressure-temperature dependences that can occur. Dopants also alter the total conductivity by causing anion vacancies to be formed (thereby increasing ionic conductivity) or by acting as donors or acceptors (thereby increasing electronic conductivity).

Table 3. Typical Point Defects in MO_2 Ionic Crystals.

Symbol	Description	Effective Charge
O_O	Oxygen in Oxygen Site	Neutral
O_i''	Interstitially Incorporated Oxygen Ion	Negative
$V_O^{\bullet\bullet}$	Doubly-Ionized Oxygen Vacancy	Positive
V_M''''	Tetravalent Cation Vacancy	Negative
F_M'	Substitutionally Incorporated Trivalent Cation	Negative
$F_I^{\bullet\bullet\bullet\bullet}$	Interstitially Incorporated Tetravalent Cation	Positive
e_V	Electron in Valence Band	Neutral
e'	Electron in Conduction Band	Negative
$h^\bullet$	Hole in Valence Band	Positive

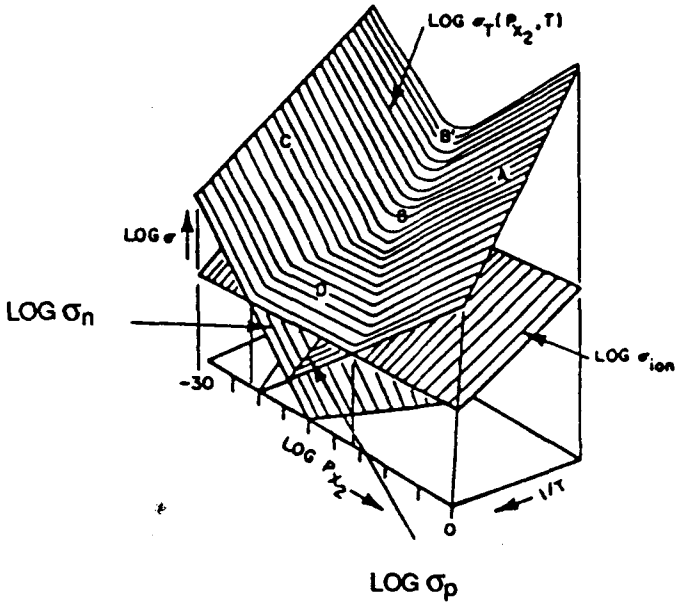

Figure 9. Schematic diagram of the P_{X_2}, T dependence of partial and total conductivities. A: $\sigma_p >> \sigma_{ion}, \sigma_n$. B-B': $\sigma_p = \sigma_n > \sigma_{ion}$. C: $\sigma_n >> \sigma_{ion}, \sigma_p$. D: $\sigma_{ion} >> \sigma_p + \sigma_n$ (Ref. 30).

2.2.1.1 Systems

An examination of several fluorite systems will elucidate some of the finer points of defect chemistry and electrical conductivity.

Pure HfO_2 and ZrO_2 in both the monoclinic and tetragonal form have been studied by several investigators.[12,31-37] From these studies, and those of Choudhary et. al.,[28] the following summary of the defect nature of HfO_2 and ZrO_2 can be made. The defect formation reactions can be written as:

$$O_o \overset{K_1}{\rightleftharpoons} O_i'' + V_o^{\bullet\bullet} \quad (2)$$

$$O_o \overset{K_2}{\rightleftharpoons} \tfrac{1}{2}O_2 + V_o^{\bullet\bullet} + 2e' \quad (3)$$

$$\tfrac{1}{2}O_2 \overset{K_3}{\rightleftharpoons} O_i'' + 2h^{\bullet} \quad (4)$$

where the mechanism described in Equation (2) is a thermally generated Frenkel defect. The mass-action law for each becomes, respectively:

$$K_1 = [O_i''][V_o^{\bullet\bullet}] \quad (5)$$

$$K_2 = n^2 P_{O_2}^{\frac{1}{2}} [V_o^{\bullet\bullet}] \quad (6)$$

$$K_3 = p^2 P_{O_2}^{-\frac{1}{2}} [O_i''] \quad (7)$$

where [ ] indicates defect concentrations and n and p are the electron and hole concentrations, respectively. Electroneutrality requires that $n+2[O_i''] = p+2[V_o^{\bullet\bullet}]$. The defect concentrations as a function of partial pressure then become:

In Region I (low P_{O_2}) where the prevailing electroneutrality condition is $n=2[V_o^{\bullet\bullet}]$,

$$n = (2K_2)^{\frac{1}{3}} P_{O_2}^{-\frac{1}{6}} \quad (8)$$

$$[V_o^{\bullet\bullet}] = (K_2/4)^{\frac{1}{3}} P_{O_2}^{-\frac{1}{6}} \quad (9)$$

$$[O_i''] = (4K_1^3/K_2)^{\frac{1}{3}} P_{O_2}^{\frac{1}{6}} \quad (10)$$

and $$p = (K_2K_3^3/4K_1^3)^{\frac{1}{6}} P_{O_2}^{\frac{1}{6}} \quad (11)$$

In Region II (medium P_{O_2}) where $[O_i''] = [V_o^{\bullet\bullet}]$,

$$[V_o^{\bullet\bullet}] = [O_i''] = K_1^{\frac{1}{2}} \quad (12)$$

$$n = (K_2^2/K_1)^{\frac{1}{4}} P_{O_2}^{-\frac{1}{4}} \quad (13)$$

and $$p = (K_3^2/K_1)^{\frac{1}{4}} P_{O_2}^{\frac{1}{4}} \quad (14)$$

And in Region III (high P_{O_2}) where $p = 2[O_i'']$,

$$p = (2K_3)^{\frac{1}{3}} P_{O_2}^{\frac{1}{6}} \quad (15)$$

$$[O_i''] = (K_3/4)^{\frac{1}{3}} P_{O_2}^{\frac{1}{6}} \quad (16)$$

$$[V_o^{\bullet\bullet}] = (4K_1^3/K_3)^{\frac{1}{3}} P_{O_2}^{-\frac{1}{6}} \quad (17)$$

and $$n = (K_3K_2^3/4K_1^3)^{\frac{1}{6}} P_{O_2}^{-\frac{1}{6}} \quad (18)$$

The Kröger-Vink diagram which shows the expected defect concentration dependence of HfO_2 and ZrO_2 on the oxygen partial pressure is shown in Figure 10. The diagram was constructed by Douglass and Wagner[38] using equations similar to Equations (8)-(18).

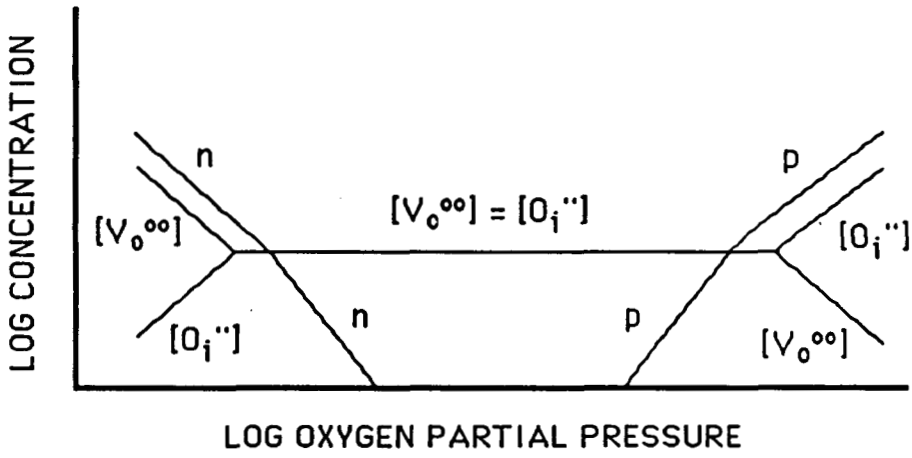

Figure 10. Kröger-Vink diagram showing pressure dependence of defect concentration for HfO_2 and ZrO_2 (Ref. 38).

The partial ionic conductivity (σ_{ion}) and partial electronic conductivity (σ_{el}) in terms of the defect concentrations are given by:

$$\sigma_{ion} = 2F(\mu_i[O_i''] + \mu_v[V_o^{\bullet\bullet}])/V_M \quad (19)$$

and $$\sigma_{el} = F(\mu_e n + \mu_h p)/V_M \quad (20)$$

where F is the Faraday constant; V_M is the molar volume of ZrO_2; and μ_i, μ_v, μ_e, and μ_h are the mobilities of interstitial oxygen ions, anion vacancies, and excess electrons

and holes, respectively.[36] In general, the mobility of an electron is 100 to 1000 times greater than that of interstitial anions. Also, in MO_2 fluorites, the mobility of anion vacancies is much greater than that of interstitial anions.[36]

The oxygen pressure dependence of the ionic and electronic conductivities are then:

In Region I (low pressures),

$$\sigma_{ion} = (2F/V_M)\{\mu_i(4K_1^3/K_2)^{\frac{1}{3}} P_{O_2}^{\frac{1}{6}} + \mu_v(K_2/4)^{\frac{1}{3}} P_{O_2}^{-\frac{1}{6}}\} \quad (21)$$

and $$\sigma_{el} \cong (F\mu_e/V_M)(2K_2)^{\frac{1}{3}} P_{O_2}^{-\frac{1}{6}} \quad (22)$$

when $\mu_e n \gg \mu_h p$

In Region II (medium pressures),

$$\sigma_{ion} = (2F/V_M)(\mu_i + \mu_v)K_1^{\frac{1}{2}} \quad (23)$$

and $$\sigma_{el} \cong (F\mu_h/V_M)(K_3^2/K_1)^{\frac{1}{4}} P_{O_2}^{\frac{1}{4}} \quad (24a)$$

when $\mu_h p \gg \mu_e n$

$$\sigma_{el} \cong (F\mu_e/V_M)(K_2^2/K_1)^{\frac{1}{4}} P_{O_2}^{-\frac{1}{4}} \quad (24b)$$

when $\mu_e n \gg \mu_h p$

And in Region III (high pressures),

$$\sigma_{ion} = (2F/V_M)\{\mu_i(K_3/4)^{\frac{1}{3}} P_{O_2}^{\frac{1}{6}} + \mu_v(4K_1^3/K_3)^{\frac{1}{3}} P_{O_2}^{-\frac{1}{6}}\} \quad (25)$$

and $$\sigma_{el} \cong (F\mu_e/V_M)(2K_3)^{\frac{1}{3}} P_{O_2}^{\frac{1}{6}} \quad (26)$$

when $\mu_h p \gg \mu_e n$

The total electrical conductivity is the sum of the ionic and electronic conductivities. Figure 11 shows the experimentally determined pressure and temperature dependence of the total electrical conductivity of pure monoclinic ZrO_2 from the work of Kumar et. al..[36] At low pressures, the conductivity is shown to have a limiting $P_{O_2}^{-\frac{1}{6}}$ dependence (n-type). The conductivity at high pressures is shown to have a $P_{O_2}^{\frac{1}{4}}$ dependence (p-type). An apparent discrepancy exists in Region III between the expected $P_{O_2}^{\frac{1}{6}}$ dependence and the observed $P_{O_2}^{\frac{1}{4}}$ dependence. A similar discrepancy was observed in monoclinic thoria by Choudhary et. al..[28]

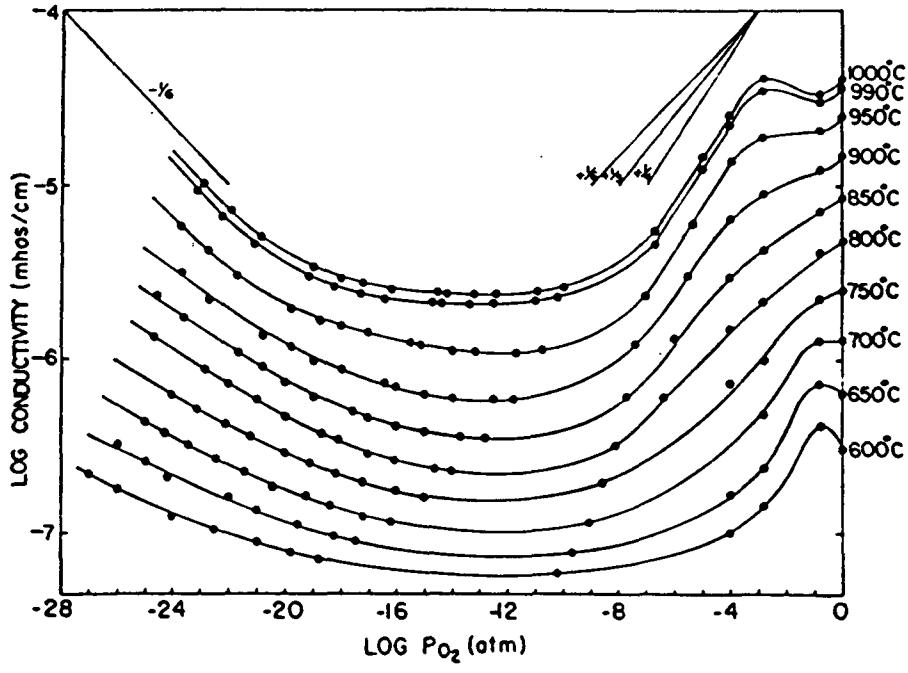

Figure 11. Temperature and pressure dependence on electrical conductivity of pure monoclinic ZrO_2 (Ref. 36).

Choudhary et. al. and Kumar et. al. examined the differences in the theoretical and experimental high pressure conductivities. Both concluded that the discrepancy occurred as a result of impurities which modified the controlling defect mechanisms at high pressures. In an effort to characterize the effects, Kumar et. al. chose to examine the electronic and ionic contributions of the conductivity. Coupling the experimentally determined transference numbers with the measured total conductivities, they were able to separate the ionic and electronic components from the total electrical conductivity. They showed that the electrical conductivity of zirconia was ionically controlled below approximately 700°C and electronically controlled above 700°C for $10^{-22} \leq P_{O_2} \leq 1$ atm. A schematic diagram of the expected pressure dependence on the electronic and ionic conductivities for the electronically controlled situation (modelled after Kumar et. al.) is shown in Figure 12. Two possibilities are presented.

Kumar et. al. found that their data was not accurate enough to distinguish between the two. However, based on Arrhenius plots of the ionic conductivity, Kumar et. al. concluded that the data for ZrO_2 was consistent with an anti-Frenkel disorder in which singly ionized oxygen interstitials predominated at high pressures. Singly ionized oxygen interstitials occur when impurities are present and lead to a $P_{O_2}^{\frac{1}{4}}$ dependence in the high pressure region in agreement with the experimental data. Nonetheless, in order to fully verify the fluorite defect model presented in Equations (2)-(26), conductivity data for monoclinic hafnia, zirconia or thoria without impurities should be collected and plotted to show the proper P_{O_2} dependence.

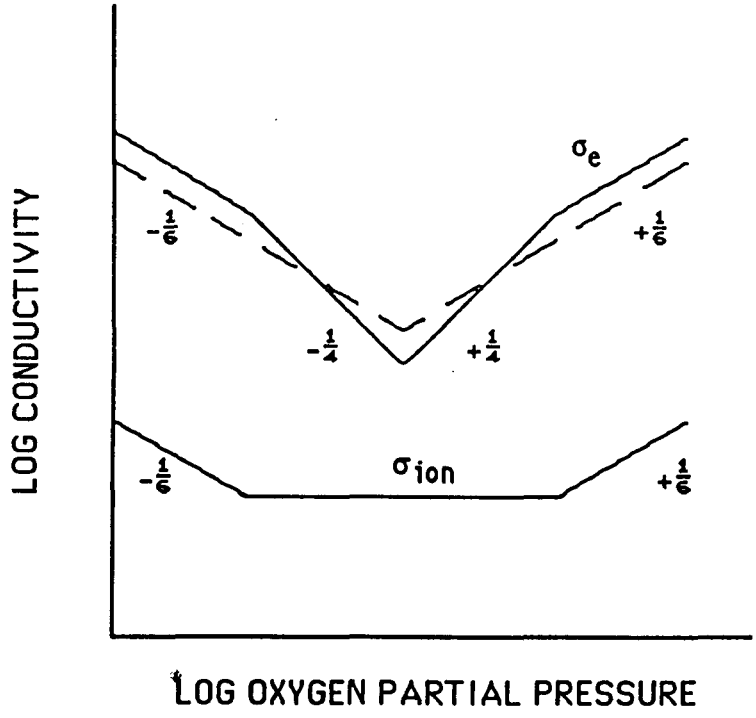

Figure 12. Schematic diagram of the expected pressure dependence on the electronic and ionic conductivities for ZrO_2 at high temperatures (Ref. 36).

Numerous studies of doped HfO_2 and ZrO_2 have been made. Some of the more recent review articles are by Choudhary et. al.,[28] Dell and Hooper,[39] and Subbarao.[8] A summary of the main aspects follows.

Several types of dopants can be added which may alter the conduction mechanisms of the fluorite structure. Mixed oxides having cations with essentially invariant valence (e.g., Zr^{4+}, Hf^{4+}, Th^{4+}, Sc^{3+}, Y^{3+}, La^{3+}, Mg^{2+}, and Ca^{2+}), generally tend to exhibit purely ionic conductivity (independent of oxygen partial pressure) over a wide range of oxygen pressures. Those cations which reduce to lower valences (e.g., $Ce^{4+}\rightarrow Ce^{3+}$, $Fe^{3+}\rightarrow Fe^{2+}$, $Eu^{3+}\rightarrow Eu^{2+}$), or those which oxidize to higher valences (e.g. $Ni^{2+}\rightarrow Ni^{3+}$, $Co^{2+}\rightarrow Co^{3+}$, and $U^{4+}\rightarrow U^{6+}$), will tend to introduce electron or hole conduction, respectively, via hopping mechanisms to the otherwise ionic conductor.

When aliovalent oxides with stable valences are substituted as impurities into the fluorite structure, they usually tend to stabilize the cubic phase and produce vacancies in the oxygen sublattice if their valence is less than four.[28] The electrical conductivity increases due to the increased concentration of oxygen vacancies. The temperature dependence exhibited by the electrical conductivity approximates Arrhenius behavior.[28] A limit to the enhancement of conductivity with dopant is reached when the oxygen vacancy mobility decreases as a result of lattice distortions and the formation of (F_M'-$V_o^{\bullet\bullet}$) complexes or vacancy clusters.[28,40-41] Figure 13 shows the maxima in conductivity with impurity concentration for some typical ZrO_2-based systems.

For aliovalent impurities added to the fluorite structure as in Y_2O_3-stabilized ThO_2, the electroneutrality requires:

$$p + 2[V_o^{\bullet\bullet}] = n + 2[O_i''] + [Y_{Th}'] \qquad (27)$$

where $[Y_{Th}']$ is the concentration of Y^{3+} ions on Th^{4+} sites. Following an analysis similar to that used for pure ZrO_2, the Kröger-Vink diagram in Figure 14 for a doped

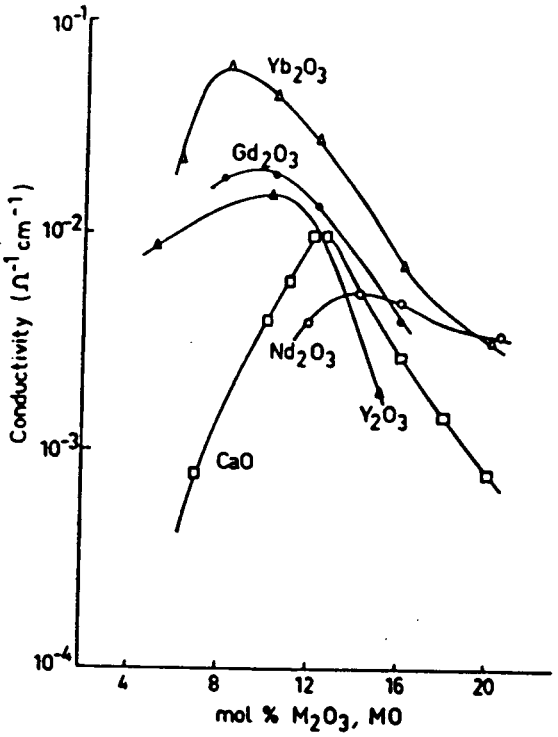

Figure 13. Maxima in conductivity for various doped ZrO_2-based materials at T= 1080°K (Ref. 41).

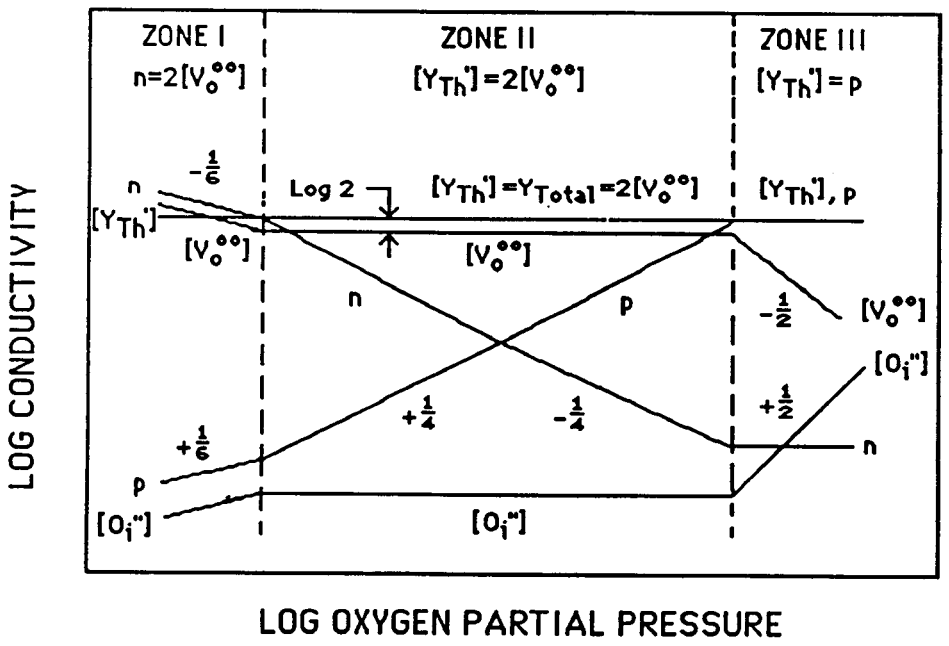

Figure 14. Kröger-Vink diagram showing pressure dependence of doped fluorite structure (Ref. 28).

fluorite structure was constructed. Also, Figure 15 shows the expected oxygen partial pressure dependence on conductivity. The effects of aliovalent impurities is primarily seen in the high pressure region. For the condition that $[Y_{Th}']$ = p, the mass-action laws lead to the pressure dependence seen in Zone III of Figure 15. In this region, the hole conductivity becomes independent of oxygen partial pressure. A fourth zone which is not shown in Figures 14 and 15 occurs for very high oxygen partial pressures. The condition p = $2[O_i'']$ exists giving concentration and conductivity dependencies similar to those observed in the high pressure regions of the pure state.

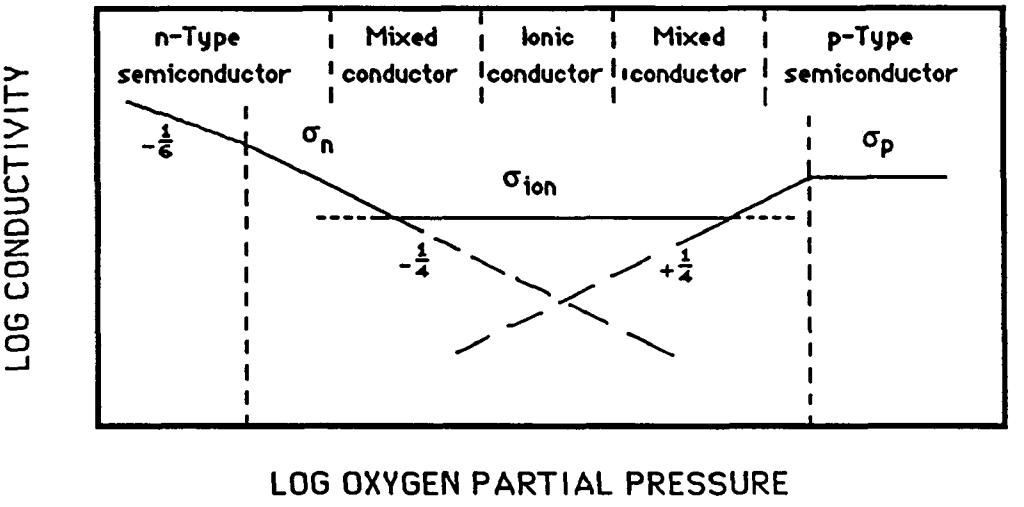

Figure 15. Schematic diagram of the expected pressure dependence on the electrical conductivity of a doped fluorite structure (Ref. 28).

With regards to temperature, in the ionic conduction region:

$$[F_M'] \doteq 2[V_O^{\bullet\bullet}] \qquad (28)$$

and is constant with temperature.[28] On the other hand,

$$[O_i''] = \frac{K_1}{[V_O^{\bullet\bullet}]} = K_1^{\circ} \exp(\frac{-\Delta G_1}{RT}) / \tfrac{1}{2}[F_M'] = k \exp(\frac{-\Delta G_1}{RT}) \qquad (29)$$

where ΔG_1 is the standard state free energy for the reaction in Equation (2), and k is a constant. $[O_i'']$ increases with temperature until:

$$[V_o^{\circ\circ}] = [O_i''] = (K_1^{\circ})^{\frac{1}{2}} \exp(\frac{-\Delta G_1}{2RT}) \qquad (30)$$

at which point the material shows intrinsic behavior.[28] Figure 16 demonstrates this point. Intrinsic behavior is rarely observed in doped oxide electrolytes, however.[28]

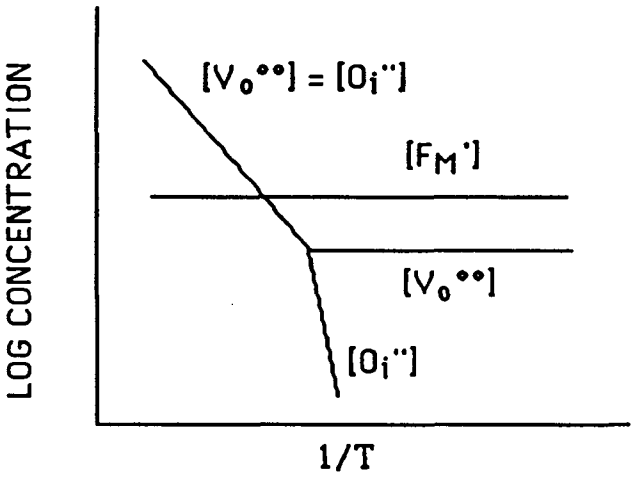

Figure 16. Schematic diagram demonstrating the effect of the temperature on defect concentration in MO_2-F_2O_3 at constant oxygen partial pressure (Ref. 28).

When multivalent cations are added to the fluorite structure, an increase in electronic conductivity results. A possible defect ionization reaction for a dopant incorporated substitutionally into the fluorite structure would be:

$$F_M + e' \rightleftarrows F_M' \qquad (31)$$

where F_M and F_M' represent substitutionally incorporated tetravalent and trivalent cations on cation sites, respectively. The electronic conductivity is increased via electrons hopping between dopant cations.[43]

If a multivalent cation is incorporated interstitially into the fluorite structure, the reaction would be:

$$FO_2 \rightarrow F_i^{\circ\circ\circ\circ} + 4e' + O_2\,(g) \qquad (32)$$

where F is a tetravalent cation.[44] The excess electrons could then be incorporated either by $F_i^{\circ\circ\circ\circ}$ or $V_o^{\circ\circ}$ following the equations:

$$F_I^{\bullet\bullet\bullet\bullet} + e' \rightarrow F_I^{\bullet\bullet\bullet} \quad (33)$$

or $$V_O^{\bullet\bullet} + 2e' \rightarrow V_O \quad (34)$$

The latter situation is the case for TiO_2 doped Y_2O_3-stabilized ZrO_2 as reported by Worrell and Weppner.[44] In their study, they found that titanium is incorporated interstitially into the fluorite structure; however, its effective charge is unknown. The result is a mixed ion-electron conductor. The electronic conductivity is high at low and high pressures. Figure 17 shows the temperature dependence of the electrical conductivity at various oxygen partial pressures for two titania dopant concentrations.

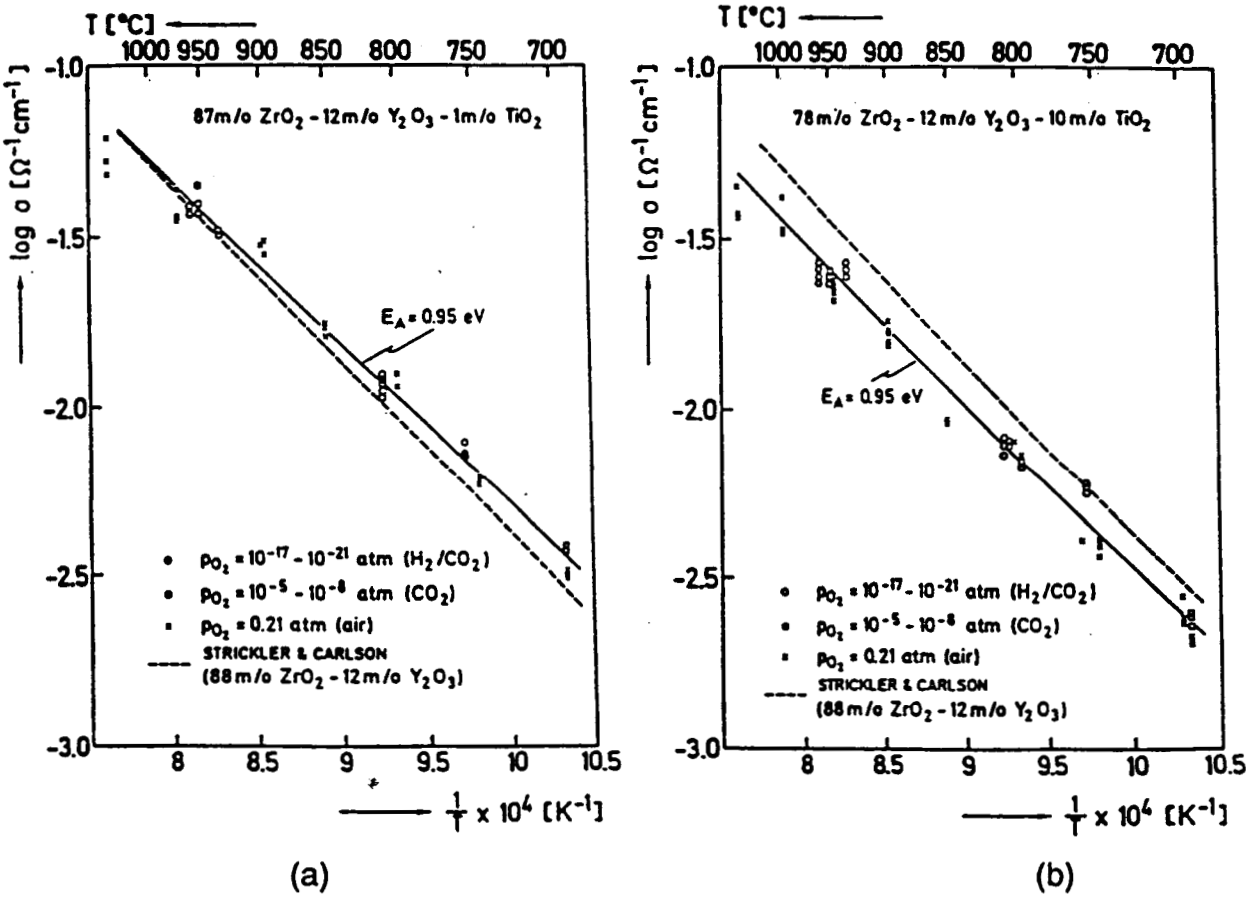

Figure 17. The dependence of electrical conductivity on temperature for various oxygen partial pressures for (a) 1 mol% and (b) 10 mol% TiO_2 in Y_2O_3-stabilized ZrO_2 (Ref. 44).

2.2.1.2 Measurements

High temperature electrical conductivity measurements are generally made using two- or four-probe methods.[39] One of the primary concerns in measuring with probes is electrode polarization (i.e., the build-up of charge at an electrode). The design of the four-probe method eliminates these effects.[45] Polarization in the two-probe method is eliminated by using ac current (500 kHz to 5 MHz).[39] The sample configuration is best when the ratio of probe separation to sample thickness is large. This assures that current paths are straight.

Resistance measurements are taken for a sample of known cross sectional area (A) and probe separation (l). When a known current (I) with known voltage (V) is passed through the sample, the resistance (R) becomes:

$$R = \frac{V}{I} \tag{35}$$

The relation between measured resistance and the resistivity (ρ) is:

$$\rho = R\frac{A}{l} \tag{36}$$

And the conductivity is then just the inverse of the resistivity.

When measurements are made as a function of oxygen partial pressure, two factors need to be considered. First, the movement of gas away from the electrode should be rapid; second, the gas mixture which establishes the P_{O_2} should not react with the sample (altering the defect chemistry). In address to the second of these factors, most conductivity studies use either H_2/H_2O or CO/CO_2 gas mixtures to establish low oxygen partial pressures. McClaine and Coppel[35], however, reported observations of interactions of H_2/H_2O and CO/CO_2 gas mixtures with pure tetragonal ZrO_2. (Carniglia et. al.[46] later noticed similar behavior in their studies of ThO_2 and ZrO_2.) McClaine and Coppel found that increased electronic conductivities occurred when H_2/H_2O gas mixtures were used to establish oxygen partial pressures as

opposed to when CO/CO_2 gas mixtures were used. They attributed this increased conductivity to the presence of hydrogen entering the matrix as interstitial positive ions. (A similar effect occurs in ZnO.) They found that the use of CO/CO_2 gas mixtures had much less of an effect on the electrical properties. (Both a high concentration and a highly active species is required for the gas reactants to dominate the defect chemistry. Apparently, neither condition prevails in the electrical conductivity of ZrO_2 electrolytes in CO/CO_2 gas mixtures.) From their studies, therefore, McClaine and Coppel recommended the use of CO/CO_2 gas mixtures for low pressure conductivity studies of pure ZrO_2. Nonetheless, further examination of the use of CO/CO_2 gas mixtures, as well as H_2/H_2O gas mixtures, is warranted.

2.2.2 Thermal Expansion

Thermal expansion is the linear or volumetric change that accompanies an increase in temperature. The linear thermal expansion coefficient (α) is defined as the ratio of the change in length per °C to the length at 0°C and can be expressed as:

$$L_T = L_o (1 + \alpha T) \qquad (37)$$

where L_o and L_T are the lengths at 0°C and some temperature T, respectively.

Most materials when heated tend to enlarge or expand in response to the increase in temperature. Such materials are said to have positive thermal expansion coefficients. Typically, thermal expansion coefficients of ceramic materials are of the order of 4.0 to 14 x 10^{-6}/°C. For applications where rapid cycling between high and low temperatures is necessary, materials with low or zero coefficients are best. (These materials tend to exhibit high thermal shock resistance.) Skaggs[5] points out that common factors in low thermal expansion materials are: (1) The symmetry is never cubic, infrequently tetragonal, possibly monoclinic, and usually orthorhombic. (2) Strong axial expansions and contractions are present (e.g., the axial thermal

expansion of orthorhombic $HfTiO_4$ is very strongly negative along the b-axis, while it is moderately positive along the a-axis). (3) The material is usually in ternary combinations. (4) A large open spaced lattice is usually involved. (5) A hysteresis in the thermal cycle usually occurs.

2.2.2.1 Systems

A number of ceramic materials with low thermal expansion coefficients have been cited in the literature.[1-5] Many compositions in the hafnia, zirconia, and titania systems are among these low coefficient materials. An examination of several materials will elucidate the mechanisms involved in low thermal expansion.

The thermal expansion of HfO_2 and ZrO_2 has been studied by several authors.[13,18,22,47-54] Table 4 summarizes the axial and linear thermal expansions of the monoclinic and tetragonal phases found in these investigations. Table 4 also gives the calculated linear thermal expansion coefficient ($\alpha_{calc.}$) of the monoclinic phases, determined from the x-ray data of Ruh et. al.,[54] as well as the volumetric thermal expansion coefficients of the unit cells ($V_{unit\ cell}$). For ZrO_2, the measured thermal expansion coefficient compares very well with the calculated value, whereas, a difference is observed for HfO_2. This difference is associated with microcracking which Dole et. al.[52] have shown indeed occurs in HfO_2. Microcracking leads to open cracks at low temperatures that close as temperature increases.[54] The effect is that the linear thermal expansion coefficient of the bulk material appears lower than the true lattice thermal expansion coefficient. In thermal expansion measurements, microcracking is observed as a hysteresis in the thermal cycle. Figure 18 shows the type of hysteresis associated with microcracking found in thermal expansion data. This hysteresis, and thus microcracking, is eliminated in fine grained (<2 μm) materials.[52] In addition to the hysteresis associated with microcracking, a hysteresis in the thermal cycle associated with the monoclinic to tetragonal phase transformation

Table 4. Axial and Linear Thermal Expansion Coefficients of HfO_2 and ZrO_2.

Parameter	Thermal Expansion Coefficient (10^{-6}/°C)*			
	ZrO_{2mono}	ZrO_{2tet}	HfO_{2mono}	HfO_{2tet}
a	9.2	11.6[49]	6.1[18]	6.1[18]
b	1.4		0.0[18]	
c	10.9	16.1[49]	9.6[18]	5.6[18]
ß	-4.5		-3.6	
$V_{unit\ cell}$	22.9	37.37[49]	20.6	37.2[18]
$\alpha_{meas.}$	7.2	10.63[49]	4.4-6.5	10.0[47]
$\alpha_{calc.}$	7.6		6.9	

*All values from Ref. 54 unless otherwise noted.

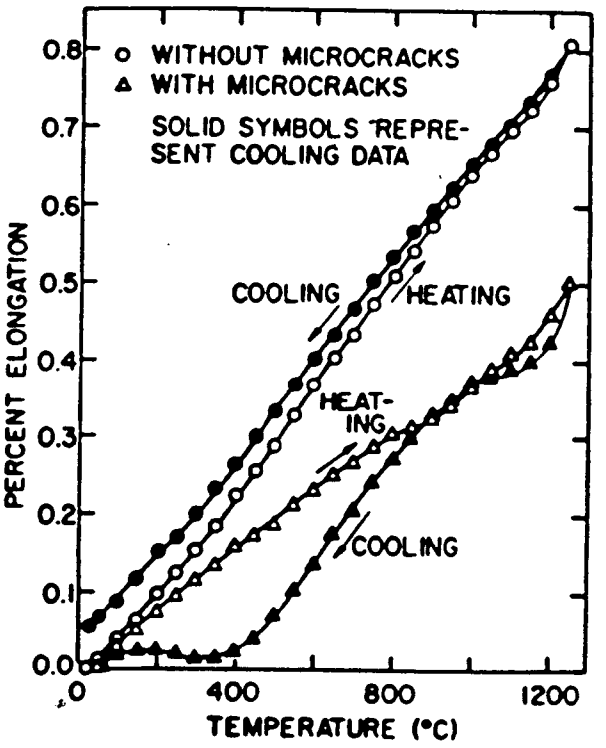

Figure 18. Linear thermal expansion coefficient of microcracked (>2 µm grains) and crack-free (<2 µm grain size) HfO_2 (Ref. 52).

occurs. This temperature hysteresis can be seen in the phase diagram in Figure 6 for the system HfO_2-ZrO_2. Figure 19 shows a typical hysteresis in the thermal expansion associated with the monoclinic to tetragonal phase transformation. The volume change of the transformation is 2.7%[51] and 3.0%[49] for HfO_2 and ZrO_2, respectively. It is this volume change which is used in transformation toughening and which is deleterious to pure unstabilized ZrO_2 and HfO_2.

The thermal expansion coefficients for a wide range of compositions in the HfO_2-ZrO_2 system were determined by Stansfield.[21] In general, the coefficient increased as ZrO_2 was added to HfO_2 while the transformation temperature decreased.

An extensive study of the effect of various additives (e.g., CaO, MgO, etc.) to ZrO_2 on the thermal expansion was made by Curtis.[55] Among other findings were the following: (1) Small additions of CaO and MgO (metastable region) reduce the inversion hysteresis and leave the thermal expansion coefficient relatively unchanged. (2) Large additions of CaO and MgO (cubic stabilized region) eliminate the inversion hysteresis but raise the thermal expansion coefficient.

The effect of adding TiO_2 to HfO_2 and ZrO_2 on the thermal expansion has been studied by several investigators.[1,5,18,19,24,56-58] Analogous to the pure oxides, the thermal expansion behaviors of the two systems are quite different. For additions of TiO_2 to ZrO_2, Brown and Duwez[19] showed that the thermal expansion coefficient decreased with increasing TiO_2. Figure 20 shows the thermal expansion curves from their study. The thermal expansion coefficient is ca. 7.5 x 10^{-6}/°C for both pure ZrO_2 and the 10 mol% TiO_2 composition. For the 20, 30, and 40 mol% compositions, a gradual decrease from 6.7 to 5.0 x 10^{-6}/°C occurs. Phase analyses show that for compositions greater than 15 mol% TiO_2, $ZrTiO_4$ begins to appear in the monoclinic solid solution. The increase in the concentration of the titanate phase slightly reduces

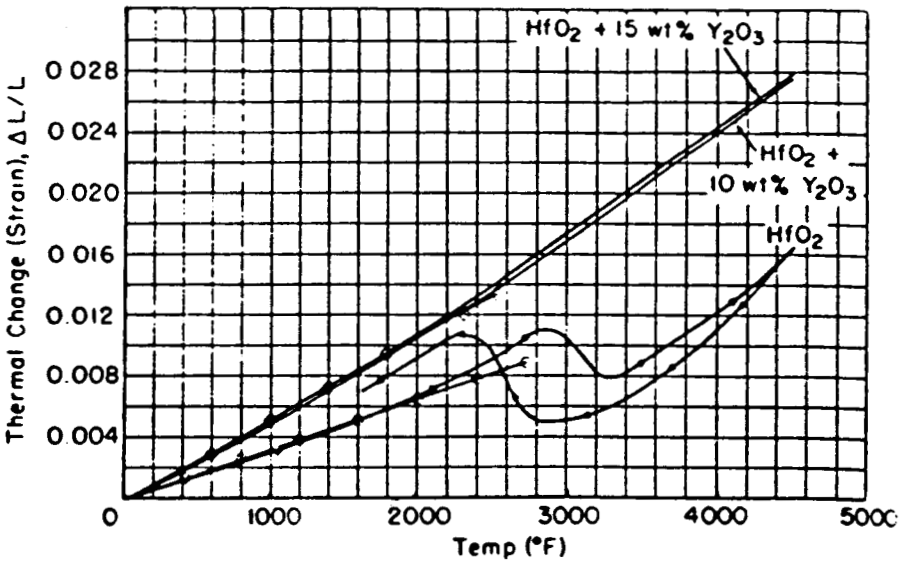

(a)

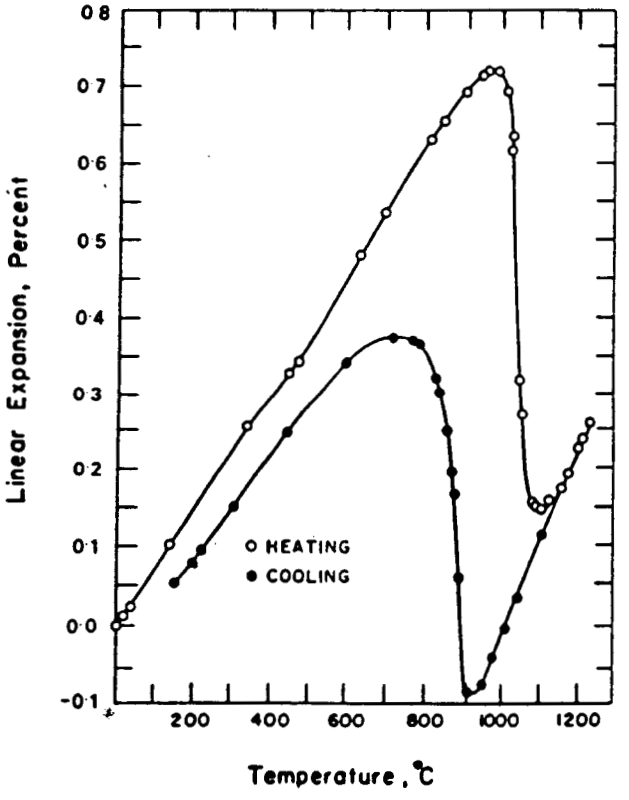

(b)

Figure 19. Linear thermal expansion demonstrating transformation temperature hysteresis of (a) HfO_2 (Ref. 47) and (b) ZrO_2 (Ref. 49).

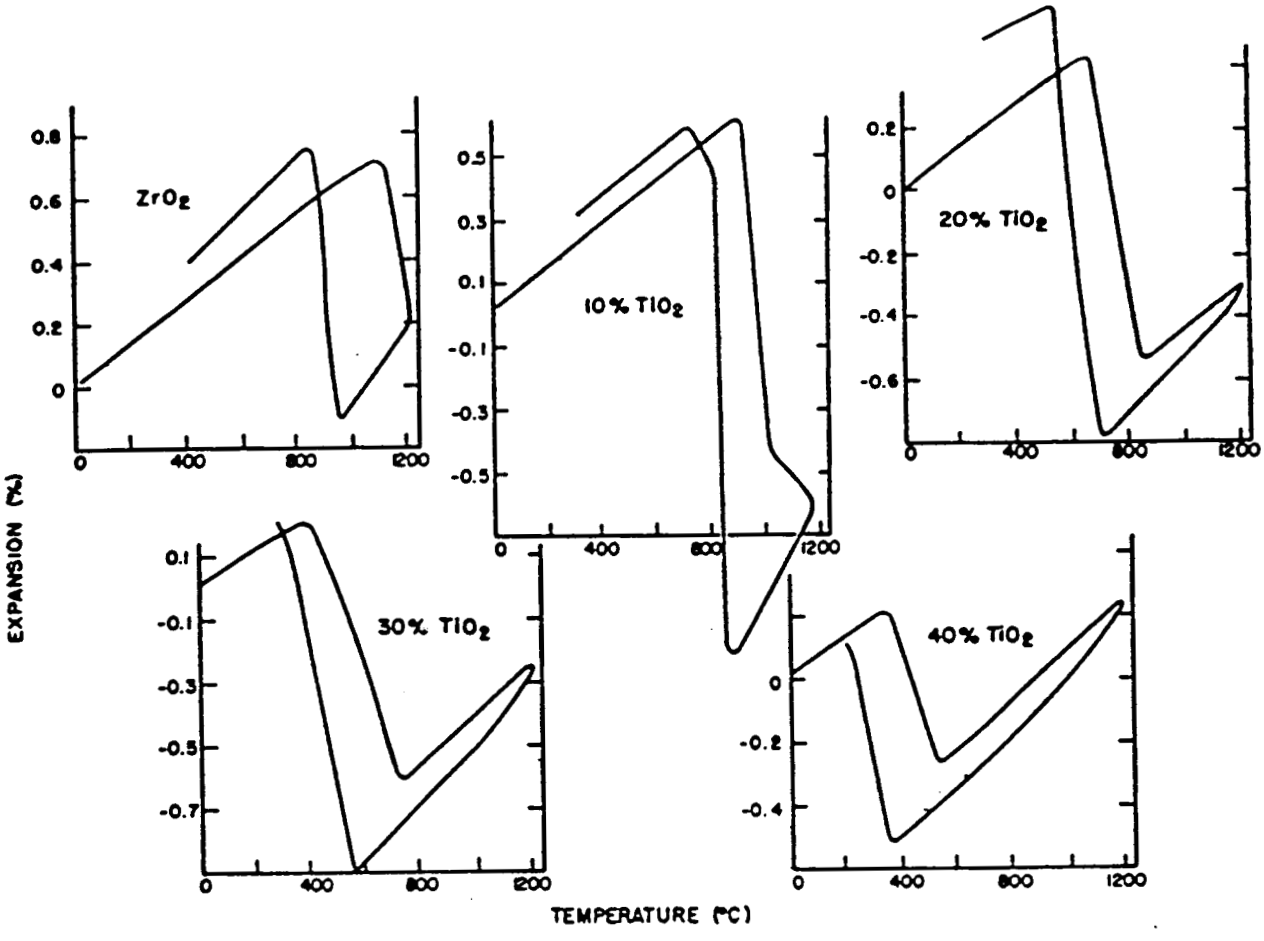

Figure 20. Linear thermal expansion curves of ZrO_2 containing various mole percentages of TiO_2 (Ref. 19).

the expansion and leads to a decrease in the magnitude of the monoclinic to tetragonal phase transformation hysteresis.

In contrast, for additions of TiO_2 to HfO_2, large reductions in the thermal expansion have been observed. Low, zero, and even negative thermal expansion coefficients have been reported for compositions in the HfO_2-TiO_2 system.[1,5,18,24,56-58] Figure 21 shows the linear thermal expansion of a number of HfO_2-TiO_2 compositions. For compositions between 30 and 40 mol% TiO_2, very low coefficients ($<1 \times 10^{-6}/°C$) are observed, while for compositions greater than 40 and less than 30 mol%, moderate coefficients ($\sim 4 \times 10^{-6}/°C$) are found. The compositional dependence of the thermal expansion is summarized in Figure 22. An examination of the HfO_2-TiO_2

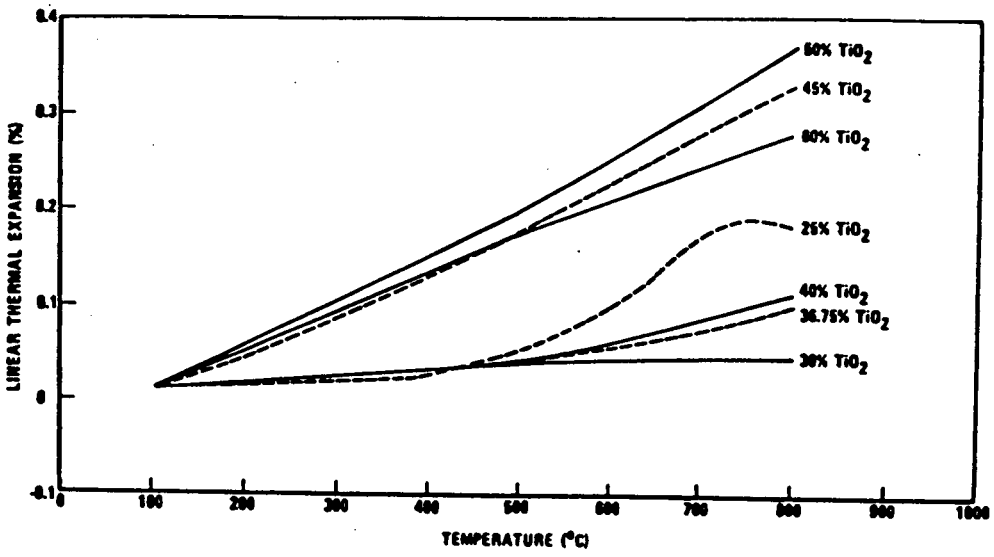

Figure 21. Linear thermal expansion for several HfO_2-TiO_2 compositions (in mol%) (Ref. 56).

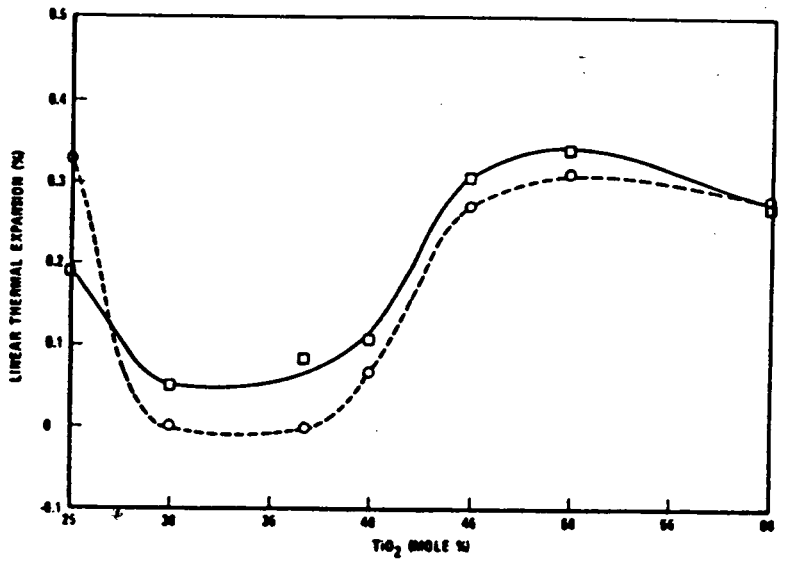

Figure 22. Linear thermal expansion vs. HfO_2-TiO_2 composition at 750°C. Open squares (Ref. 56). Open circles (Ref. 24).

phase diagram shows that the compositions with the lowest coefficients lie within the two-phase ($HfTiO_4$ plus monoclinic HfO_2) region. Three conditions which are present in the HfO_2-TiO_2 system but are not present in the ZrO_2-TiO_2 system have been associated with the low thermal expansion coefficients. First, the b-axial thermal expansion is negative for $HfTiO_4$ in contrast to the positive expansion which occurs for $ZrTiO_4$ (see Figure 23).[24] Second, a hysteresis in the thermal expansion data is observed for $HfTiO_4$ but is not present in the $ZrTiO_4$ data.[58] Third, microcracking occurs in the HfO_2-TiO_2 system but not in the ZrO_2-TiO_2 system.[58] Each of these conditions leads to low thermal expansion in the HfO_2-TiO_2 system. Similar to the ZrO_2-TiO_2 system, the titanate phase decreases the magnitude of the monoclinic to tetragonal phase transformation hystereses for compositions in the HfO_2-TiO_2 system.

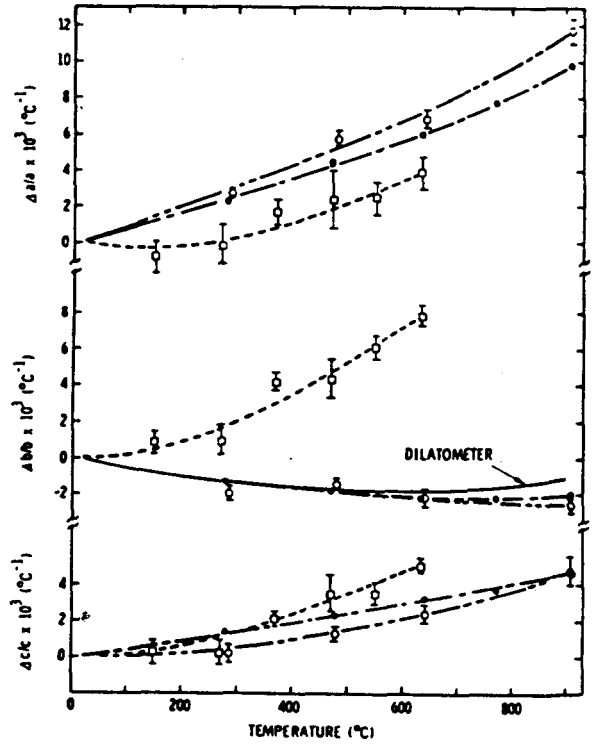

Figure 23. Axial thermal expansion of orthorhombic $HfTiO_4$ (solid circles), $Hf_{1.26}Ti_{0.74}O_4$ (open circles) and $ZrTiO_4$ (open squares) (Ref. 57).

In the HZT system, many reports of compositions with low thermal expansion coefficients have been made. In almost every study, the low coefficient materials were within the titanate plus monoclinic two-phase region. Exceptions were found in the work of Schroeder[3] and Brown et. al..[4] Both investigations report compositions with low thermal expansion coefficients in the monoclinic solid solution region of the phase diagram. For compositions where the titanate phase is present, the low thermal expansion coefficients are attributed to microcracking which results from the negative b-axial thermal expansion of the titanate phase. Schroeder showed that the b-axis of the monoclinic phase in the composition that he studied also exhibited negative thermal expansion. He attributed the low linear thermal expansion coefficient to the negative b-axial thermal expansion, but never addressed the possibility of microcracking. He presented an openness model to explain the reduced expansion tendencies. In the openness model, titanium ions, which are smaller than either hafnium or zirconium ions, assume cation positions on the lattice which is oversized for the titanium ion. The result is an increased openness in the lattice which can better accommodate thermal agitation, thereby decreasing the rate of thermal expansion.[59] The openness model, however, states that once the titanate phase begins to form, an increase in thermal expansion occurs which is contrary to the reported observations.

Table 5 summarizes the thermal expansion behavior of various compositions in the HZT system. For compositions which are well within the known titanate plus monoclinic solid solution region, the coefficients decrease with additions of ZrO_2 up to a limit (ca. 13%) and then increase. In addition, from the work of Brown et. al.,[4] a range of compositions and coefficients were reported. The range of coefficients were -1 to 5 x 10^{-6}/°C for compositions 60 to 85 mol% HfO_2, 10 to 30 mol% ZrO_2 and 10 to 30 mol% TiO_2. It is suspected that the lowest coefficient corresponded to a composition with approximately 60 mol% HfO_2-10 mol% ZrO_2-30 mol% TiO_2. One final comment regarding the effect of TiO_2 on the expansion behavior of HZT compositions,

the monoclinic to tetragonal transformation range is widened and the volume change is lowered when the concentration of titania is increased.[3]

Table 5. Thermal Expansion Coefficients for Various Compositions in the HZT System.

Composition (mol%)			Thermal Expansion Coefficient	Ref.
H	Z	T	(10^{-6}/°C)	
63	0	37	0.5	1
61	3	36	-0.9	1
59	5	36	-1.0	1
58	8	35	-1.5	1
55	10	35	-1.8	1
52	13	35	-4.4	1
47	16	37	2.2	5
32	32	37	5.9	5
16	47	37	6.7	5
60	20	20	3.1	4

2.2.2.2 Measurements

Measurements of thermal expansion can be made on both the bulk material (linear thermal expansion) and the lattice or unit cell (axial thermal expansion).

For linear thermal expansion measurements, a dilatometer is used to monitor the change in length of a bulk sample when heat is applied. A factor to contend with in using a dilatometer is the expansion of the unit itself during the measurement. Usually, a standard with a known thermal expansion is run to calibrate the apparatus. Once the expansion of the apparatus is known, the thermal expansion of a test sample can be determined by adding the apparatus expansion to the measured expansion. The final equation for determining the expansion of a material using a single rod dilatometer is then:

$$\Delta L_{sample} = (\Delta L_{standard} - \Delta L_{stand.\ meas.}) + \Delta L_{sample\ meas.} \qquad (38)$$

where ΔL is the change in length. As long as the conditions are identical for the calibration run and the sample run, the final expansion of the material can accurately be determined. To assure identical conditions, a dual rod dilatometer can be used which measures the standard and the test sample simultaneously.

For axial thermal expansion measurements, hot-stage x-ray units are used. The lattice parameters are determined at various temperatures and the parameter change versus temperature is plotted to give the axial thermal expansion. For isotropic materials, the axial thermal expansion is equal to the linear thermal expansion. For anisotropic orthonormal polycrystalline materials:

$$\bar{\alpha} = \tfrac{1}{3} (\alpha_a + \alpha_b + \alpha_c) \qquad (39)$$

where $\bar{\alpha}$ is the linear thermal expansion coefficient and α_a, α_b, and α_c are the axial thermal expansion coefficients. For non-orthorhombic systems, (e.g., monoclinic), the conversion between axial and linear thermal expansion coefficients requires matrix transformations.

2.2.3 Fracture Strength and Toughness

The fracture behavior of a structure depends on many factors besides the inherent strength of the material. Factors such as flaws, microstructure, and environment strongly influence the fracture mechanics. This section will discuss the strength and toughness of materials and address the factors which influence the fracture behavior.

The theoretical cohesive strength of a solid is governed by the strengths of the bonds between constituent atoms. Fracture occurs when the separation between atoms along a plane reaches a critical distance whereby the attractive forces no longer can bind the atoms. This critical distance and the energy required to create new surfaces are used in determining the theoretical strength of a solid. For covalently

bonded solids, the attractive forces can be approximated by the Morse potential.[60] The cohesive strength is then:

$$\sigma_c = \sqrt{\gamma E/4a} \qquad (40)$$

where γ is the surface energy, E is the elastic modulus, and a is the separation between atoms. For an elastic material, the theoretical strength is of the order of 2×10^6 psi (14 GPa).

In general, measured strengths are orders of magnitude lower than theoretical strengths. This difference is attributed to flaws which are present in all materials. Flaws reduce the strength of a structure by introducing stress concentration effects, residual stress effects, or a combination of both.

Inglis[61] was the first to show that flaws in the form of fine cracks act as stress concentrators. When a stress is applied perpendicular to the fine cracks within a structure, the stress is magnified at the crack tips. The resultant concentration of stresses causes the structure to fracture at applied stresses which are much lower than expected from considerations of theoretical strengths. Griffith[62] used the stress analysis of Inglis to show that the fracture strength of a flawed structure is:

$$\sigma_f = \sqrt{2\gamma E/\pi c} \qquad (41)$$

where c is the length of the critical flaw. Griffith assumed that in brittle fracture, the material is entirely elastic and that at failure, the strain energy around the crack equals the energy to create the new surfaces. Irwin[63] extended the ideas presented in the Griffith theory to include the plastic nature of materials and to take into account energy lost to mechanisms other than the creation of surface area. Irwin showed that the fracture strength of a material is:

$$\sigma_f = \sqrt{G_c E/\pi c} \qquad (42)$$

where G_c is the elastic energy release rate. G_c becomes equal to 2γ for a purely elastic material having only surface energy dissipation at fracture.

The term G_c is related to the fracture toughness (K_{1C}). The fracture toughness, also called the critical stress intensity factor, is the resistance of a material to crack propagation. A structure will catastrophically fail when the stress intensity factor reaches K_{1C}. The applied stress is then:

$$\sigma_f = \frac{K_{1C}}{Y\sqrt{c}} \tag{43}$$

where Y is a geometrical constant and c is the critical flaw size.

As Equation (43) points out, the fracture strength of a structure is related to the fracture toughness of the material and to the critical flaw size. The fracture toughness is considered by many to be a material property that is dependent upon microstructural effects (e.g., second phases, grain size, porosity, grain boundaries, microcracks, agglomerates, etc.) and environmental effects (e.g., temperature, atmosphere, stress distribution, etc.). Consequently, the fracture strength is influenced by these effects also. Flaws, which are the principal source of fracture, however, dominate the fracture behavior.[64]

Detailed reviews of the various types of flaws and their effect on the fracture behavior of ceramics have been made by Evans[64] and by Singh.[65] As Evans points out, three categories of failure can be distinguished: (1) failure from preexistent flaws, (2) failure from the coalescence or joining of microcracks, and (3) failure from the formation and coalescence of cavities.[64] A brief description of the various failure mechanisms and flaw types in ceramic materials follows as well as an examination of their relationship to strength.

Preexistent flaws are those that are present in a structure prior to the application of a stress. They can be separated into two types, internal and surface. Internal flaws (e.g., inclusions, voids, pores, etc.) are generally introduced during fabrication. Surface flaws, which tend to dominate the fracture behavior, occur in the as-fired condition or may be introduced during polishing. Inclusion-initiated failure usually

involves a combination of stress concentration and residual stress influences, while void-induced failures are related to stress concentration effects and surface crack failures are a consequence of residual stresses.[64-65]

Inclusions are a major source of premature fracture. In general, they introduce residual stresses as a result of a mismatch in the thermal expansion coefficients of the matrix and the inclusion. The residual stress can be expressed as:

$$\sigma_r = -2\sigma_t = -(\alpha_m - \alpha_i)\Delta T \Big/ \left(\frac{1+\nu_m}{2E_m} + \frac{1-2\nu_i}{E_i}\right)\left(\frac{R}{r}\right)^3 \qquad (44)$$

where σ_r and σ_t are the radial and tangential stresses, respectively; i and m refer to inclusion and matrix; ΔT is the difference between room temperature and the maximum temperature below which stresses are not relaxed during cooling; R is the radius of the inclusion; and r is the radial distance from the inclusion.[65] Depending on the thermal expansion coefficients, elastic moduli, and toughnesses of the matrix and inclusion, a variety of fracture mechanisms can occur. (For example, when an inclusion has a thermal expansion coefficient that is much lower than that of the matrix, residual tensile stresses occur in the matrix. These stresses when large enough produce radial cracks that severely degrade the strength of the structure.) A schematic diagram of the various inclusion-initiated fracture mechanisms is presented by Evans.[64] Some fracture modes tend to be more detrimental to the strength than others. Not all inclusions when added to a material, however, degrade the strength. Transformation toughened materials and glass-ceramics have second phase inclusions that actually enhance the strength.[66] The strengthening effects of inclusions, however, will not be addressed here.

Voids or large pores are a frequent source of failure in sintered ceramics. They usually serve as stress concentrators by acting in conjunction with other flaw types (e.g., extending surface cracks or microcracks).[64] The reduction in strength depends

on the size, shape and distribution of the porosity. The strength generally decreases with increasing pore size. The relation between the strength and the amount of porosity is empirically given by:

$$\sigma_p = \sigma_o e^{-BP} \qquad (45)$$

where σ_p and σ_o are the strengths with and without pores, B is a constant that depends on the distribution and morphology of the pores, and P is the fractional pore content.[65,67-70]

Surface flaws tend to strongly influence fracture behavior. A large number of as-fired surface flaws are introduced in virtually every ceramic fabrication process. In many instances, it is necessary to grind or polish the surface to eliminate these flaws. The finishing process, however, tends to introduce surface cracks which may also act as failure-initiating sites. These surface cracks originate from the residual stresses that accompany the localized deformation in the vicinity of the grinding particles. A correlation between the grit size of the polishing media and the crack size exists. Likewise, a correlation exists between the grit size and the fracture strength. The strengths tend to be higher for finer grit polishes.[64-65]

Preexistent flaws, whether internal or at the surface, generally influence fracture behavior at low and intermediate temperatures (i.e., in temperature regions where fracture is elastic). Strength in this region is either constant or increases slightly with temperature. At high temperatures where plastic deformation occurs, the influence of preexistent flaws in reduced.[65] The stress concentration and the residual stress effects introduced by flaws are lessened when plastic deformation occurs.

Failure by microcrack coalescence also occurs in the low and intermediate temperature range. Microcracks (which form in grain boundaries as a consequence of thermal expansion anisotropy) generally act to decrease the strength. The initial formation of microcracks does not lead to failure. Fracture in microcracked structures occurs when microcracks coalesce or join to form a crack of critical size. Both the

orientation and the concentration of microcracks strongly influence the fracture behavior. For example, dilutely microcracked materials may experience no degradation in strength, and highly microcracked materials with the proper relative crack orientation, may enhance strength by stopping crack propagation (microcrack toughening).[71-72]

The fracture process at high temperatures usually involves nonlinear deformation. Generally, the strength decreases as the temperature is elevated. Failure occurs as a result of the formation and coalescence of cavities. Cavity sites initiate from the corners of grains, from grain boundaries, from local deviations in the chemical composition of the grain boundary phase or from thick amorphous regions within the grain boundary. Cavities grow by diffusion and/or viscous deformation. Coalescence or the joining of cavities progresses until fracture occurs. The degradation of the strength is dependent upon the diffusive transport of material from the growing cavity and the nature of the grain boundary phase which forms the cavity.[65]

2.2.3.1 Systems

Several of the major points of fracture mechanics will be illustrated by examining the effects of various additives to hafnia and zirconia.

A large number of studies on ZrO_2-based materials have produced considerable amounts of data on fracture strength and toughness. Since the data for HfO_2-based materials is limited, emphasis here will be upon ZrO_2-based compositions. The range of fracture strengths is from 170[73] to 1500 MPa[74] depending on the composition, purity, phases present, and fabrication technique. Toughnesses range from 1.8[75] to 12 MPa·$m^{\frac{1}{2}}$.[76]

The strongest, toughest materials are tetragonal ZrO_2 polycrystals which are predominantly single phase.[74] For grain sizes less than 0.1 to 0.3 μm, the tetragonal

phase is metastable and will transform to the monoclinic phase when a stress is applied, thereby transformation toughening the material.[77] Strength and toughness values for ZrO_2 with optimum metastabilizing concentrations of MgO or Y_2O_3 are in the range 1200 to 1500 MPa and 10 to 12 MPa·$m^{\frac{1}{2}}$.[74,78-81]

The weakest, least tough materials are fully stabilized cubic zirconias. The toughness drops to 1.8 MPa·$m^{\frac{1}{2}}$ and the strength to 170 MPa.[73,81]

Strength and toughness values increase from those of cubic zirconia for mixtures of the cubic and monoclinic phases (250 MPa and 3.7 MPa·$m^{\frac{1}{2}}$) and the tetragonal and cubic phases (650 MPa and 7.1 MPa·$m^{\frac{1}{2}}$).[8] Pure monoclinic ZrO_2 and mixtures of the monoclinic and tetragonal phases have strength and toughness values that fall intermediate between these.

Metastable tetragonal hafnia has shown toughness values of the order of 10 MPa·$m^{\frac{1}{2}}$ for compositions with 46% tetragonal phase.[82-83] (Strength values for tetragonal hafnia compositions should be comparable to those of metastable tetragonal zirconia.[83]) As the amount of monoclinic phase increases, the toughness decreases similar to the ZrO_2 situation. As 100% monoclinic HfO_2 is approached, the toughness drops to approximately 2 MPa·$m^{\frac{1}{2}}$.[82] This value is much less than that of 100% monoclinic ZrO_2. (The strength of monoclinic HfO_2 should be much less than that of monoclinic ZrO_2 since extensive microcracking occurs in HfO_2.)

Titanate compositions in the HfO_2-TiO_2 system were studied for fracture strength by Hoagland et. al.[84] and Simpson.[1] These studies showed that $HfTiO_4$ weakens the material dramatically. Table 6 presents the data from the two studies. The strengths for compositions between 30 and 40 mol% were found to be the lowest. This range coincides with the low thermal expansion coefficient range. The low strengths can be attributed to the extensive microcracking which results from the anisotropic thermal expansion.[84]

Table 6. Strength of Compositions in the HfO_2-TiO_2 System.

Composition (mol% TiO_2)	Strength (MPa)	Reference
30	44.3	84
30	30.5	1
37	40.9	84
37	34.0	1
40	41.8	84
45	82.4	84
50	64.6	84

The fracture strength of 61 mol% HfO_2-3 mol% ZrO_2-36 mol% TiO_2 was found to be 36.4 MPa.[84] This represents a slight increase from the base composition 63 mol% HfO_2-37 mol% TiO_2.

The effect of temperature on the strength and toughness of a typical fluorite material (partially stabilized zirconia) is illustrated in Figure 24. A general decrease in both the strength and the toughness with increasing temperature is observed. Fluorite materials with low thermal expansion coefficients, on the other hand, typically exhibit an increase in strength with temperature to an upper critical temperature (e.g., Figure 25). This increase in strength results from the closing of microcracks.

2.2.3.2 Measurements

A number of techniques have been developed to measure fracture strength and toughness of brittle ceramics. A summary of the various techniques for determining strength has been compiled by Evans[86] and Quinn et. al..[87] Techniques for determining toughness can be found in a number of studies.[88-99]

Strength measurement techniques consider such factors as load direction (i.e., compression or tension), specimen configuration (e.g., three-point bend, four-point bend, double cantilever beam, compact tension, double torsion, tapered cantilever

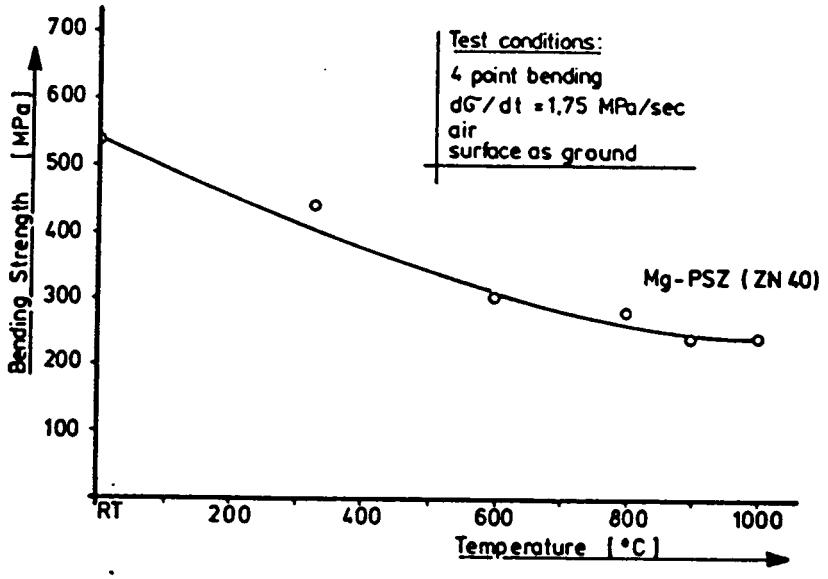

(a)

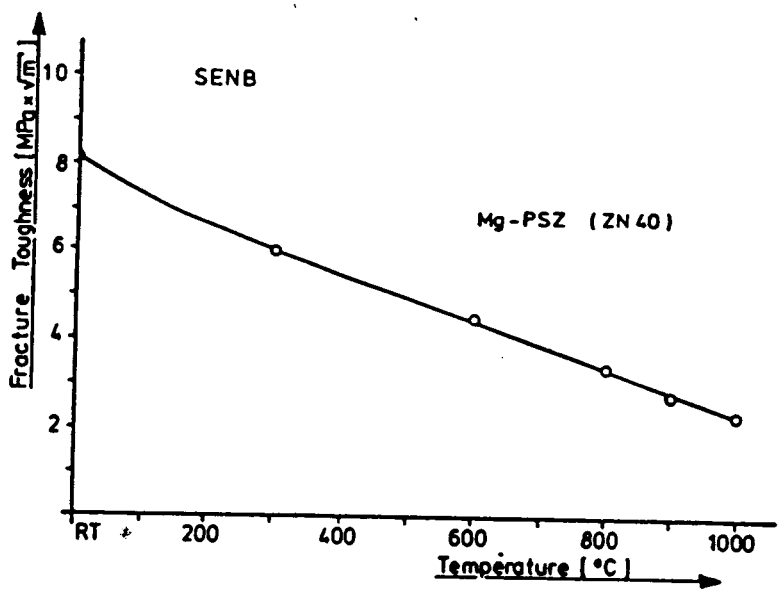

(b)

Figure 24. Effect of temperature on (a) strength and (b) toughness of PSZ (Ref. 85).

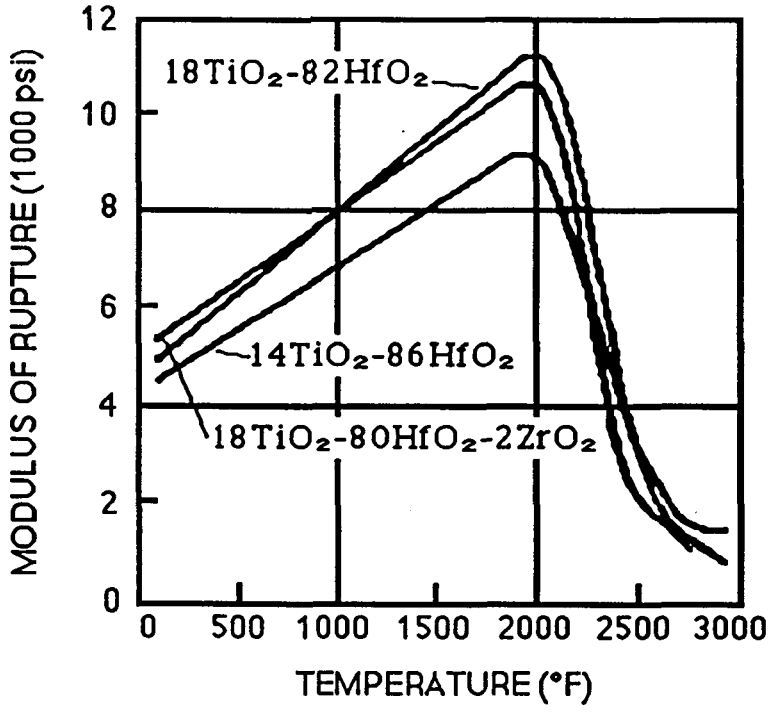

Figure 25. Effect of temperature on strength of three compositions in the HZT system (Ref. 1). Composition values are in weight percent.

beam, and constant moment),[86] specimen size, and surface finish (i.e., polished and indented or notched). Even though no standard method for determining strength has been established, variations of the four-point bend method are most often used in the literature. Although other methods of measuring strength have advantages, only the method and advantages of four-point bend measurements will be discussed here.

2.2.3.2.1 Fracture Strength

Figure 26 shows a schematic drawing of the stress application in a four-point bend fixture. The top surface of the specimen is put into tension (the bottom in compression) when moments are applied to the bar ends. The fracture strength (also called the modulus of rupture, four-point bend strength, or fracture stress) is

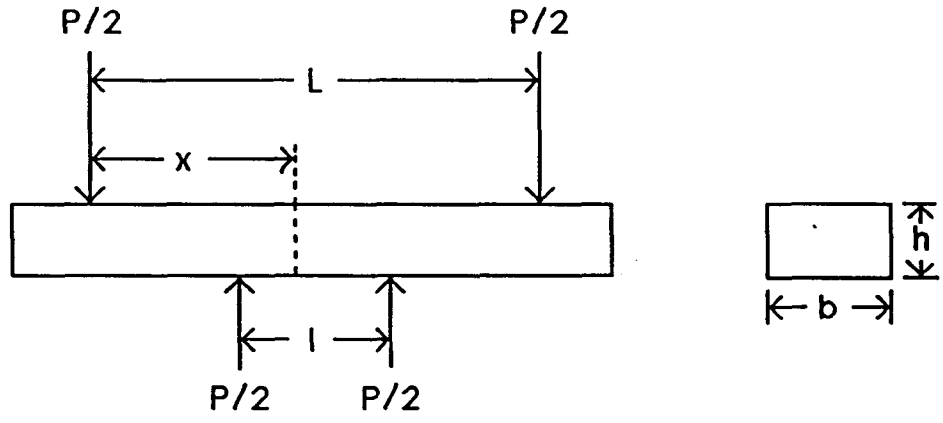

Figure 26. Schematic drawing of the load application in a four-point bend fixture.

determined from the applied load at fracture, the bar dimensions, and the fixture dimensions according to the equation:

$$\sigma_{MOR} = \frac{3P(L-l)}{2(bh^2)} \tag{46}$$

where σ_{MOR} is the fracture strength, P is the applied load, L and l are the inner and outer spans between load points, b is the width of the bar, and h is the bar height or thickness. This equation can be derived as follows:

$$\sigma_{MOR} = \frac{Mc}{I} \tag{47}$$

where:

$$M = \frac{P}{2}x - \frac{P}{2}\left(x - \frac{(L-l)}{2}\right) = \frac{P(L-l)}{4} \tag{48}$$

$$c = \frac{h}{2} \tag{49}$$

$$I = \int_{-h/2}^{h/2} y^2\, dA = b\int_{-h/2}^{h/2} y^2\, dy = \tfrac{1}{3}b\left[\frac{h^3}{8} + \frac{h^3}{8}\right] = \frac{bh^3}{12} \tag{50}$$

where M is the applied moment, x is some distance away from the outer span load point along the length of the bar, c is the distance away from the top surface to the plane where there is zero compression and tension, I is the moment of inertia, y is a

distance in the direction of the thickness, and A is the cross sectional area of the bar. Substituting Equations (48)-(50) into Equation (47) gives Equation (46).

Factors such as bar sizes, fixture design, fixture dimensions, and bar surface finish are still being investigated in an effort to standardize the four-point bend method. Sample sizes approximately 5.1 cm x 0.6 cm x 0.3 cm and outer span to inner span ratios of 3.0 are most often used in the literature. Size and span ratios have a bearing on the measured strength in that they affect the flaw distribution. Fixture designs attempt to give uniform point load applications and precise bar alignments. Most designs use rods to achieve point load applications and to allow fixture movement for uniform loading.

Surface flaws of suitable size are usually placed on the tensile side of a four-point bend specimens in order to give a controlled fracture. Fracture initiates at the site of this flaw because it tends to be the worst in the specimen. Fracture strength values for specimens with controlled flaws tend to have less scatter than values for specimens without controlled flaws. There is, however, a consequent reduction in the measured fracture strength when large flaws are intentionally introduced.

The major disadvantages of the four-point bend method (and flexure test methods in general) are: (1) Only small volumes of material are exposed to the full applied tensile stress. This minimal exposure may lead to inaccurate strength estimates. (2) Strength measurements are highly dependent upon the surface finish of the specimens. (3) Biasing of the data can occur as a consequence of which statistical analysis method is selected, the inadvertent elimination of weaker specimens during sample preparation, and the presence of large flaws such as pores that reduce the effective cross sectional area.[87] The major advantage of the four-point bend method over other flexural methods is that the volume of material exposed to uniform tensile stresses is the largest (i.e., a constant tensile stress is present on the specimen surface within the inner loading pin span).

2.2.3.2.2 Fracture Toughness

Fracture toughness measurements are now widely made using indentation techniques. These techniques fall into two main categories: (1) tests in which K_{1C} is determined from direct measurements of crack size as a function of indentation load and (2) tests in which the indentation crack serves as a controlled flaw in a bend specimen, so that K_{1C} is determined by a strength measurement.[99] Although the methods in both categories tend to give reproducible measurements, their accuracy levels are about 30 to 40% of the true K_{1C} values for most materials.

A recently developed indentation technique, however, has proven to be both reproducible and accurate. This technique was developed by Cook and Lawn[99] and is a hybrid of techniques from both categories. Certain problems associated with other indentation techniques are by-passed; namely, (1) the determination of the elastic modulus to hardness ratio (E/H) and (2) the applicability of the E/H ratio to non-ideal elastic/plastic materials. Cook and Lawn have found that when two or three Vickers indentations are placed within the inner span of a four-point bend specimen (see Figure 27), all experience near-identical stress histories during the bend test, but only one fails. The critical crack length (c_m) can then be determined from the surviving indentations, and using the critical crack stress (σ_m), the fracture toughness can be determined from:

$$K_{1C} = A\,\sigma_m c_m^{\frac{1}{2}} + B \qquad (51)$$

where A = 2.02 and b = -0.68 MPa·$m^{\frac{1}{2}}$.[99] The calibration curve in Figure 28 was used to determine A and B. As the figure shows, the K_{1C} values for a wide variety of materials fit the equation. Major benefits of the technique are: (1) it can be used to measure K_{1C} at elevated temperatures and (2) fracture strengths are obtained at the same time.

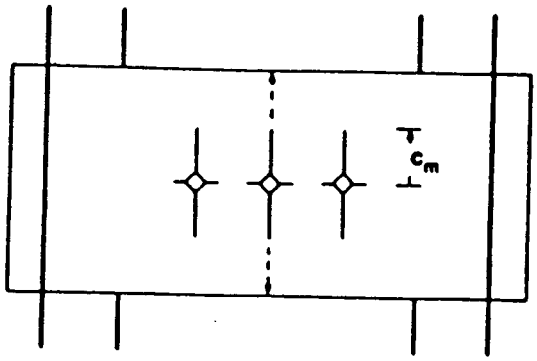

Figure 27. Indentation configuration for technique used to determine fracture toughness (Ref. 99).

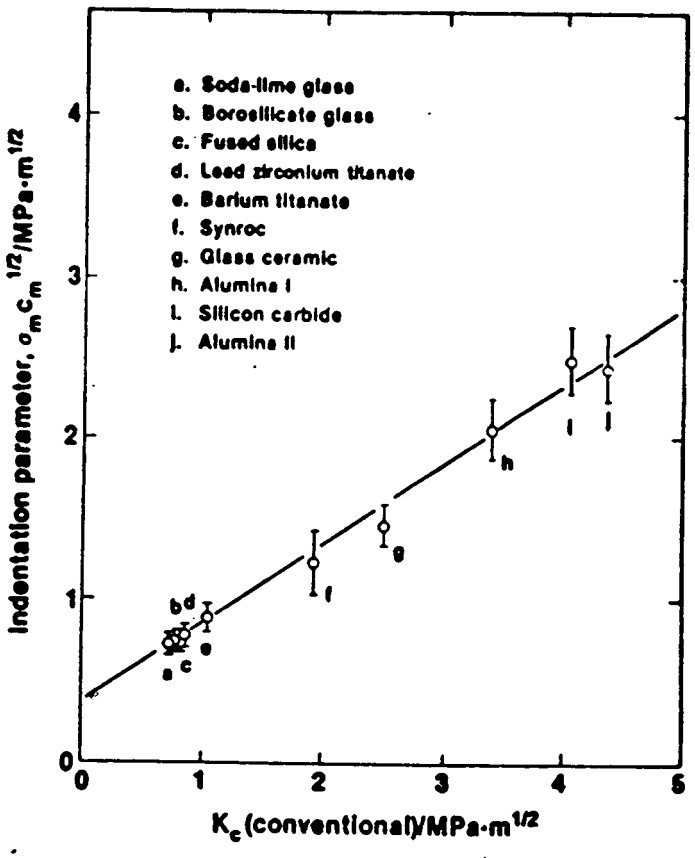

Figure 28. Calibration curve for fracture toughness method of Cook and Lawn (Ref. 99).

3. EXPERIMENTAL PROCEDURES

3.1 Compositions and Batching

The literature search suggested that compositions with 60 mol% or more hafnia and moderate concentrations of zirconia and titania would give the best thermal expansion, thermal shock resistance, and strengths possible in the system. On the basis of this knowledge, the following six compositions (in mol%) were selected for the preliminary investigation:

1. 60% HfO_2, 35% ZrO_2, 05% TiO_2
2. 60% HfO_2, 30% ZrO_2, 10% TiO_2
3. 60% HfO_2, 25% ZrO_2, 15% TiO_2
4. 60% HfO_2, 20% ZrO_2, 20% TiO_2
5. 60% HfO_2, 15% ZrO_2, 25% TiO_2
6. 60% HfO_2, 10% ZrO_2, 30% TiO_2

Early experiments with materials prepared with these compositions allowed the last two compositions to be eliminated from consideration. The remaining compositions exhibited the best sintering characteristics and offered the highest potential of delivering the properties sought. For the compositions exceeding 20 mol% titania, sintering was seriously impaired.

The starting powders were high purity hafnia[a], zirconia[b], and titania[c]. The impurity content of each is given in Appendix I. Six hundred gram batches of each composition were mixed by milling in plastic containers for one hour. Subsequently,

---

[a] Teledyne Wah Chang Albany, Albany, OR 97321
[b] Magnesium Elektron, Inc., Fleming, N. J. 08822
[c] J. T. Baker Chemical Company, Phillipsburg, N. J. 08865

three processing techniques were performed on each composition in order to make bar samples.

3.2 Sample Preparation

The three techniques used to prepare samples are described below.

3.2.1 Reaction-Sintered Powders (T_1)

Two weight percent Polytran FS[d] in distilled water was added as binder to four hundred grams of the mixed as-received high purity powder. The powder was dried and sieved through a 200 mesh screen. Pellets 2.54 cm in diameter were then pressed uniaxially in a Denison press[e] to 12,000 psi (82 MPa), reaction sintered to 1700°C for 5 hours in a Remey gas furnace[f], crushed, milled in a steel ball mill, chemically treated with HNO_3 and HCl to remove metal contamination introduced by ball milling, then further ball milled using ZrO_2 balls for 48 hours. Two hundred grams of the reaction-sintered powder were then pressed uniaxially in a tungsten carbide lined die[g] using a Carver press[h] into the form of 5.2 cm x 0.6 cm x 0.3 cm bars at 13,000 psi (87 MPa). Four weight percent Carbowax[i] dispersed in acetone was used as the binder. The bars were then pressed isostatically to 30,000 psi (207 MPa) in rubber bladders using an Autoclave press.[j]

The bars were cut in half using a stainless steel razor blade, taken to 500°C for ½ hour to burn out the binder, then fired to 2200°C for 4 hours in a Brew vacuum

---

[d] Dawes Laboratories, Inc., Chicago, IL
[e] The Denison Engineering Company, Columbus, OH
[f] Remey, manufacturer unknown
[g] Staats and Staats, Inc., Irwin, PA 15642
[h] Fred S. Carver, Inc., Summit, N. J.
[i] Union Carbide Corporation, N. Y., N. Y. 10017
[j] Autoclave Engineers, Inc., Erie, PA

furnace[k] at 10^{-6} torr. A 6 μm diamond finish was put on three sides, $\frac{1}{4}$ μm finish on the top surface, and the edges were bevelled. Three indents were made in most of the bars using a Vickers microhardness indenter with a load of 40 lbs (178 N). Several bars were set aside in order to study the reduced state. The rest of the bars were oxidized in air at 1700°C for 12 hours.

3.2.2 As-Received Powders (T_2)

Four weight percent Carbowax dispersed in acetone was added to 200 grams of the mixed as-received powders. The powders were dried, sieved through a 200 mesh screen, and pressed uniaxially into 5.2 cm x 0.6 cm x 0.3 cm bars at 13,000 psi (87 MPa). The bars were pressed isostatically to 30,000 psi (207 MPa), cut in half, presintered to 1700°C in air for $2\frac{1}{2}$ hours, then vacuum fired to 2200°C for 4 hours. Most of the bars were subsequently oxidized in air at 1200°C for 6 hours. All bars were polished and bevelled. Bars used in the fracture studies were indented.

3.2.3 Plasma-Sprayed Powders (T_3)

Two hundred grams of reaction sintered powder were passed through the high temperature plasma (H_2 and N_2 gas mixture) of an 80 kW METCO 7M plasma spray unit[m] operating at 50% power, then quenched into distilled water to effect rapid solidification. The powders were then calcined at 950°C in air for 4 hours and vacuum hot pressed[n] at 2000°C for 2 hours in graphite molds[o] under a pressure of 6.33 tons (27.8 MPa). The 5.2 cm diameter wafers were cut into bars 2.5 cm x 0.3 cm x 0.15 cm using a high speed diamond saw and polished. Several bars were oxidized in air at 1200°C for 6 hours.

---

[k] Richard D. Brew and Company, Concord, N. H. 03301
[m] METCO, Inc., Westbury, L-I, N. Y.
[n] GVA Corporation / Vacuum Industries Division, Somerville, MA
[o] ATJ grade carbon, Union Carbide Products Division, Cleveland, OH

3.3 Property Measurements

Three properties were investigated: (1) electrical conductivity, (2) thermal expansion, and (3) fracture strength and toughness. Each of these properties is important in understanding the effect that titania has in the HZT system and is pertinent to applications in heat exchangers and electric heaters.

3.3.1 Electrical Conductivity

Electrical conductivity measurements were made on bars prepared from as-received high purity powders. Platinum[p] electrodes were painted 0.5 cm apart and allowed to dry. Bars approximately 2.5 cm x 0.25 cm x 0.15 cm were mounted in the experimental apparatus shown in Figure 29 by wrapping the Pt-30%Rh[q] leads around the electroded ends. The apparatus was then heated to 1700°C. Resistance measurements were made while the furnace self-cooled (20 to 40°C/min) using a Wayne Kerr Automatic LCR meter[r] at 10kHz. The electrical resistance for each composition was measured from 1700°C down to approximately 400°C in air (P_{O_2} = 21 kPa), and in premixed gasses[s] of 1.0% O_2 in Ar (P_{O_2}= 10 kPa) and 9.55% CO in CO_2 (P_{O_2} = 10^{-2} to 10^{-31} kPa). The electrical conductivity was determined using the equation:

$$\sigma = \left(R \frac{A}{l}\right)^{-1} \qquad (52)$$

where σ is the total conductivity, R is the measured resistance, A is the bar cross sectional area, and l is the distance between electrodes.

---

[p] Electro-science Laboratories, Inc., Pt paste No. 5545, King of Prussia, PA 19406
[q] Electro-science Laboratories, Inc., King of Prussia, PA 19406
[r] Wayne Kerr LCR meter 4225, Woburn, MA 01801
[s] Air Products and Chemicals, Inc., Tamaqua, PA 18252

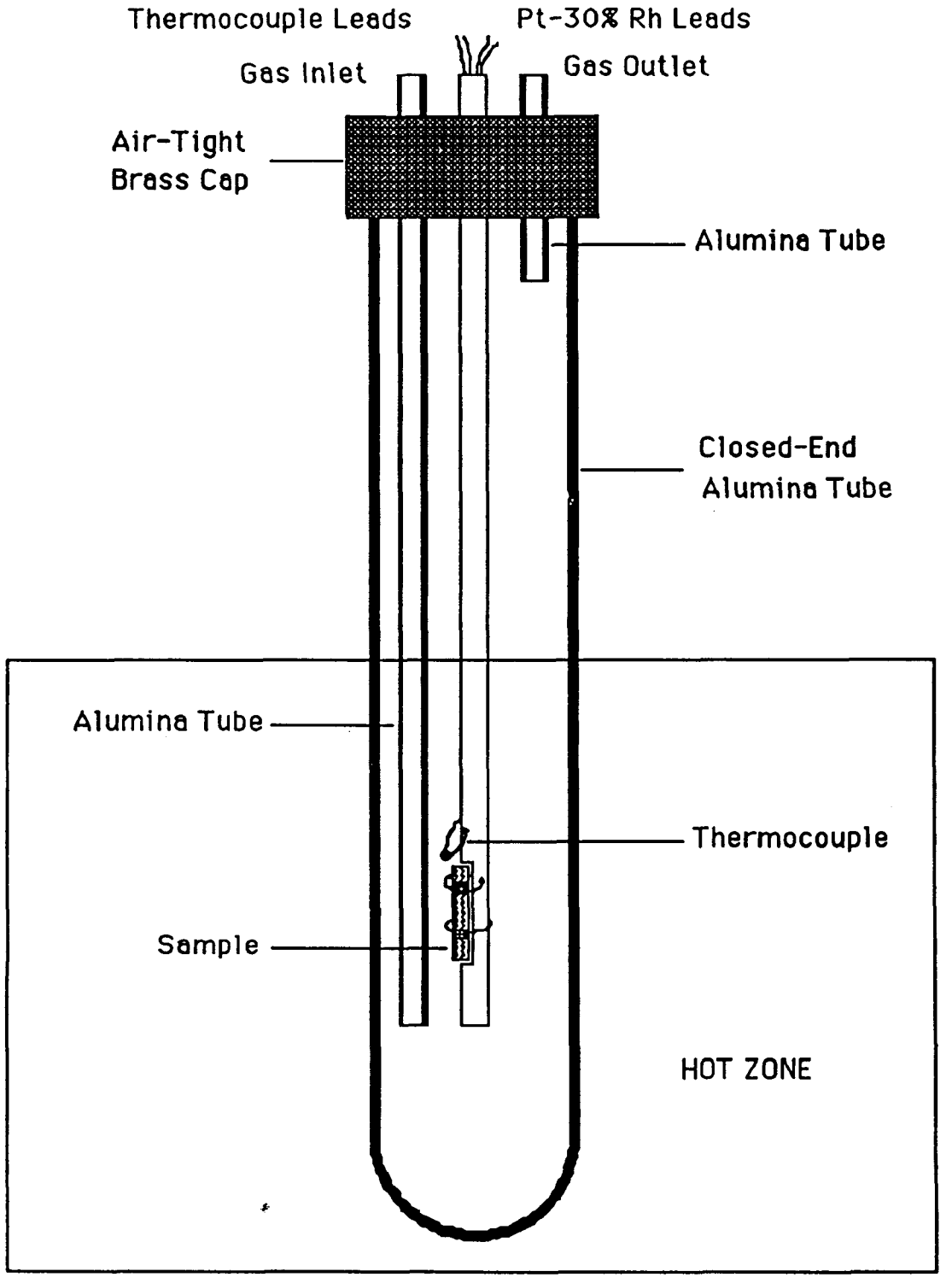

Figure 29. Schematic diagram of experimental apparatus used in obtaining the electrical resistance of the HZT bars.

3.3.2 Thermal Expansion

Thermal expansion measurements were made using the standard dilatometer set-up shown in Figure 30. The set-up consisted of a Theta 18 inch alumina specimen holder assembly[t] mounted to an Orton dilatometer.[u] Bar samples approximately 2.5 cm x 0.3 cm x 0.2 cm prepared from as-received powders were mounted vertically in the sample holder and upon expansion pushed the center rod up. The transducer in the dilatometer, which sensed the rod movement, sent a signal to a Daytronic LVDT conditioner.[v] A chart recorder then plotted the sample expansion. The sample holder was inserted through the top of a Teresco furnace.[w] Measurements were made in air between room temperature and 1700°C. The heating and cooling rates were 2°C/min. The apparatus was calibrated by measuring the expansion of a known standard; namely, a single crystal sapphire having similar dimensions to the bars. Appendix II gives the thermal expansion of the standard. Each sample was cycled once to 1700°C prior to being measured. The thermal expansion for each composition was determined by adding the expansion of the apparatus determined from the standard calibration run to the measured expansion of the bars.

3.3.3 Fracture Strength and Toughness

Fracture strength measurements were made on bar specimens prepared from reaction-sintered (T_1), as-received (T_2), and plasma-sprayed (T_3) powders. Either Al_2O_3 or SiC four-point bend load fixtures having inner spans of 6.5 mm and outer spans of 19 mm were used. Several bars of each composition in both the oxidized and reduced state were loaded using either a floor model Instron[x] or the load cell

---

[t] Theta Industries, Inc., Port Washington, N. Y. 11050
[u] Orton, Columbus, OH 43201
[v] Daytronic LVDT Conditioner Model 3130, Miamisburg, OH 45342
[w] Teresco, Champaign, IL 61820
[x] Instron Model 1125, Canton, MA 02021

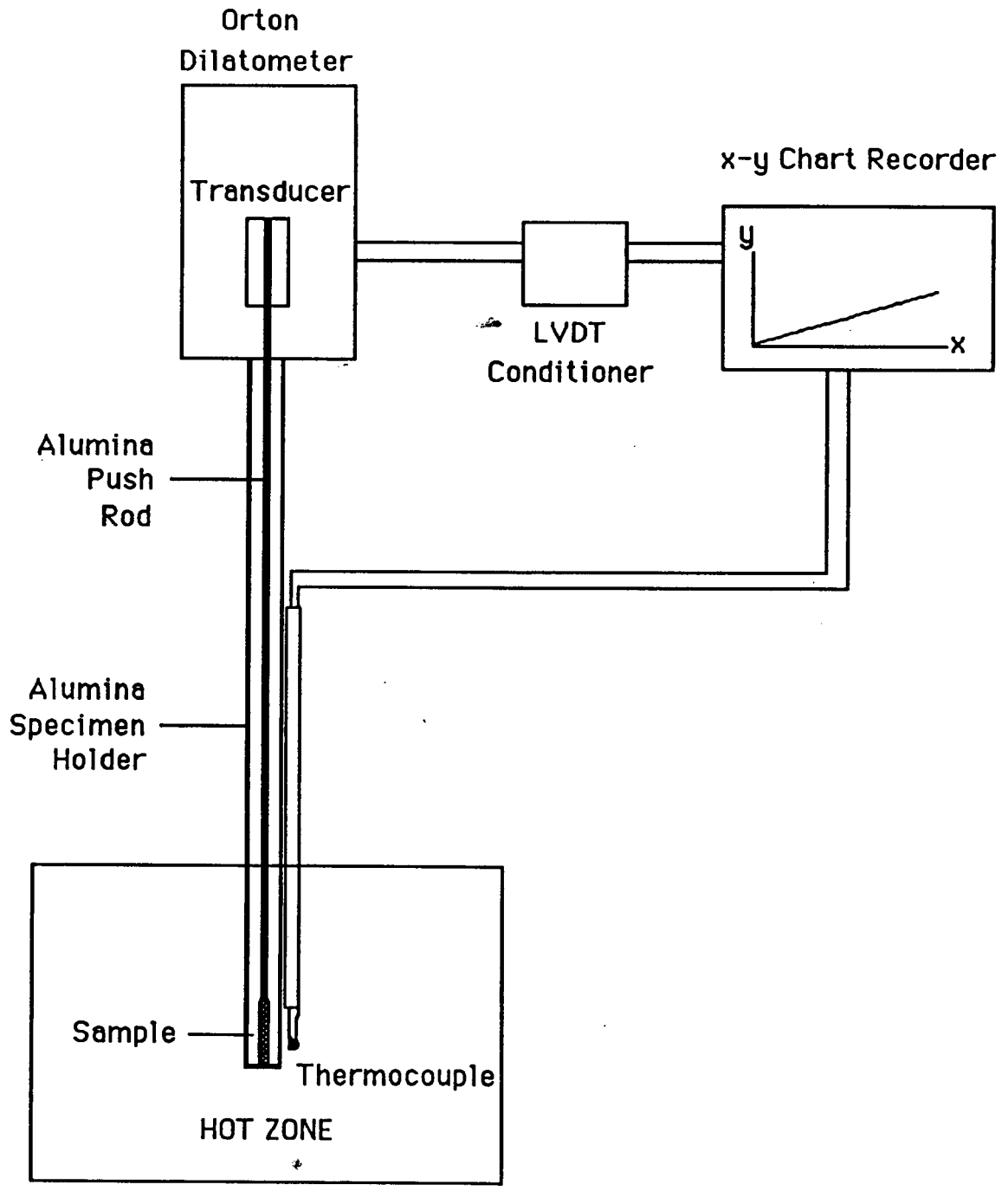

Figure 30. Schematic diagram of the dilatometer set-up used to determine the thermal expansion of the HZT bars.

apparatus shown in Figure 31. Both were equipped with furnaces for high-temperature measurements. The loading rate was about 0.5 cm/min. Room temperature measurements were made on both nonindented and triple Vickers indented bars. Measurements at 1000°C and 1400°C were made only on indented bars. The fracture toughness was also determined for indented bars at room temperature, 1000°C, and 1400°C. Surviving crack length measurements were made using an optical microscope.

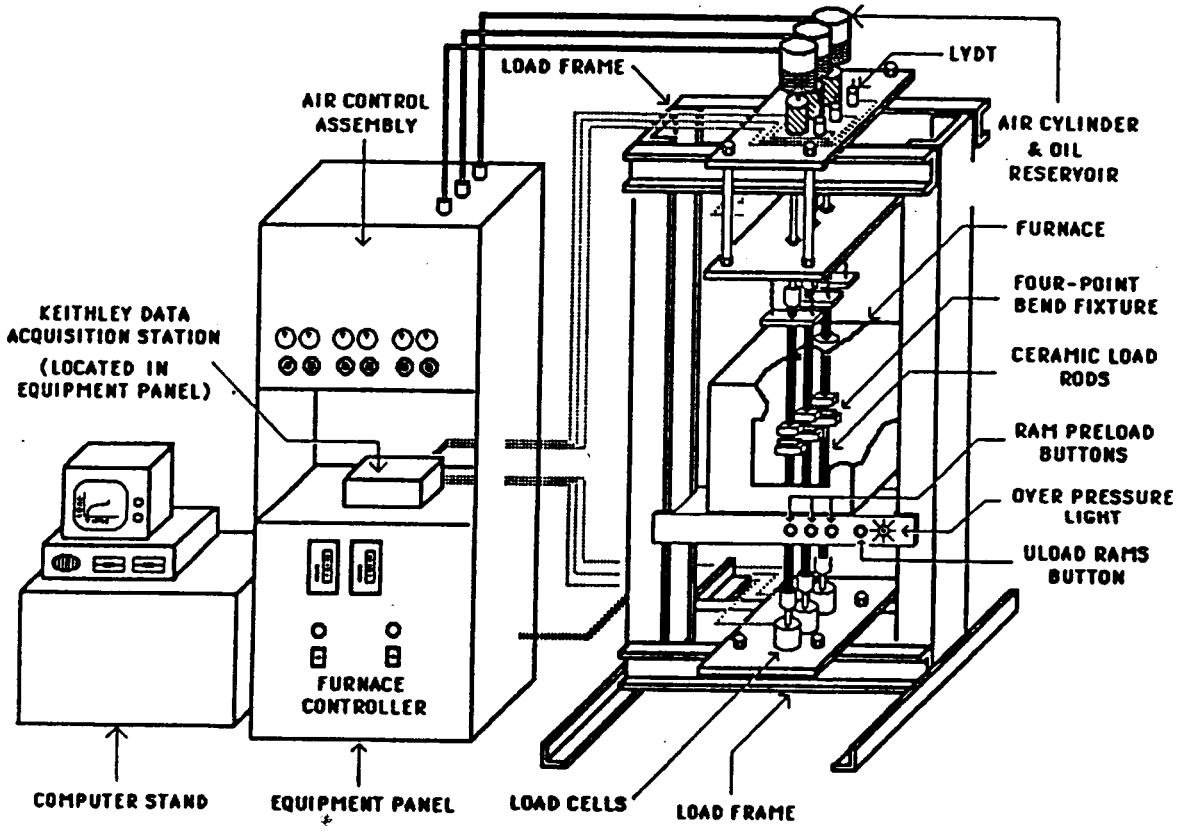

Figure 31. Schematic diagram of fracture load cell apparatus used in fracture strength and toughness study.

3.4 Analyses

Each of the four compositions prepared using the three different techniques was analyzed for starting particle size, density, sintered microstructure, and phases present.

3.4.1 Particle Size and Shape

Particle size analyses were performed at IMC in Terre Haute, IN using a Microtrac Particle Size Analyzer.[y] The Microtrac uses optical and laser light scattering to determine particle sizes. An ISI DS-130 SEM[z] equipped with an EDX was used to examine the particle shape and elemental make-up.

3.4.2 Densities, Mass Changes, and Length Changes

Densities were obtained by using an ethyl alcohol displacement technique. The dry mass and the suspended masses were determined using a Mettler balance.[aa] Mass changes were determined by measuring the mass before and after oxidation. Lengths of the green, fired and oxidized bars were also measured.

3.4.3 Sintered Microstructure

The sintered microstructure was examined using both optical and scanning electron microscopy. The average grain size was determined by the linear intercept method.

---

[y] Leeds and Northrup, North Wales, PA 19454
[z] International Scientific Instruments, Santa Clara, CA
[aa] Mettler Instrument Corp., Hightstown, N. J.

3.4.4 Phases

X-ray analyses were performed using a Debye-Scherrer powder camera[ab] and a Philips diffractometer.[ac] Monochromatic 40 kV, 30 mA copper K_α radiation was used for phase analyses. Ni-filtered 35 kV, 15 mA copper K_α radiation with a 11.4 cm diameter camera was used to determine accurate lattice parameters.

[ab] Norelco Type 17010200, Philips Electronic Instruments, Mount Vernon, N. Y.
[ac] Philips APD 3520, Philips Electronic Instruments, Inc., Nahwah, N. J. 07430

4. RESULTS AND DISCUSSION

The effects of TiO_2 on selected properties of HfO_2-rich mixed oxides in the HZT system were examined in detail. Analyses of the starting powders, sintered microstructures, densities, and final phases are presented first, followed by electrical conductivity, thermal expansion, and fracture strength and toughness studies. For ease of discussion, the following nomenclature is used for sample identification. Each group of samples is designated by composition (in mol% TiO_2), fabrication technique (e.g., made from: (1) reaction-sintered powders, (2) as-received powders, or (3) plasma-sprayed powders), and oxidation state (e.g., "ad" represents highly anion deficient or "ox," oxidized). For example, $5T_1$ox is an oxidized composition of 5 mol% TiO_2 made from reaction-sintered powders.

4.1 Powder Analyses

The average particle size, shape, and relative composition of the starting powders were determined for each composition and fabrication technique. Table 7 summarizes the particle size analyses. The analyses showed that the reaction-sintered (T_1) powders consisted of fine particles having an average size of 2 to 4 μm. The plasma-sprayed (T_3) and as-received (T_2) powders consisted of coarse particles having an average size of 16 to 23 μm. Figures 32-43 show scanning electron micrographs of the twelve starting powders. The T_1 and T_2 powders had very rough jagged surfaces, whereas the T_3 powders were round and smooth. EDX analyses showed qualitatively that the three sets of powders had the correct proportions of HfO_2, ZrO_2, and TiO_2 across the compositional series and that the T_1 and T_3 particles were homogeneous mixtures. No contaminations were detected in any of the powders.

4.2 Densities, Length Changes, and Mass Changes

The densities of samples at various stages of fabrication were determined for

Table 7. Particle Size Analyses of Starting Powders for HZT Compositions.

Composition	Average Particle Size (μm)
HfO_2	22.83
ZrO_2	1.82
TiO_2	1.20
$5T_1$	4.14
$10T_1$	2.90
$15T_1$	2.57
$20T_1$	3.84
$5T_2$	26.94
$10T_2$	18.29
$15T_2$	20.53
$20T_2$	26.93
$5T_3$	28.53
$10T_3$	16.08
$15T_3$	15.72
$20T_3$	17.43

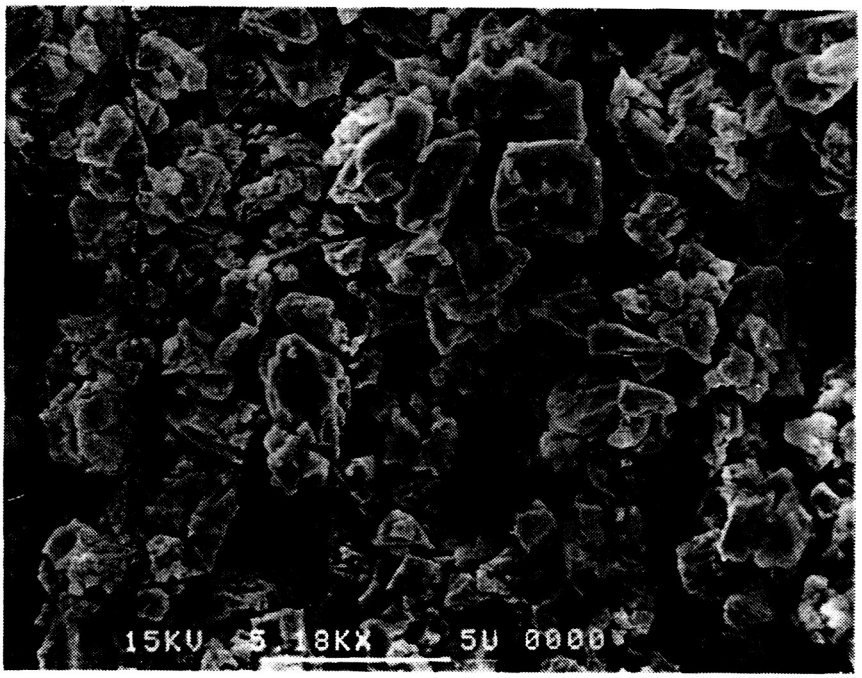

Figure 32. Scanning electron micrograph of reaction-sintered powder having 5 mol% TiO_2 ($5T_1$).

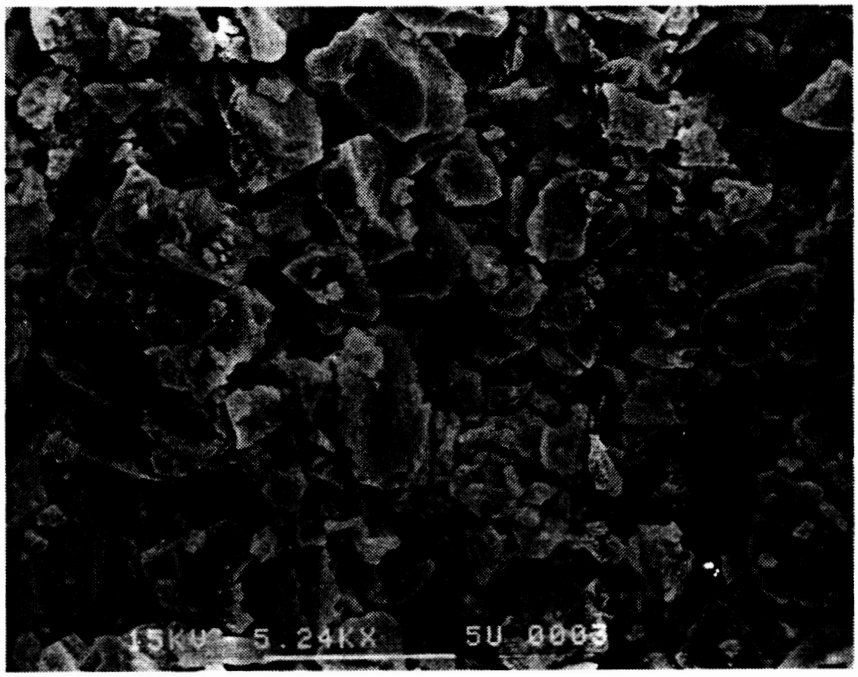

Figure 35. Scanning electron micrograph of reaction-sintered powder having 20 mol% TiO_2 ($20T_1$).

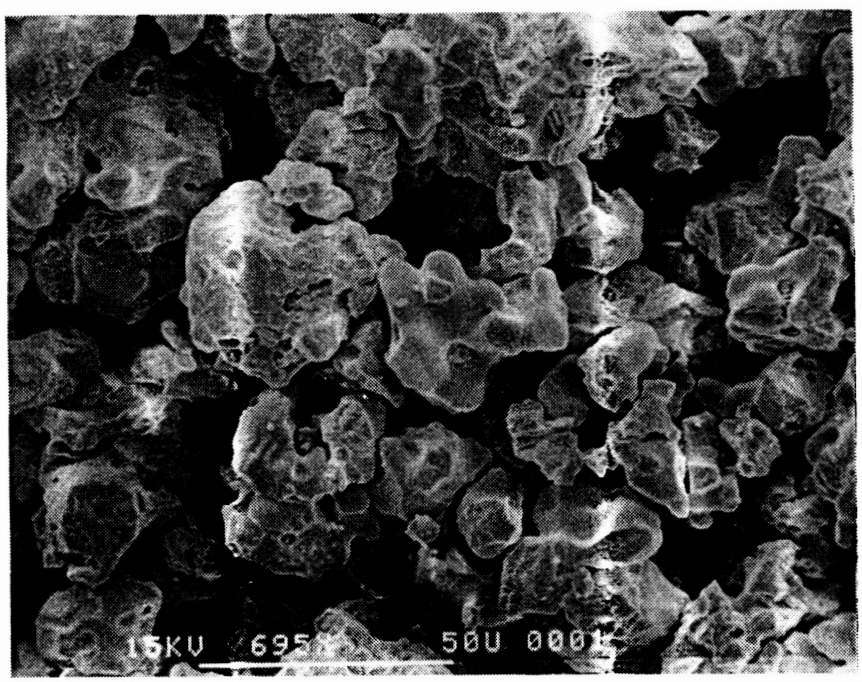

Figure 36. Scanning electron micrograph of as-received powder having 5 mol% TiO_2 ($5T_2$).

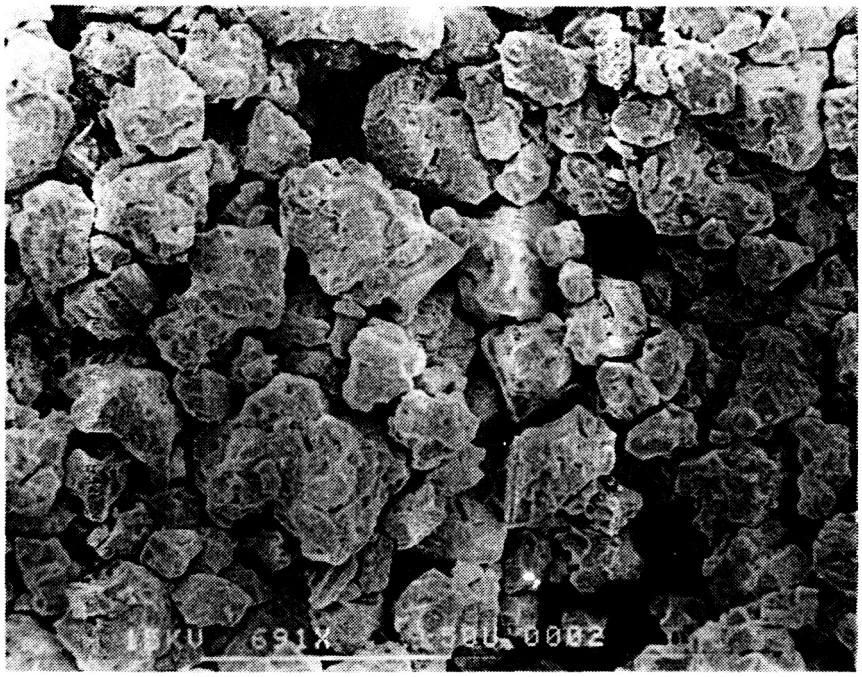

Figure 37. Scanning electron micrograph of as-received powder having 10 mol% TiO_2 ($10T_2$).

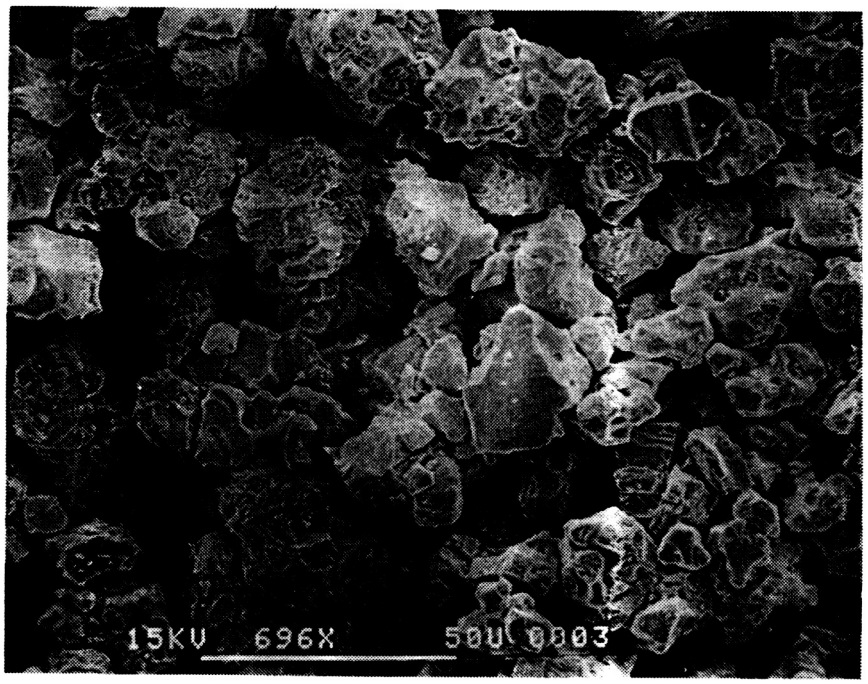

Figure 38. Scanning electron micrograph of as-received powder having 15 mol% TiO_2 ($15T_2$).

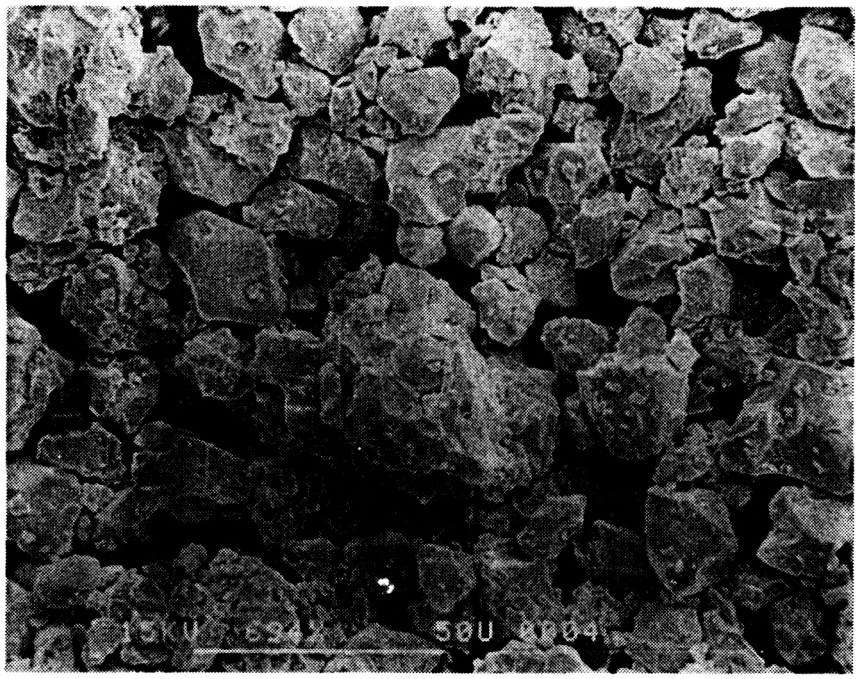

Figure 39. Scanning electron micrograph of as-received powder having 20 mol% TiO_2 ($20T_2$).

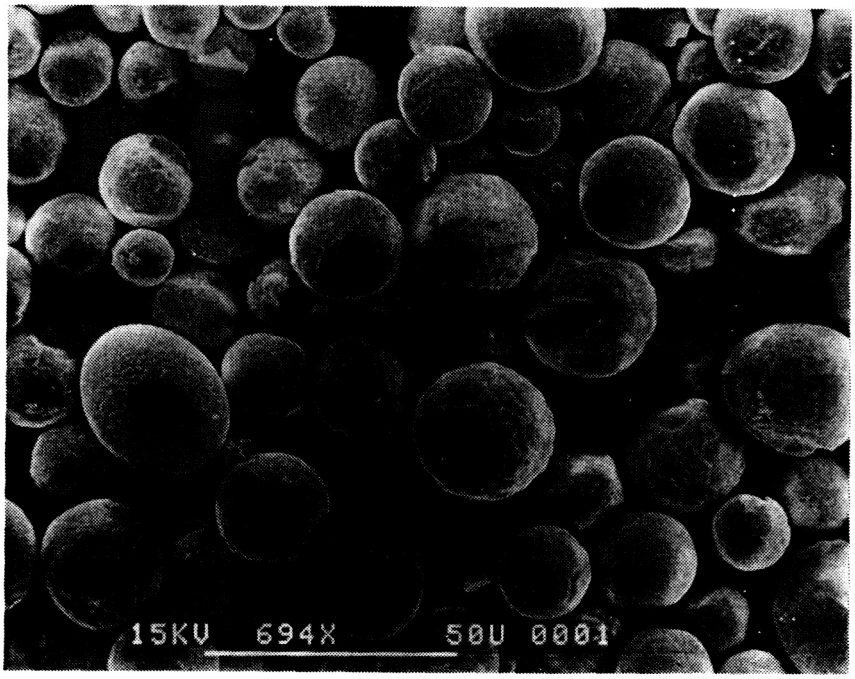

Figure 40. Scanning electron micrograph of plasma-sprayed powder having 5 mol% TiO_2 ($5T_3$).

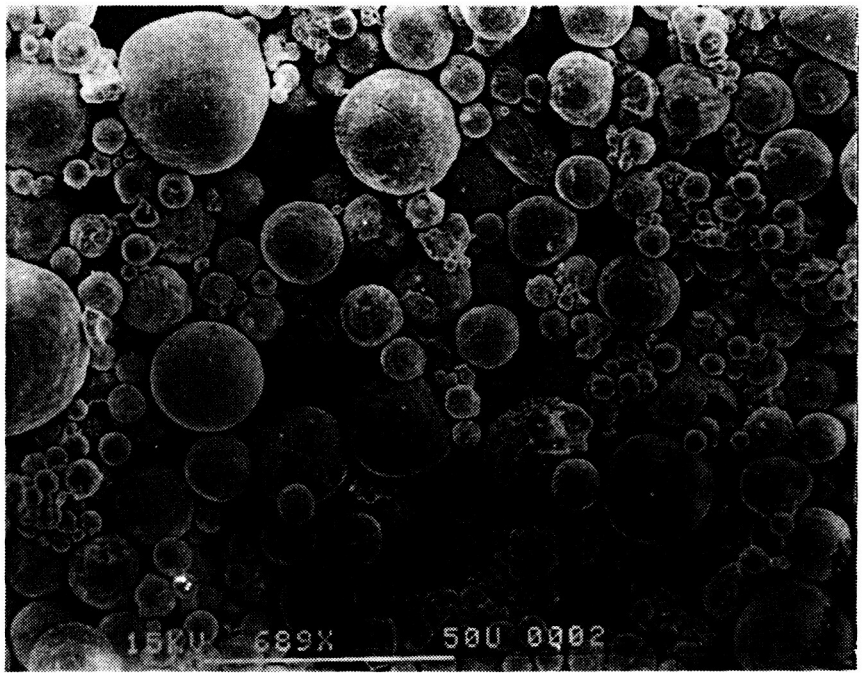

Figure 41. Scanning electron micrograph of plasma-sprayed powder having 10 mol% TiO_2 ($10T_3$).

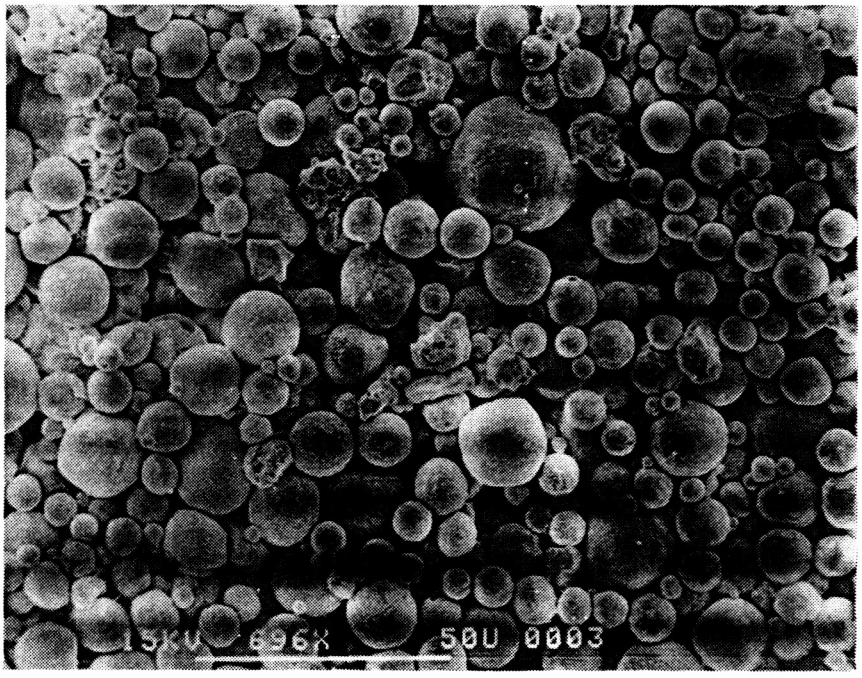

Figure 42. Scanning electron micrograph of plasma-sprayed powder having 15 mol% TiO_2 ($15T_3$).

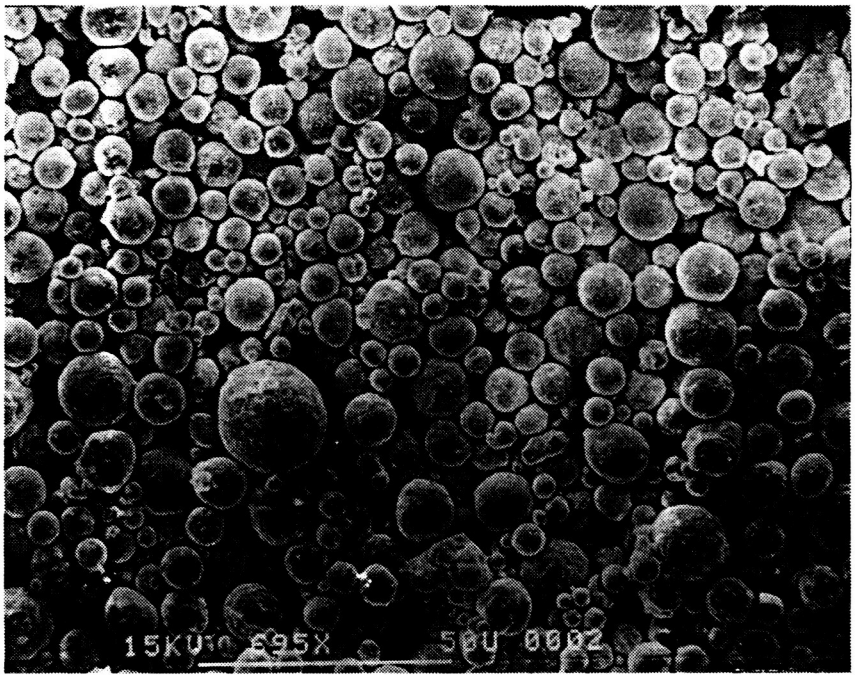

Figure 43. Scanning electron micrograph of plasma-sprayed powder having 20 mol% TiO_2 ($20T_3$).

each composition and fabrication technique. Table 8 summarizes the results. Theoretical mix densities were determined using the rule of mixtures (i.e., for each composition, the densities of HfO_2, ZrO_2, and TiO_2 were added in compositional weight proportions to determine the density of the mixed materials). Theoretical x-ray densities were determined using lattice parameter measurements of fired materials (in the monoclinic form) and assuming that the fluorite unit cell consisted of atoms with compositional proportions.

Isostatically pressed bars in the green state, were found to be approximately 60% of the theoretical density for both the T_1 and T_2 series. Samples that were fired to 1700°C in air achieved only 85% theoretical density. Increasing the firing temperature to 2200°C increased the densities of the reduced materials to roughly 95% and 93% theoretical for the T_1 and T_2 series, respectively. Upon oxidation of these materials at

Table 8. Densities, Mass Changes, and Length Changes of HZT Compositions.

Comp.	Theoretical Mix Density (g/cm^3)	Theoretical X-ray Density (g/cm^3)	Green Density (g/cm^3) (%)	Fired Density (ad) (g/cm^3) (%)	Fired Density (ox) (g/cm^3) (%)	Mass Change (% wt gain)	Length Change (% expan.)
$5T_1$			5.34 64	8.14 97	8.09 97	0.47	0.33
$5T_2$	8.54	8.37	4.98 58	7.86 94	7.75 93	0.45	0.46
$5T_3$				7.97 95	7.99 95	0.28	0.20
$10T_1$			5.26 63	8.06 96	7.99 95	0.61	0.51
$10T_2$	8.55	8.38	4.92 58	7.81 93	7.70 92	0.62	0.57
$10T_3$				8.40 100	8.41 100	0.35	0.31
$15T_1$			5.21 63	7.85 94	7.75 93	0.69	1.40
$15T_2$	8.55	8.33	4.83 56	7.73 93	7.52 93	0.72	1.80
$15T_3$				8.31 100	8.33 100	0.46	0.54
$20T_1$			5.05 60	7.76 92	7.38 87	0.71	2.40
$20T_2$	8.56	8.45	4.76 56	7.57 90	7.42 88	0.74	2.40
$20T_3$				8.37 99	8.45 100	0.55	0.71

1200°C in air, the bars underwent a weight gain and lengthening that increased with the concentration of TiO_2. A slight reduction in the densities of the oxidized materials resulted. Bars that were subsequently oxidized to 1700°C in air suffered a further decrease in density reducing to approximately 92% theoretical. The density reduction that accompanied the oxidation in the T_1 and T_2 series materials resulted in part from phase changes (e.g., the formation of lower density titanates). Phase analyses of the various oxidation states of the T_1 and T_2 series will be discussed shortly.

For the T_3 series, densities of the vacuum hot pressed samples in the reduced state approached theoretical density. Upon oxidation of the samples, the densities became 100% of the theoretical values. In addition, lower linear expansions and weight gains were observed during oxidation of the T_3 compositions as compared with the T_1 and T_2 series. These reduced weight and length changes that accompanied oxidation can be attributed to the absence of the cubic phases in the reduced state and the titanate phases in the oxidized state of the T_3 series. Phase analyses of the T_3 series will be discussed in detail in Section 4.4. (Table 2 shows that the unit cell

volumes of the titanate and cubic phases are lower than the volumes of the monoclinic phases. This volume differential leads to increased volume changes upon oxidation of the materials in the T_1 and T_2 series.) The increased densities in the T_3 series can also be attributed to the absence of the titanate phase in the oxidized materials. (Table 2 shows that the titanate phases have lower densities than the monoclinic phases.)

4.3 Microstructure Analyses

The microstructures of the fired bars were analyzed using both optical and scanning electron microscopy. From optical microscopy, large regions (approximately 16 to 3000 μm) were observed on the polished surfaces of both the reduced and oxidized bars. Scanning electron microscopy showed that these large regions consisted of very fine grains (~1 μm). A summary of the region and grain sizes is given in Table 9.

Scanning electron micrographs of oxidized, polished surfaces of several compositions in the T_1, T_2, and T_3 series are given in Figures 44-52. The micrographs (taken at various magnifications) show the relation between the large regions and the fine grains.

A close examination of the region boundaries in the SEM micrographs suggests that microcracking occurs in the HZT system. As was pointed out in Section 2.2.2.1, microcracking has been observed in the HfO_2-TiO_2 system. A similar situation would be expected in the HZT system. The large (microcrack) regions in the T_1 compositions dramatically increase in size in going across the series, whereas in the T_2 and T_3 series, little change in size is observed. On the other hand, the grain size in the T_1 series decreases, whereas in the T_2 and T_3 series, it remains constant with composition. These observations suggest that the size of the microcracked regions is

Table 9. Microstructure Analyses of Fired HZT Compositions.

Composition	Average Grain Size (μm) (within Regions)	Average Region Size (μm)
$5T_1$	1.3	200
$10T_1$	1.8	160
$15T_1$	0.8	1000
$20T_1$	0.7	3000
$5T_2$	1.0	27
$10T_2$	1.0	34
$15T_2$	1.0	36
$20T_2$	0.9	32
$5T_3$	~1.0	31
$10T_3$	~1.0	20
$15T_3$	~1.0	17
$20T_3$	~1.0	16

inversely proportional to the grain size. Dole et. al.[52] found similar effects in their study of microcracking in HfO_2.

An examination of the grains in the T_1 and T_2 series micrographs shows that a degree of liquid phase sintering is occurring in the higher TiO_2 compositions. The possibility that a liquid phase might be present was observed during firing. Several bars of the high TiO_2 compositions fused together when heated to 2200°C. From the phase diagram of the HfO_2-TiO_2 system (see Figure 7a), a solid plus liquid two-phase region exists at approximately 2200°C for compositions above 15 mol% TiO_2. A similar region apparently exists in the HZT system.

Figures 44-51 show that a high degree of porosity is present in the sintered bodies of the T_1 and T_2 series. The porosity was observed to concentrate at the grain boundaries. Scanning electron micrographs of polished surfaces of $10T_3ox$, $15T_3ox$, and $20T_3ox$ showed the material to be highly dense with very little porosity. Some porosity, however, remained in the $5T_3ox$ composition after hot pressing. Figure 52

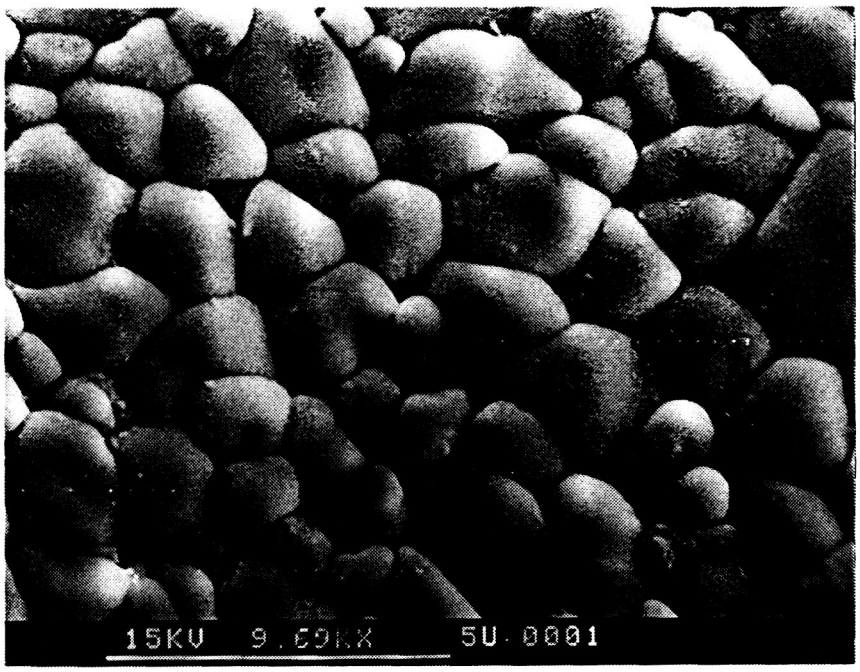

(a)

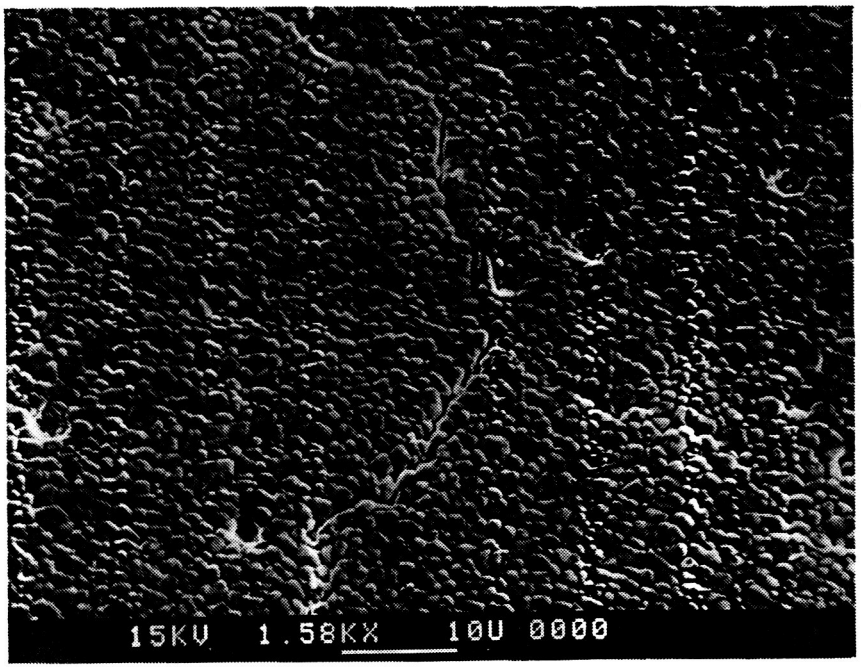

(b)

Figure 44. Scanning electron micrographs of a thermally etched, polished surface of a fired $5T_1$ox bar at (a) high magnification and (b) low magnification.

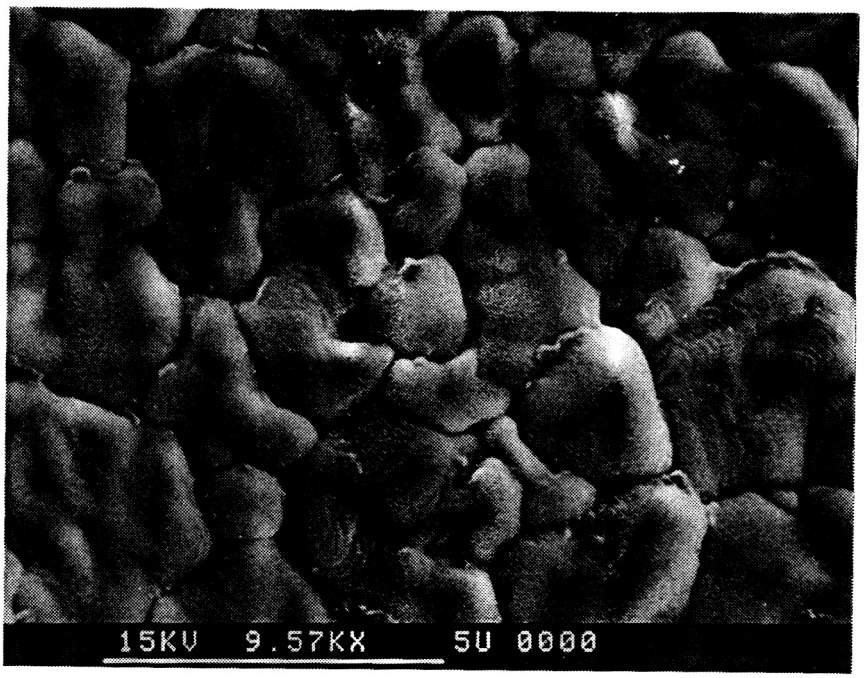

Figure 45. Scanning electron micrograph of a thermally etched, polished surface of a fired $10T_1$ox bar.

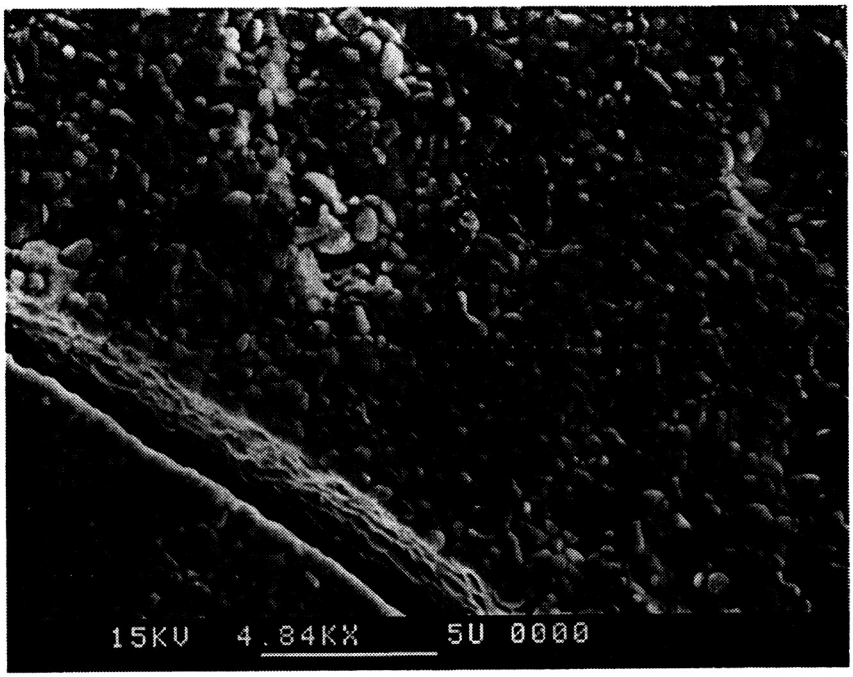

(a)

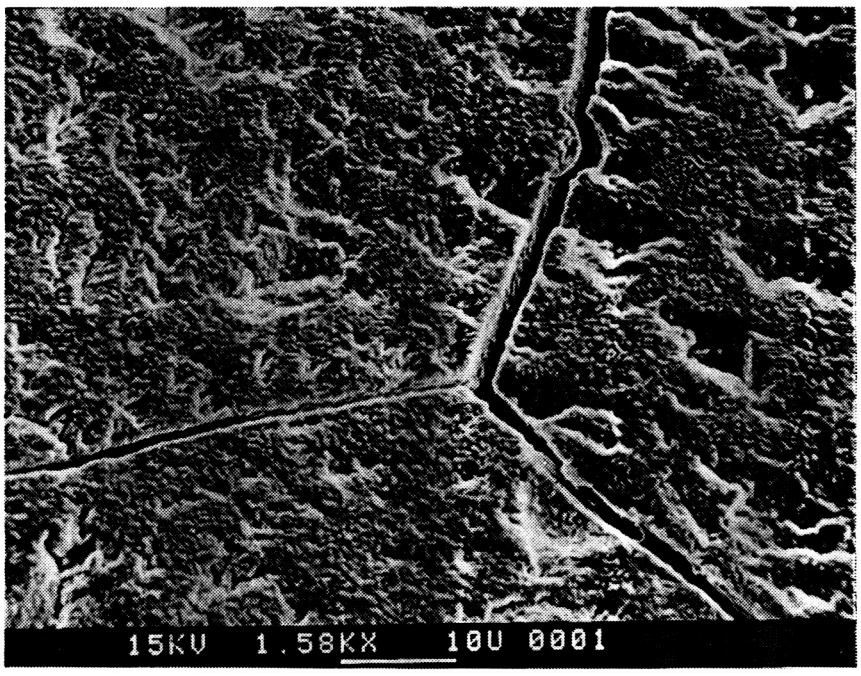

(b)

Figure 46. Scanning electron micrographs of a thermally etched, polished surface of a fired $15T_1ox$ bar at (a) high magnification and (b) low magnification.

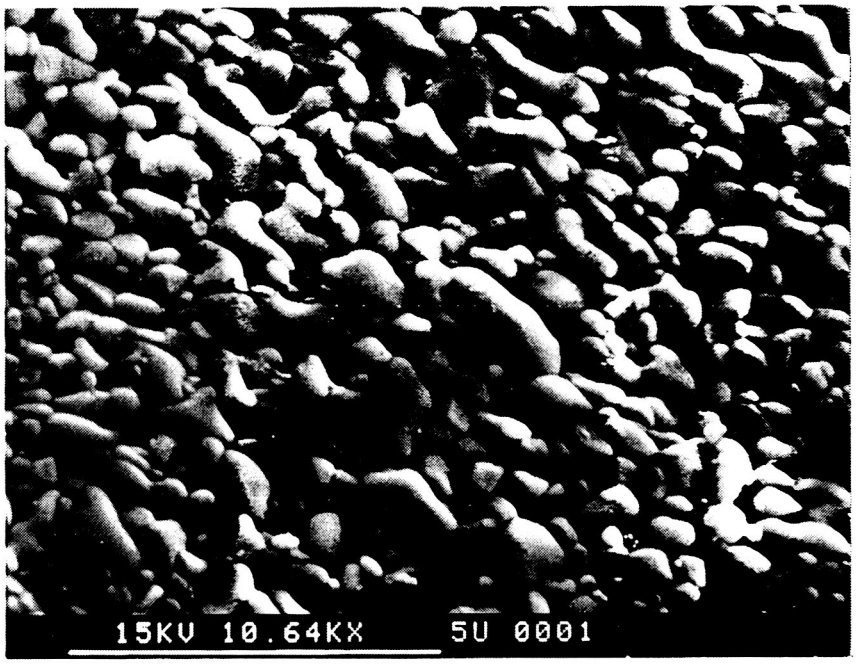

Figure 47. Scanning electron micrograph of a thermally etched, polished surface of a fired $20T_1$ox bar.

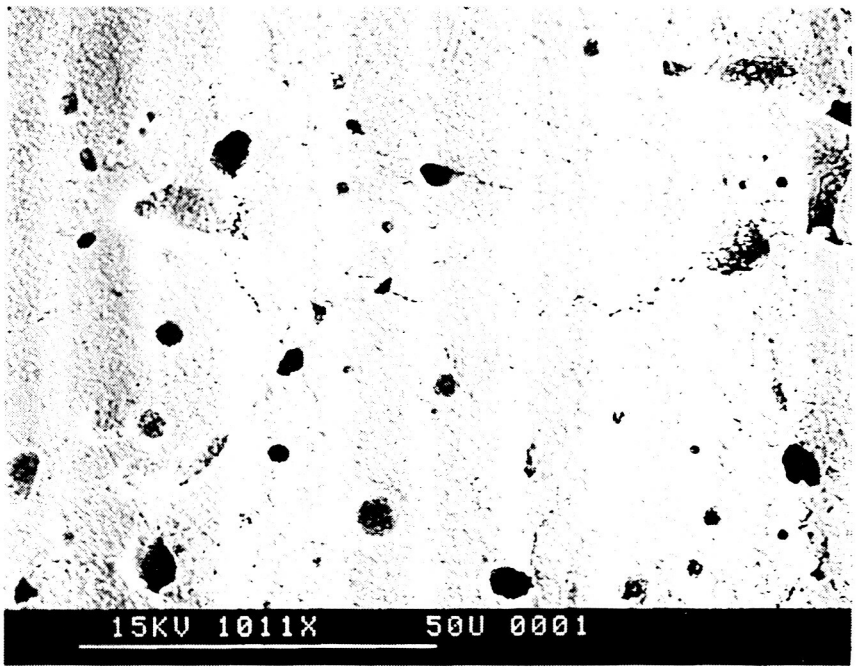

Figure 48. Scanning electron micrograph of a thermally etched, polished surface of a fired $5T_2$ox bar.

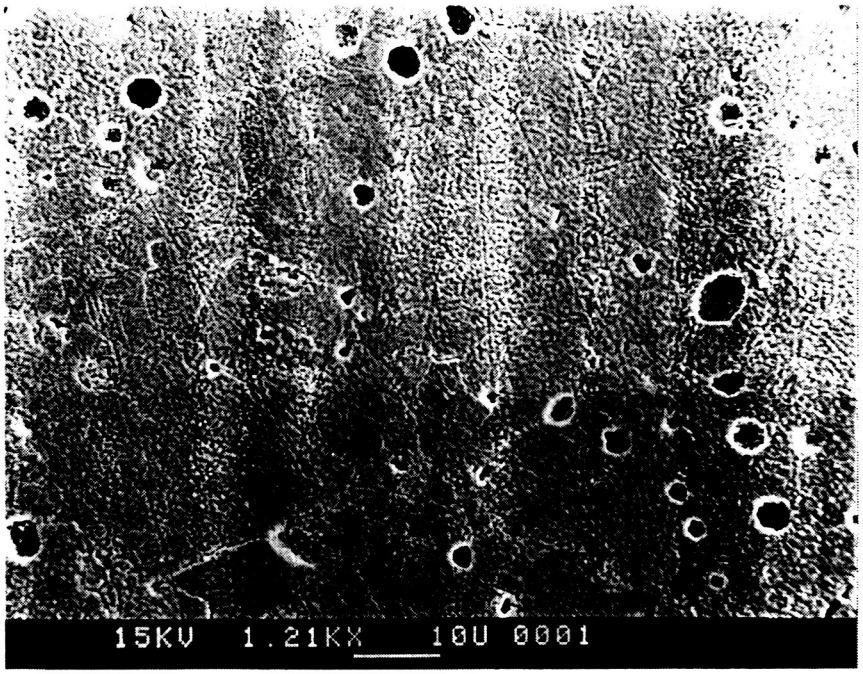

Figure 49. Scanning electron micrograph of a thermally etched, polished surface of a fired $10T_2$ox bar.

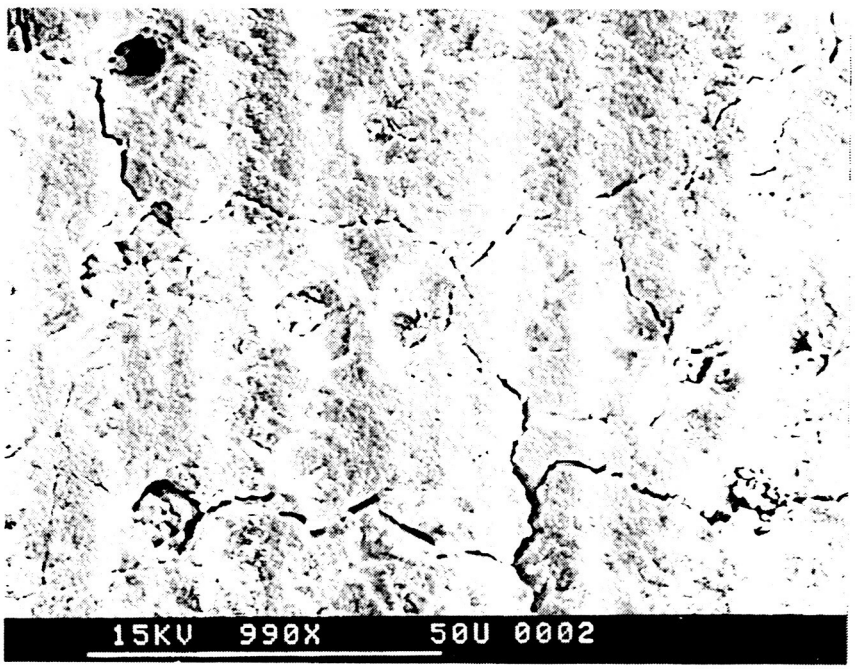

Figure 50. Scanning electron micrograph of a thermally etched, polished surface of a fired $15T_2$ox bar.

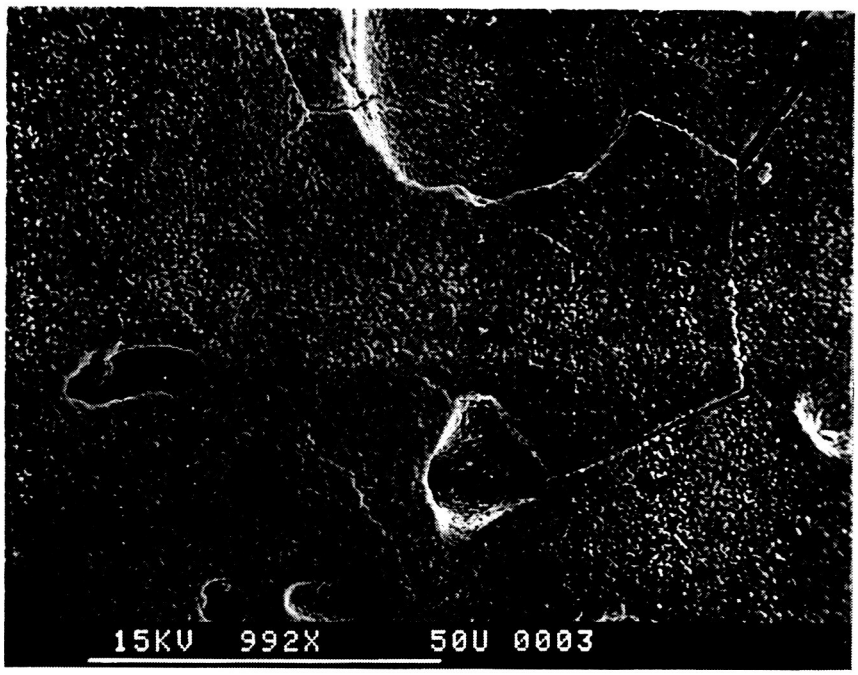

Figure 51. Scanning electron micrograph of a thermally etched, polished surface of a fired 20$\hat{T}_2$ox bar.

(a)

(b)

Figure 52. Scanning electron micrographs of thermally etched, polished surface of fired (a) $5T_3ox$ and (b) $20T_3ox$ bars.

shows that a degree of the original round particle nature that existed prior to pressing was retained.

Qualitative EDX indicated that all compositions: (1) had the correct proportions of Hf, Zr, and Ti, (2) were homogeneous, and (3) had no apparent contamination. Exceptions to statement (2) above were the 20 mol% TiO_2 compositions that had titanates. Second phase titanate grains were found that had higher concentrations of Ti than surrounding grains.

X-ray diffractometry suggested that a degree of preferred orientation was present within the microcrack region in many of the compositions. Diffractometry traces of bars having large microcrack regions tended to have peaks with different relative heights depending upon the orientation of the bar with respect to the x-ray beam. This, coupled with indications of preferential polishing directions, seems to imply that the grains within a microcrack region tend to preferentially align.

4.4 Phase Analyses

Qualitative x-ray analyses were performed on each of the four compositions in the T_1, T_2, and T_3 series. A variety of phases resulted depending on the composition, the fabrication technique, the oxidation state, and the oxidation time and temperature. Table 10 gives a summary of the phase analyses.

4.4.1 Reduced or Highly Anion Deficient State

All compositions prepared in each of the three techniques were black colored after firing in vacuum. This state is referred to as the reduced or highly anion-deficient state. In the reduced state, a variation in the stoichiometric ratio and a weight loss occur due to oxygen release. The black coloration results from entrapped electrons which fill the vacated oxygen sites.[43] A modification of the structure can occur depending on the degree of anion deficiency (or departure from stoichiometric

Table 10. X-ray Phase Analyses of the HZT Compositions.

Comp./Technique	ad	ox (6-12 hrs) (at 1200°C)	ox ($\frac{1}{2}$ hr) (at 1300°C)	ox (at 1700°C)
$5T_1$	M	M	M	
$5T_2$	M	M	M	M
$5T_3$	M	M		
$10T_1$	M + C	M	M	
$10T_2$	M + C	M	M	M
$10T_3$	M	M		
$15T_1$	C + M†	M + O†	M	
$15T_2$	C + M†	M + O†	M	M_1+M_2†+O†
$15T_3$	M + C†	M		
$20T_1$	C + M†	M + O	M	
$20T_2$	C	M + O	M	M_1+M_2+O
$20T_3$	M + C	M		

M is the monoclinic phase, M_1 and M_2 refer to two different monoclinic phases in solution, C is the cubic phase, and O is the orthorhombic titanate phase. A † indicates that only trace amounts were observed.

proportions). For stoichiometric HfO_2 and ZrO_2, the percentages of oxygen are 15.2 and 26.0 wt%, respectively. Two weight percent oxygen loss can be accommodated in HfO_2 at 2200°C while still maintaining a solid solution of HfO_{2-x}.[100] For ZrO_2, up to three weight percent oxygen loss can be accommodated.[101] From the ZrO_2-rich side of the Zr-O phase equilibrium diagram, at 2200°C, tetragonal ZrO_{2-x} is stable up to 0.19 wt% oxygen loss. From 0.19 to 0.48%, cubic and tetragonal ZrO_{2-x} are stable. And from 0.48 to 3.0 wt% loss, cubic ZrO_{2-x} is the stable phase.[101] A similar situation is found in HfO_{2-x}.[100]

In this investigation, the stoichiometric weight percentages of oxygen in the 5, 10, 15, and 20 mol% TiO_2 compositions were 18.5, 18.7, 18.9, and 19.2, respectively. For the T_1 and T_2 compositional series, the weight loss range of the reduced state was

from 0.45 to 0.74%. For the T_3 series, the range was from only 0.28 to 0.55%. The lower weight loss in the T_3 series is probably due to either the lower firing temperature and time (i.e., 2000°C for 2 hours) or to a difference associated with vacuum hot pressing as opposed to sintering in a vacuum furnace.

A comparison of the observed phases cited in Table 10 with the weight losses given in Table 8 suggests that a correlation exists between the degree of oxygen weight loss and the resultant phases. For 0 to 0.47 wt% oxygen loss, only the monoclinic phase was seen. For 0.47 to 0.74%, the monoclinic and cubic phases were observed. Above 0.74%, only the cubic phase existed. These phases correspond to a combination of high and low temperature states and follow similar trends to those which occur in the Zr-O system.

Since fairly rapid cooling rates were employed (20 to 40°C/min.) in all the fabrication techniques, the cubic high temperature phase in the reduced HZT compositions may have been a result of quenching effects. Quenching is known to stabilize the high temperature cubic phase in anion deficient ZrO_2.[101] In the HZT system, the anion deficiency as well as the presence of titanium act to stabilize the cubic phase upon cooling. (At low oxygen partial pressures (as occur in vacuum sintering), titanium ions enter the lattice structure substitutionally for hafnium and zirconium ions. The variability of the titanium ion valence leads to an increased degree of anion deficiency in the reduced compositions which becomes even greater as increasing amounts of titanium ions are added. A more relaxed stable cubic structure is produced as a result of the anion deficiency and the presence of titanium. Upon cooling of these materials, the amount of structural reorientation necessary to change the high temperature effects of titanium are too great, and thus the cubic phase is retained to room temperature.) These occurrences explain the increased amounts of cubic phase that are observed in the reduced materials in the HZT system that have

high TiO_2 concentrations. The high temperature tetragonal phase, on the other hand, reverts to monoclinic symmetry upon cooling and is not stabilized by titanium thus explaining the absence of the tetragonal phase in the reduced state after cooling.

The unit cell lattice parameters of the monoclinic phase in the reduced HZT compositions were approximately: a = 5.009 Å; b = 5.134 Å; c = 5.272 Å; and β = 98.9°. A comparison with the larger parameters of pure monoclinic zirconia and hafnia (refer to Table 2) suggests that either the smaller titanium ions are entering the lattice or that anion deficiency is reducing the size of the unit cell. The lattice parameters of the cubic phases in all of the reduced HZT compositions were ca. 5.055 Å. This value is lower than that of pure cubic ZrO_2 (5.07 Å) suggesting that the cubic unit cell in the HZT compositions is also modified by titanium and/or anion deficiency.

4.4.2 Oxidized State

The oxidized state was obtained after the reduced materials were annealed in air. Depending on the annealing temperature, the bars turned either cream colored (1200°C) or white (1700°C). Also, different phases were observed.

X-ray analyses showed that materials in the T_1 and T_2 series that were oxidized at 1200°C were monoclinic solid solutions for compositions with less than 15 mol% TiO_2. For compositions with more than 15 mol% TiO_2, a titanate phase was observed in addition to the monoclinic phase. As Table 10 shows, high TiO_2 compositions in the T_2 series that were annealed at 1700°C contained an additional monoclinic phase, whereas identical compositions annealed at 1200°C did not. (A similar situation occurs in the HfO_2-TiO_2 system.[18]) Table 11 gives the d-spacings which distinguish the two monoclinic phases and the orthorhombic titanate phase in the $15T_2$ox and $20T_2$ox materials. The significance of the second monoclinic phase was discussed in Section 2.1.2.2.

Table 11. X-ray d-spacings from Powder Patterns of T_2ox Samples Oxidized at 1700°C.

Composition (in mol% TiO_2)	$d_{-111_{M_2}}$(Å)	$d_{-111_{M_1}}$(Å)	d_{110_O}(Å)	$d_{111_{M_1+M_2}}$(Å)
15	3.123	3.080	2.952	2.808
20	3.127	3.081	2.963	2.810

For all compositions in the T_3 series, only the monoclinic phase was observed after oxidation. Even the 20 mol% TiO_2 composition showed no presence of the titanate phase. This is in agreement with the work of Brown et. al.[4] and Schroeder.[3] Powders in the T_1 and T_2 series that were taken to 1300°C for $\frac{1}{2}$ hour on a hot stage x-ray diffractometer and cooled were also observed to be only monoclinic. Both the T_3 series oxidation effects and the T_1 and T_2 oxidation effects at 1300°C suggest that the suppression of the titanate phase is an oxidation related phenomenon.

X-ray powder diffraction patterns were taken of each composition in the monoclinic phase. The results are given in Table 12. A decrease in parameters with increasing TiO_2 was observed. This confirms that the titanium is entering the unit cell; however, whether or not the titanium takes an interstitial or substitutional position is not apparent.

Table 12. X-ray Lattice Parameters of Monoclinic HZT Compositions.

Composition (in mol% TiO_2)	a (Å)	b (Å)	c (Å)	β (degrees)	V ($Å^3$)
5	5.109	5.158	5.288	99.2	137.6
10	5.087	5.127	5.273	99.0	135.8
15*	5.071	5.104	5.258	98.8	134.6
20*	5.030	5.050	5.240	98.6	131.3

*Not stable form (i.e., 100% monoclinic phase with no titanate).

4.5 Electrical Conductivity

Electrical resistance measurements were made on bars in the T_2 compositional series at temperatures over the range 400°C to 1700°C in air and in gas mixtures of 1% oxygen in argon and 9.55% CO in CO_2. Measurements were made to determine the effects of titania on the conductivity of compositions in the HZT system as a function of temperature and oxygen partial pressure. The T_2 series was chosen for examination since testable materials were produced for each composition within the series. Similar electrical behavior, however, would be expected for identical compositions in the T_1 and T_3 series as well.

The electrical conductivity as a function of temperature is shown in Figure 53 for the four compositions. Figure 54 shows the same data plotted so that the pressure dependence for each composition can be seen more clearly. Several observations can be made from the electrical conductivity data: (1) At high temperatures and low P_{O_2}, the conductivity increases with increasing TiO_2 concentration. (2) At low temperatures and high P_{O_2}, the conductivity decreases with increasing TiO_2, while at low P_{O_2}, it increases. The observed conductivity trends coupled with the phase analyses suggest that titanium is incorporated (1) interstitially at low temperatures and high P_{O_2} and (2) substitutionally with a valency change at low P_{O_2}.

The probable defects in the HZT system are summarized in Table 13. The defect formation reactions can be written as:

$$O_o \overset{K_1}{\rightleftharpoons} O_i'' + V_o^{\circ\circ} \qquad (53)$$

$$O_o \overset{K_2}{\rightleftharpoons} \tfrac{1}{2}O_2 + V_o^{\circ\circ} + 2e' \qquad (54)$$

$$e_V \overset{K_3}{\rightleftharpoons} e' + h^{\circ} \qquad (55)$$

$$S \overset{K_4}{\rightleftharpoons} V_M'''' + 2V_o^{\circ\circ} \qquad (56)$$

$$F_M \overset{K_5}{\rightleftharpoons} F_i^{\circ\circ\circ\circ} + V_M'''' \qquad (57)$$

$$F_M \overset{K_6}{\rightleftharpoons} F_M' + h^{\circ} \qquad (58)$$

$$F_M' \overset{K_7}{\rightleftharpoons} F_M'' + h^{\circ} \qquad (59)$$

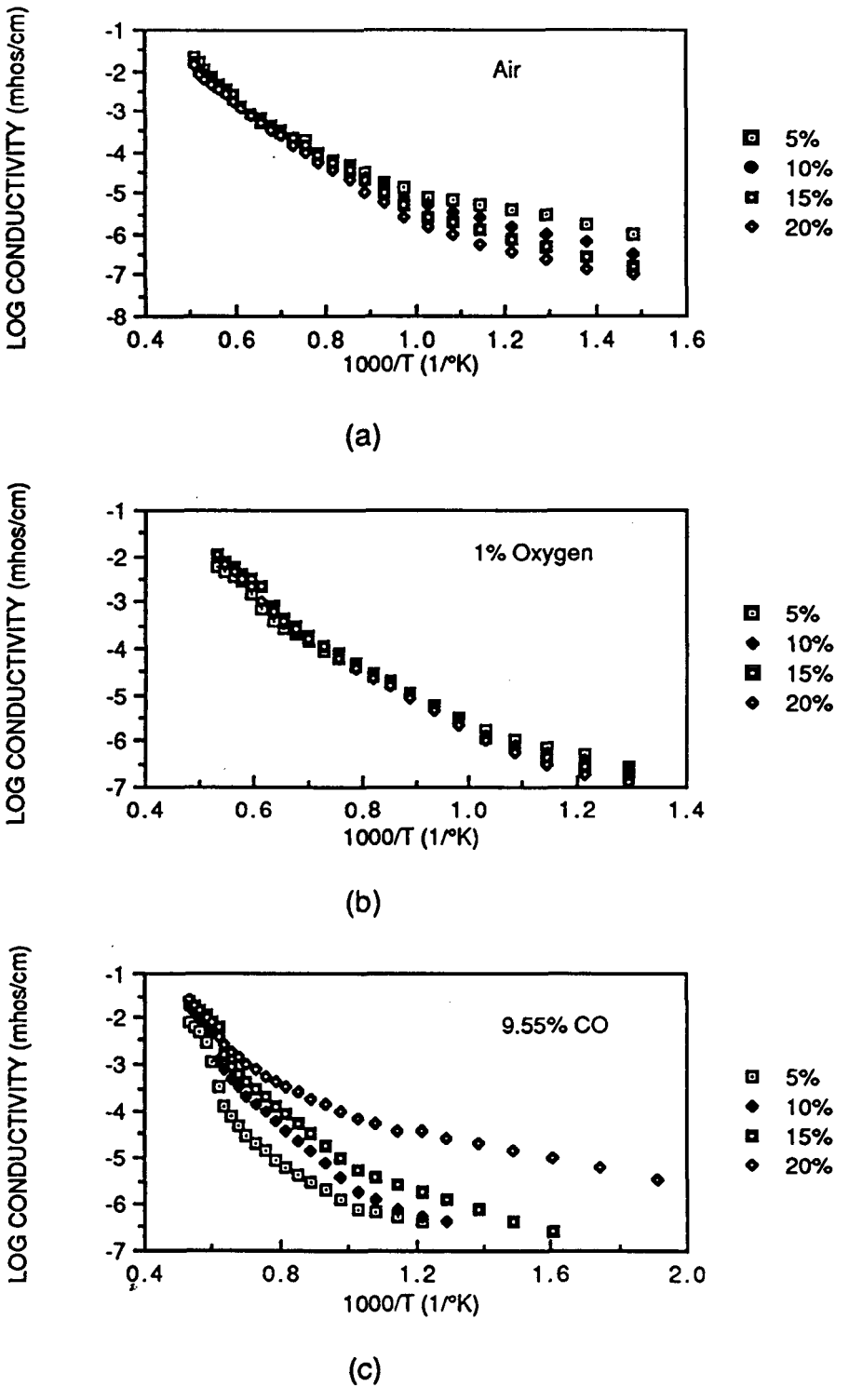

Figure 53. The electrical conductivity of four compositions in the HZT system measured as a function of temperature in (a) air, (b) 1% O_2 in Ar, and (c) 9.55% CO in CO_2. The amount of TiO_2 in mol% is indicated on the right.

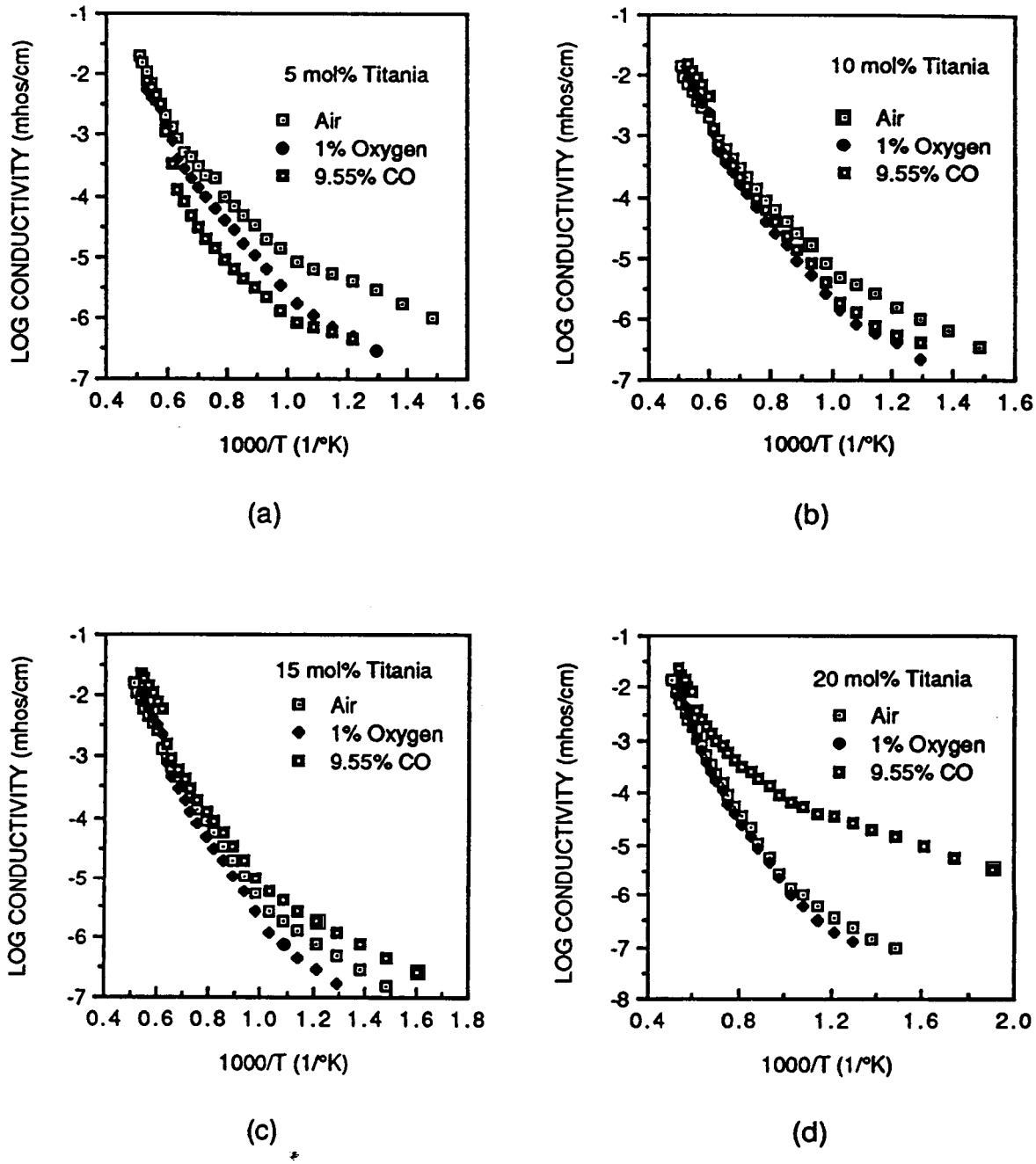

Figure 54. The electrical conductivity measured as a function of temperature in air, 1% O_2 in Ar, and 9.55% CO in CO_2 for compositions in the HZT system having (a) 5, (b) 10, (c) 15, and (d) 20 mol% TiO_2.

Table 13. Probable Defects in the HZT System.

Defect	Description
O_o	Oxygen in Oxygen Site
O_i''	Interstitially Incorporated Oxygen Ion
$V_o^{\bullet\bullet}$	Doubly-Ionized Oxygen Vacancy
V_M''''	Tetravalent Cation Vacancy
F_M	Substitutionally Incorporated Ti^{4+} Cation on a Tetravalent Cation Site
F_M'	Substitutionally Incorporated Ti^{3+} Cation on a Tetravalent Cation Site
F_M''	Substitutionally Incorporated Ti^{2+} Cation on a Tetravalent Cation Site
$F_I^{\bullet\bullet\bullet\bullet}$	Interstitially Incorporated Ti^{4+} Cation
S	Schottky Pair
e_V	Electron in Valence Band
e'	Electron in Conduction Band
$h^{\bullet}$	Hole in Valence Band

where the reactions in Equations (56)-(59) represent the effect of interstitially and substitutionally incorporating titanium into the fluorite structure. The reactions in Equations (53)-(55) are equivalent to those given in Equations (2)-(4) for pure fluorite materials. A more direct relation between hole and electron formation, however, is given by Equation (55).

The mass action law for each becomes, respectively:

$$K_1 = [O_i''] [V_o^{\bullet\bullet}] \tag{60}$$

$$K_2 = n^2 P_{O_2}^{\frac{1}{2}} [V_o^{\bullet\bullet}] \tag{61}$$

$$K_3 = np \tag{62}$$

$$K_4 = [V_M''''] [V_o^{\bullet\bullet}]^2 \tag{63}$$

$$K_5 = \frac{[F_I^{\bullet\bullet\bullet\bullet}] [V_M'''']}{[F_M]} \tag{64}$$

$$K_6 = \frac{[F_M'] p}{[F_M]} \tag{65}$$

$$K_7 = \frac{[F_M''] p}{[F_M']} \tag{66}$$

where [ ] indicates defect concentrations, and n and p are the electron and hole concentrations, respectively.

Conservation of titanium requires that the sum of the concentrations of interstitially and substitutionally incorporated titanium is equal to the total amount of titanium added. Also, electroneutrality requires that the concentration of all positive charge carriers equal that of all negative charge carriers. These two conditions are then:

$$[Ti] = [F_M] + [F_M'] + [F_M''] + [F_i^{\bullet\bullet\bullet\bullet}] \tag{67}$$

$$n + 4[V_M''''] + [F_M'] + 2[F_M''] + 2[O_i''] = p + 4[F_i^{\bullet\bullet\bullet\bullet}] + 2[V_o^{\bullet\bullet}] \tag{68}$$

The defect concentrations as a function of P_{O_2} can then be determined for the following six regions.

In Region I (very low P_{O_2}), the dominating electroneutrality condition is $n = 2[V_o^{\bullet\bullet}]$, and the prevailing titanium conservation condition is $[F_M''] \approx [Ti]$, giving:

$$n = (2K_2)^{\frac{1}{3}} P_{O_2}^{-\frac{1}{6}} \tag{69}$$

$$p = \left(\frac{K_3^3}{2K_2}\right)^{\frac{1}{3}} P_{O_2}^{\frac{1}{6}} \tag{70}$$

$$[V_o^{\bullet\bullet}] = \left(\frac{K_2}{4}\right)^{\frac{1}{3}} P_{O_2}^{-\frac{1}{6}} \tag{71}$$

$$[O_i''] = \left(\frac{4K_1}{K_2}\right)^{\frac{1}{3}} P_{O_2}^{\frac{1}{6}} \tag{72}$$

$$[V_M''''] = \left(\frac{4K_4^{\frac{3}{2}}}{K_2}\right)^{\frac{2}{3}} P_{O_2}^{\frac{1}{3}} \tag{73}$$

$$[F_M] = [Ti] / \left(1 + \frac{K_6}{p} + \frac{K_6K_7}{p^2} + \frac{K_5}{[V_M'''']}\right) \tag{74}$$

$$[F_M'] = \frac{K_6 [F_M]}{p} \tag{75}$$

$$[F_M''] = \frac{K_6K_7 [F_M]}{p^2} \tag{76}$$

and

$$[F_i^{\bullet\bullet\bullet\bullet}] = \frac{K_5 [F_M]}{[V_M'''']} \tag{77}$$

In Region II (low P_{O_2}), the electroneutrality condition is $[V_o^{\bullet\bullet}] = [F_M'']$ and the titanium conservation condition is $[F_M''] \approx [Ti]$, giving:

$$n = \left(\frac{K_2}{[Ti]}\right)^{\frac{1}{2}} P_{O_2}^{-\frac{1}{4}} \tag{78}$$

$$p = \left(\frac{[Ti]K_3^2}{K_2}\right)^{\frac{1}{2}} P_{O_2}^{\frac{1}{4}} \tag{79}$$

$$[V_o^{\bullet\bullet}] = [Ti] \tag{80}$$

$$[O_i''] = \frac{K_1}{[Ti]} \tag{81}$$

$$[V_M''''] = \frac{K_4}{[Ti]^2} \tag{82}$$

and the equations for $[F_M]$, $[F_M']$, $[F_M'']$, and $[F_i^{\bullet\bullet\bullet\bullet}]$ are the same as those in Region I.

In Region III (medium P_{O_2}), the electroneutrality condition is $[F_M''] = 2[F_i^{\bullet\bullet\bullet\bullet}]$, and the titanium conservation condition requires that $[F_M''] \approx \frac{2}{3}[Ti]$ and $[F_i^{\bullet\bullet\bullet\bullet}] \approx \frac{1}{3}[Ti]$, giving:

$$n = \left(\frac{2K_2^2K_3^2K_5}{K_4K_6K_7}\right)^{\frac{1}{6}} P_{O_2}^{-\frac{1}{6}} \tag{83}$$

$$p = \left(\frac{K_3^4K_4K_6K_7}{2K_2^2K_5}\right)^{\frac{1}{6}} P_{O_2}^{\frac{1}{6}} \tag{84}$$

$$[V_o^{\bullet\bullet}] = \left(\frac{K_2K_4K_6K_7}{2K_3^2K_5}\right)^{\frac{1}{3}} P_{O_2}^{-\frac{1}{6}} \tag{85}$$

$$[O_i''] = \left(\frac{2K_1^3K_3^2K_5}{K_2K_4K_6K_7}\right)^{\frac{1}{3}} P_{O_2}^{\frac{1}{6}} \tag{86}$$

$$[V_M''''] = \left(\frac{2K_3^4K_4K_5^2}{K_2^2K_6^2K_7^2}\right)^{\frac{1}{3}} P_{O_2}^{\frac{1}{3}} \tag{87}$$

and the equations for $[F_M]$, $[F_M']$, $[F_M'']$, and $[F_i^{\bullet\bullet\bullet\bullet}]$ are the same as those in Regions I and II.

In Region IV (medium high P_{O_2}), the electroneutrality condition is $[F_M'] = 4[F_i^{\bullet\bullet\bullet\bullet}]$, and the titanium conservation condition is $[F_M] \approx [Ti]$, giving:

$$n = \left(\frac{K_2^2 K_3 K_5}{K_4 K_6}\right)^{\frac{1}{5}} P_{O_2}^{-\frac{1}{5}} \tag{88}$$

$$p = \left(\frac{K_3^4 K_4 K_6}{K_2^2 K_5}\right)^{\frac{1}{5}} P_{O_2}^{\frac{1}{5}} \tag{89}$$

$$[V_o^{\bullet\bullet}] = \left(\frac{K_2^5 K_4 K_6}{K_3^5 K_5}\right)^{1/10} P_{O_2}^{-1/10} \tag{90}$$

$$[O_i''] = \left(\frac{K_1^{10} K_3^5 K_5}{K_2^5 K_4 K_6}\right)^{1/10} P_{O_2}^{1/10} \tag{91}$$

$$[V_M''''] = \left(\frac{K_3^5 K_4^4 K_5}{K_2^5 K_6}\right)^{\frac{1}{5}} P_{O_2}^{\frac{1}{5}} \tag{92}$$

and the equations for $[F_M]$, $[F_M']$, $[F_M'']$, and $[F_i^{\bullet\bullet\bullet\bullet}]$ are the same as those in Regions I, II and III.

In Region V (high P_{O_2}), the electroneutrality condition is $p = [F_M']$ and the titanium conservation condition is $[F_M] \approx [Ti]$, giving:

$$n = \left(\frac{K_3^2}{[Ti]\,K_6}\right)^{\frac{1}{2}} \tag{93}$$

$$p = \left([Ti]K_6\right)^{\frac{1}{2}} \tag{94}$$

$$[V_o^{\bullet\bullet}] = \left(\frac{[Ti]K_2K_6}{K_3^2}\right) P_{O_2}^{-\frac{1}{2}} \tag{95}$$

$$[O_i''] = \left(\frac{K_1K_3^2}{[Ti]K_2K_6}\right) P_{O_2}^{\frac{1}{2}} \tag{96}$$

$$[V_M''''] = \left(\frac{K_3^4K_4}{[Ti]^2K_2^2K_6^2}\right) P_{O_2} \tag{97}$$

and the equations for $[F_M]$, $[F_M']$, $[F_M'']$, and $[F_i^{\bullet\bullet\bullet\bullet}]$ are the same as those in Regions I,II, III, and IV.

In Region VI (very high P_{O_2}), the electroneutrality condition is $p = 4[V_M'''']$, and the titanium conservation condition is $[F_M] \approx [Ti]$, giving:

$$n = \left(\frac{K_2^2 K_3}{4K_4}\right)^{\frac{1}{5}} P_{O_2}^{-\frac{1}{5}} \quad (98)$$

$$p = \left(\frac{4K_3^4 K_4}{K_2^2}\right)^{\frac{1}{5}} P_{O_2}^{\frac{1}{5}} \quad (99)$$

$$[V_O^{\bullet\bullet}] = \left(\frac{16K_2K_4^2K_6}{K_3^2}\right)^{\frac{1}{5}} P_{O_2}^{-1/10} \quad (100)$$

$$[O_i''] = \left(\frac{K_1^5 K_3^2}{16K_2K_4^2}\right)^{\frac{1}{5}} P_{O_2}^{1/10} \quad (101)$$

$$[V_M''''] = \left(\frac{K_3^2 K_4}{4^4 K_2^2}\right)^{\frac{1}{5}} P_{O_2}^{\frac{1}{5}} \quad (102)$$

and the equations for $[F_M]$, $[F_M']$, $[F_M'']$, and $[F_i^{\bullet\bullet\bullet\bullet}]$ are the same as those in Regions I, II III, IV and V.

The proposed Kröger-Vink diagram which shows the defect concentration dependence on the oxygen partial pressure is shown in Figure 55. The titanium concentration was chosen arbitrarily to be 10 mol%. Equilibrium constants (K) were chosen to give reasonable defect concentrations over the specified pressure regions. The diagram given in Figure 55 is one of a number of possibilities based on assumptions of equilibrium constants and titanium concentrations. In addition, the pressure ranges given in the diagram are only relative to actual pressure regions.

The electrical conductivity measurements from this work were plotted as a function of P_{O_2} at various temperatures (Figure 56). (The P_{O_2} of 9.55% CO in CO_2 has the temperature dependence shown in Figure 57.) A negative P_{O_2} dependence is observed at high temperatures under low pressures for HZT compositions with high TiO_2 concentrations. This negative slope is indicative of n-type conductivity. A positive slope is observed at low temperatures under high pressures for all compositions, and at high temperatures for the 5 mol% TiO_2 composition. This positive slope is indicative of p-type conductivity. A general tendency to go from n-type to p-type conductivity

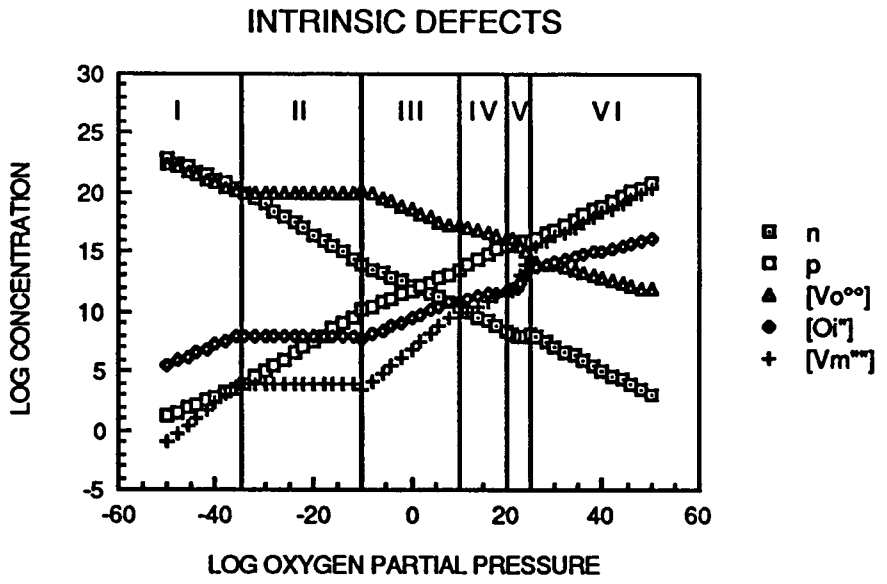

(a)

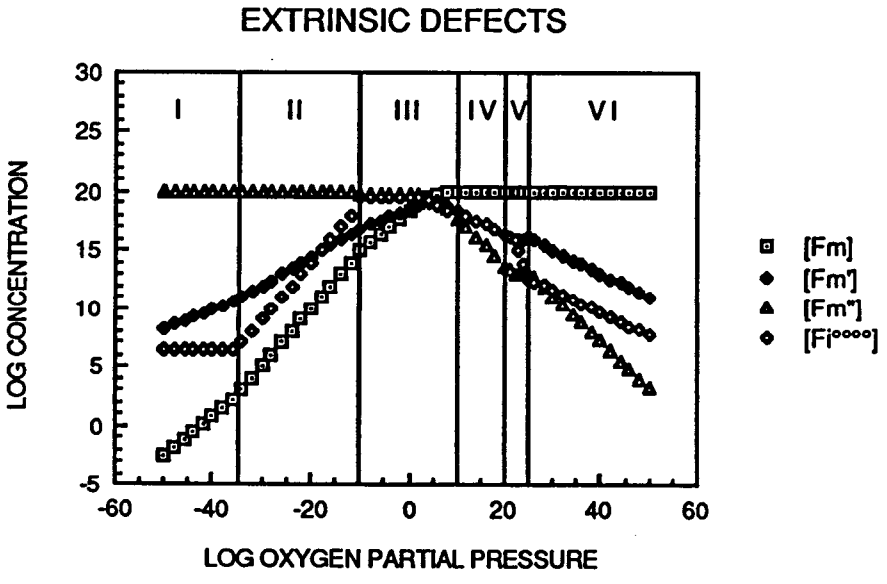

(b)

Figure 55. Kröger-Vink diagram showing defect concentration dependence on P_{O_2} for TiO_2 doped MO_2 for (a) intrinsic and (b) extrinsic defects.

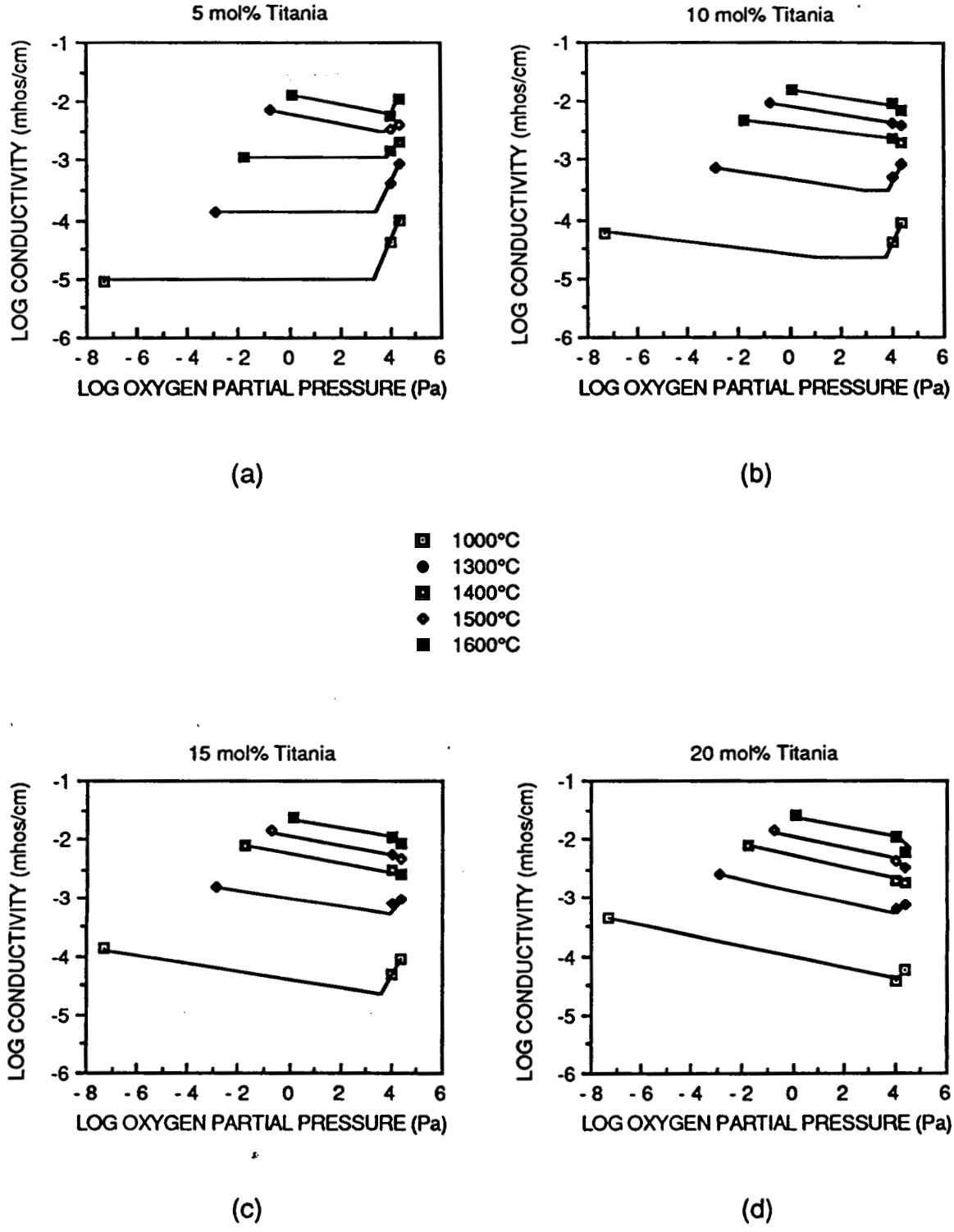

Figure 56. Electrical conductivity dependence on P_{O_2} for compositions in the HZT system: (a) 5 mol% TiO_2, (b) 10 mol% TiO_2, (c) 15 mol% TiO_2, and (d) 20 mol% TiO_2.

C-2

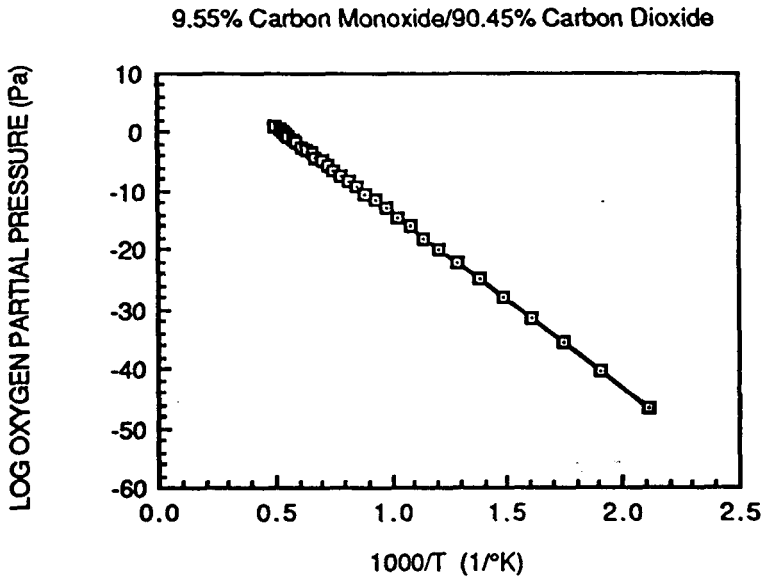

Figure 57. The temperature dependence of the oxygen partial pressure of 9.55% CO in CO_2.

occurs as oxygen partial pressure is increased. This tendency is suppressed as TiO_2 is added. That is, at high pressures, titanium is incorporated interstitially reducing p-type conductivity with increasing TiO_2 concentration. At low pressures, titanium is incorporated substitutionally with a valency change increasing n-type conductivity with increasing TiO_2 concentration. The trends observed in the data support the proposed defect model for the HZT system.

Since defect mobilities were not considered in the present model and since equilibrium constants were chosen rather than determined, detailed correlations between the conductivities predicted by the model and experimental values cannot be conclusively made. Furthermore, accurate determinations of the slopes in Figure 56 are not possible due to the limited nature of the data. Conductivity measurements at several additional partial pressures need to be made in order to properly determine the slopes and assess the model. The primary purpose of plotting the data in Figure 56 was to show the general pressure dependence on conductivity that occurs in the HZT system and to correlate the dependence to a possible defect model.

A comparison with the literature shows that unlike the ZrO_2-based electrolytes that are doped with CaO or MgO, the HZT compositions have a rather high electronic conductivity component. Worrell and Weppner[44] found a similar effect in TiO_2 doped Y_2O_3-stabilized ZrO_2. They also concluded that the high electronic conductivity was due to titanium entering into interstitial positions. They were unable, however, to determine whether the titanium valency changed leading to increased conductivity via electron hopping or if the oxygen vacancies were causing the increase in conductivity.

4.6 Thermal Expansion

Thermal expansion measurements were made on T_2ox bars from room temperature to 1700°C in air. Measurements were made to determine the effects of titania on the thermal expansion behavior in the HZT system. The T_2ox series was chosen for examination since all the compositions in the series produced testable bars. Extensive microcracking occurred in the T_1ox series making them impossible to thermally cycle to 1700°C repeatedly without breaking. As will be explained shortly, low thermal expansion coefficients ($< 4 \times 10^{-6}/°C$) would be expected for these materials since microcracking was so prevalent. Compositions in the T_3ox series were also unable to survive repeated cycling to 1700°C and hence were not tested. Again, low thermal expansion coefficients would be expected based on literature findings for monoclinic materials in the HZT system.[2-4] Since the testing apparatus was not set up for thermal expansion measurements in reducing environments, thermal expansion measurements of reduced HZT compositions were not made. A study of the thermal expansion behavior of these materials would certainly be enlightening and is recommended for future studies of the HZT system.

4.6.1 Thermal Expansion Coefficient

The fractional thermal expansions ($\Delta L/L$) versus temperature are shown in

Figures 58-61 for the four T_2ox compositions. The thermal expansion coefficient of each composition is given in Table 14 for both the monoclinic and tetragonal phases. A general decrease in the coefficient occurs with increasing TiO_2 concentration. For the monoclinic phase, a range from 6.2 to 5.0 x 10^{-6}/°C was observed for the compositional range 5 to 20 mol% TiO_2. As pointed out in Table 4, the calculated linear thermal expansion coefficients determined from lattice parameter data for pure HfO_2 and ZrO_2 in the monoclinic phase are 6.9 and 7.6 x 10^{-6}/°C, respectively. The measured coefficients for compositions of HfO_2-ZrO_2 solid solutions having about the same proportions as in this investigation are ca. 7.2 x 10^{-6}/°C.[21] The measured thermal expansion coefficient values in this study fall below each of these values implying that TiO_2 is indeed reducing the thermal expansion.

From studies of the ZrO_2-TiO_2 and HfO_2-TiO_2 systems, the thermal expansion coefficient was also found to reduce with increasing TiO_2. For 20 mol% TiO_2 added to ZrO_2, the reduction was 11%.[19] For 25 mol% TiO_2 added to HfO_2, the thermal expansion coefficient was reduced by 60%.[56] In this study, the reduction was double the amount found in the ZrO_2-TiO_2 system. As pointed out in Section 2.2.2.1, the titanate that forms in the HfO_2-TiO_2 system is the cause of the extreme reduction in the thermal expansion coefficient. The titanate that forms in the ZrO_2-TiO_2 system does not reduce the thermal expansion coefficient by nearly as much. This suggests that the titanates that form in the HZT system have an intermediate effect on the the reduction in thermal expansion as compared with $HfTiO_4$ and $ZrTiO_4$. But indeed, the titanate does lower the thermal expansion coefficient as is seen by the large drop in Table 14 in going from the 15 to 20 mol% compositions.

A discrepancy exists between the measured coefficient of the 20 mol% TiO_2 composition obtained in the present study (5.0 x 10^{-6}/°C) and that found for an identical composition studied by Brown et. al. (3.1 x 10^{-6}/°C).[4] These anomalous results can be explained by a number of factors (e.g., fabrication and phase

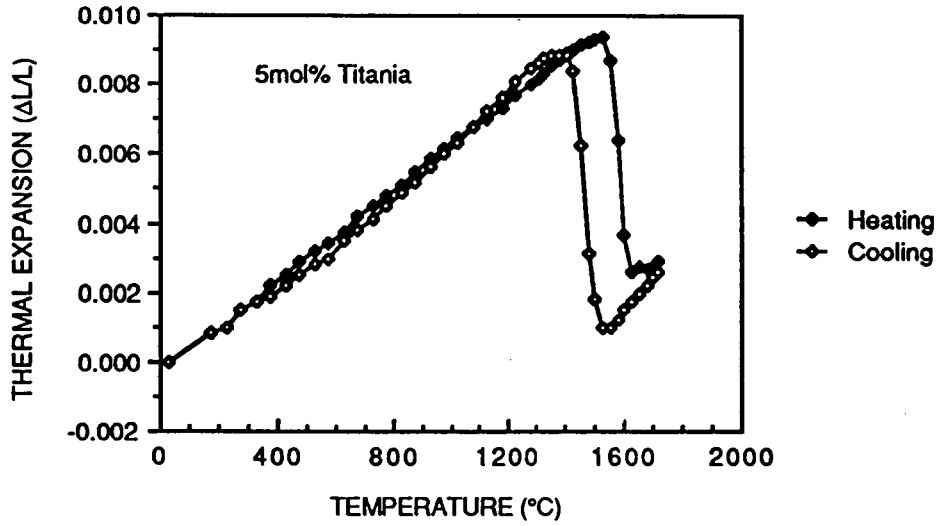

Figure 58. Linear thermal expansion of the 5 mol% TiO_2 composition in the HZT system.

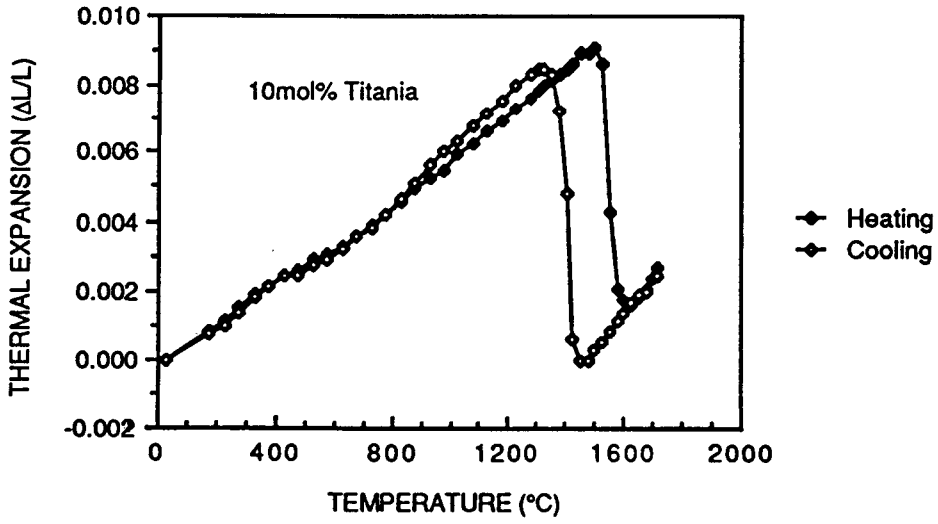

Figure 59. Linear thermal expansion of the 10 mol% TiO_2 composition in the HZT system.

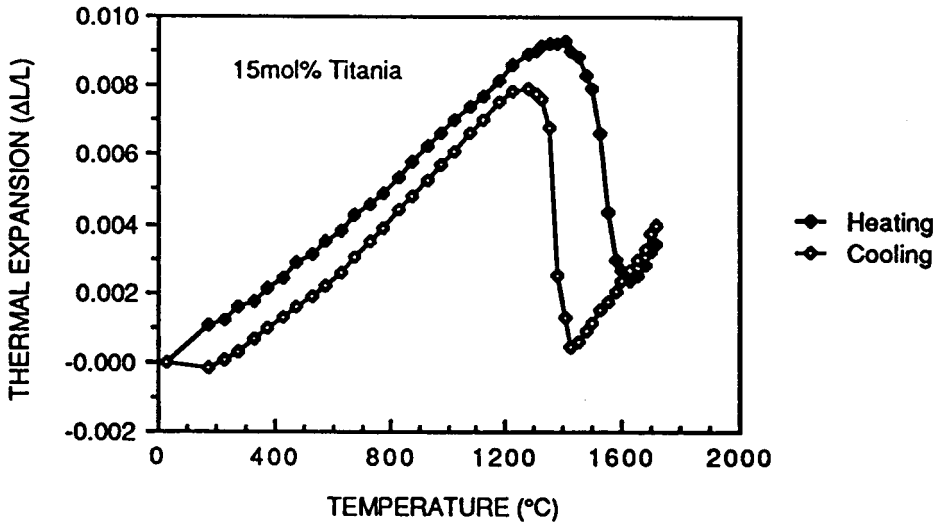

Figure 60. Linear thermal expansion of the 15 mol% TiO_2 composition in the HZT system.

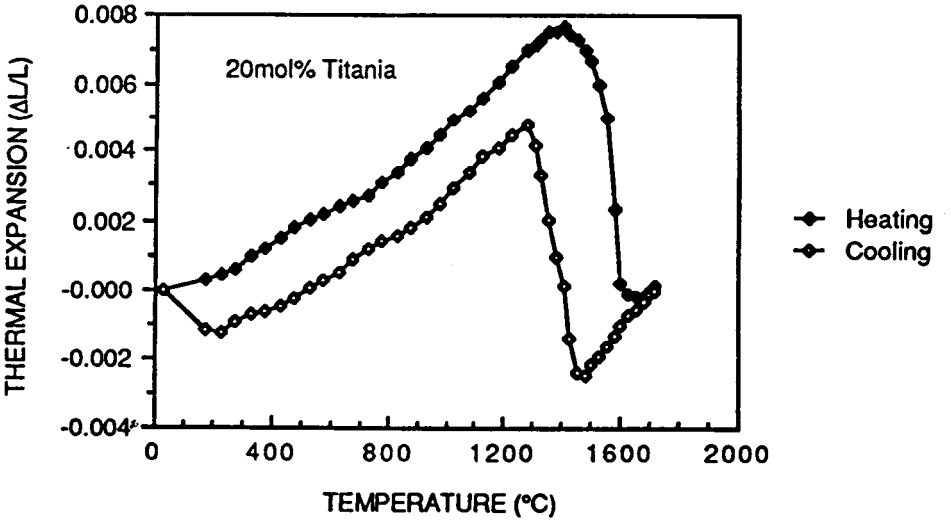

Figure 61. Linear thermal expansion of the 20 mol% TiO_2 composition in the HZT system.

Table 14. Thermal Expansion Coefficients of the Monoclinic and Tetragonal Phases in the HZT Compositions.

Composition (mol% TiO_2)	Thermal Expansion Coefficient (10^{-6}/°C) Monoclinic Phase	Tetragonal Phase
5	6.22	8.31
10	6.12	8.29
15	6.05	8.26
20	5.03	7.96

differences, temperature range differences, and measurement rate differences).

Schroeder, in his work with the HZT system, found that the fabrication process had a critical effect on the reproducibility of measurements and that the reproducibility was rather poor.[2,3] As this study has already pointed out, phase differences can be expected for the same composition depending on the fabrication and oxidation process. In the work of Brown et. al.,[4] the 20 mol% composition was fabricated by hot-pressing disks from reaction-sintered powders and then sintering the disks at 2000°C for 1 hour. In the present study, the fabrication involved sintering cold pressed bars to 2200°C in vacuum for 4 hours and then reoxidizing to 1700°C. In the former case, only the monoclinic phase was observed. In the latter case, two monoclinic phases and a titanate phase resulted. One factor that may explain the discrepancies in the thermal expansion coefficient values, therefore, is that different phases due to the fabrication processes were being examined even though the compositions were the same.

A second factor is the range over which the measurements were made. In the Brown et. al. study, the thermal expansion coefficient was measured from room temperature to only 1000°C. The thermal expansion coefficient for the same range in the present study is approximately 3.9×10^{-6}/°C.

A third factor might be the rate at which the measurements were made. In the present study, the thermal expansion was measured at a rate of 2°C/min which

allowed the sample plenty of time to achieve its equilibrium length at all temperatures. Although Brown et. al. did not state their heating rate, had the measurement been made at a faster rate, a lower expansion might be expected.

For the tetragonal phase, the thermal expansion coefficients for the compositions examined in this study were found to decrease with increasing TiO_2 (refer to Table 14). The values were much lower than the coefficients for tetragonal HfO_2 and ZrO_2 (10.0 x 10^{-6}/°C and 10.6 x 10^{-6}/°C, respectively). Since the range over which the measurements were made was small, the observed values might be a bit lower than the true values. Nonetheless, the reduced values from the pure phases further suggests that TiO_2 lowers the thermal expansion.

4.6.2 Transformation Temperatures

The monoclinic to tetragonal transformation temperatures can easily be identified in the thermal expansion curves shown in Figures 58-61. As the curves suggest, the transformation is spread over a temperature range and has a thermal cycle hysteresis (i.e., the transformation temperatures for the heating and cooling curves are not the same). Such behavior is typical of the HfO_2 and ZrO_2 fluorite structures. The strain energy due to the diffusionless transformation (i.e., atom displacements of less than an interatomic distance) in the fluorite structure adds an additional degree of freedom and consequently causes the transition to occur over a temperature range rather than at a single temperature. The large strains that are set up as the temperature increases are not relieved by atom migration, but rather by twinning.[102] This upsets the energy balance such that the reaction is not reversible at the same temperature thereby producing a thermal cycle hysteresis.[103]

The phase diagram of the HfO_2-ZrO_2 system (Figure 6) shows that when ZrO_2 is added to HfO_2, the transformation temperature range increases, while the transformation temperature decreases. The phase diagrams of the HfO_2-TiO_2 and the

ZrO_2-TiO_2 systems (Figures 7a and 8b, respectively) show that a similar behavior occurs when TiO_2 is added up to the point where the titanate begins to form. Beyond this point, a levelling off of the lower monoclinic to tetragonal transformation temperature is observed. In the present study, the thermal expansion curves show that additions of TiO_2 lower the transformation temperature and increase the transformation temperature range in a similar manner to that observed in the HT and ZT systems. Table 15 summarizes the transformation temperatures for the four compositions. It should be pointed out that at the same time that TiO_2 is being added in the present HZT system, ZrO_2 is being removed. This suggests that the effect of TiO_2 on the transformation temperature is greater than the effect of ZrO_2 since the trends due to the latter are totally reversed. It should also be pointed out that the levelling off of the transformation temperature (similar to that which is observed in the HT and ZT systems) occurs at the 15 mol% TiO_2 composition in the present HZT system. This corresponds to the composition at which the titanate begins to form and suggests that the solubility limit of TiO_2 in the present study is between 10 and 15 mol% (ca. 12 mol%).

The transformation that occurs in going from the reduced state to the oxidized state was also observed using both a hot stage x-ray diffractometer and a dilatometer in air. This inversion involves a cubic to monoclinic phase change. For each composition, the transformation temperature was found to be approximately 600°C. Figure 62 shows the thermal expansion trace.

The following observations were made for the $15T_2$ composition: (1) The initial thermal expansion of the reduced state material was found to be low ($\alpha \approx 5.0 \times 10^{-6}/°C$). (2) A large increase in length was observed during the cubic to monoclinic transformation. (3) The thermal expansion of the upper temperature region of the heating curve and the cooling curve were the same as that of the $15T_2$ox thermal expansion in Figure 60.

Table 15. Transformation Temperatures and Ranges for the Monoclinic to Tetragonal Inversion in the HZT System.

Composition (mol% TiO_2)	Transformation Range (°C)	Transformation Temperature (°C)
5	1387 - 1510	1469
	1551 - 1632	1591
10	1346 - 1449	1388
	1510 - 1592	1571
15	1286 - 1429	1367
	1408 - 1592	1551
20	1286 - 1450	1367
	1408 - 1592	1551

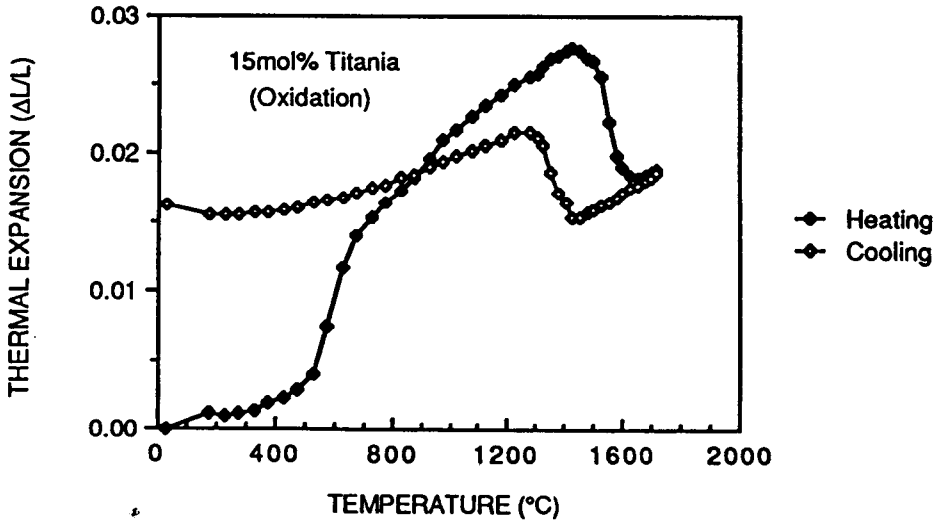

Figure 62. Linear thermal expansion of the 15 mol% TiO_2 composition upon oxidizing.

Several conclusions can be drawn from the oxidation curve. First, a rapid initial oxidation occurs at 600°C. Second, beyond 600°C, the oxidation is much more gradual. And third, once the oxidation is complete, the cubic phase no longer exists. One possible mechanism is a rapid oxidation at 600°C corresponding to the point at which a sufficient amount of energy is introduced to produce significant oxygen mobility, followed by an equilibrium mobility of oxygen as oxidation continues.

4.6.3 Microcracking

The effects of extensive microcracking can be observed in the 15 and 20 mol% TiO_2 thermal expansion curves. A hysteresis between the heating and cooling curves is evident. A correlation between the size of the hysteresis and the size of the microcracks can be made. The microstructures in Figures 44-52 show that the low TiO_2 compositions have very fine microcracks (less than one grain wide), whereas the microcracks in the high compositions are very large (approximately seven grains wide). Similarly, the hystereses in the thermal expansion curves of the high TiO_2 compositions are quite pronounced whereas in the low TiO_2 composition, the hysterses are negligible. The conclusion can then be made that large microcracks lead to the large hystereses in the high TiO_2 compositions.

4.7 Fracture Strength and Toughness

This section is divided into three parts. The first part examines the phase and microcracking dependencies of the strengths of reduced and oxidized compositions in the HZT system. Specifically, the effects of the cubic phase on the strength of reduced materials and the effects of the titanate phase on the strengths of oxidized materials are discussed. Also, compositions with various degrees of microcracking are examined to illustrate the effects of microcracking on strength. The second part of this section examines the effects of composition on fracture toughness. Materials in both

the oxidized and reduced states are investigated. The final part of this section examines the effects of temperature on the fracture strength and toughness of the oxidized compositions in the HZT system. A similar examination of the reduced compositions was not made due to testing apparatus limitations and limited material supplies. Further examination of these materials to determine the high temperature strength and toughness in reducing environments is warranted.

4.7.1 Fracture Strength

Fracture strength values were determined by placing bars in a four-point bend load fixture. The tensile side of the test bars was polished to a $\frac{1}{4}$ μm diamond finish to minimize the number and size of surface flaws. The edges were bevelled to reduce the stress concentration effects of sharp corners. Measurements were taken of the load at fracture and the bar dimensions at the site of fracture. Using Equation (46), the modulus of rupture (or fracture strength) was calculated for each sample.

The modulus of rupture for both indented and nonindented bars were determined. As discussed in Section 2.2.3.2.1, controlled flaw fractures (as occur from preindented specimens) generally give reproducible MOR values. However, the measured values do not always give an adequate assessment of the material strength (i.e., the measured MOR values tend to be low). On the other hand, fractures from nonindented specimens tend to give high MOR values but with large degrees of scatter. Therefore, MOR measurements for both indented and nonindented bars were made in order to give both an accurate assessment of the strengths of HZT compositions and to determine the reproducibility of the measured trends.

Between three and twelve bars of each composition for each series were tested. Due to the low number of bars tested, a Weibull plot could not be made. Instead, the statistical nature of the fracture strength was given as a 90% confidence interval as

determined from Student's t distribution curves.[104] Such curves are generally used for low sample populations. The strength was therefore reported as:

$$\bar{x} \pm t_{0.10/2,\, n-1} \frac{s_x}{\sqrt{n}} \qquad (103)$$

where $\bar{x}$ is the average of the n measured values (e.g., MOR values), $t_{0.10/2,\, n-1}$ is the value from the Student's t distributions for a 90% confidence interval for n-1 values, and s_x is the standard deviation of the n values.

4.7.1.1 Nonindented Bars

Modulus of rupture values of nonindented bars were determined for each composition in the T_1, T_2, and T_3 series. Both the reduced and the oxidized states were examined. The effects of titania on the strengths of the HZT compositions are shown in Figure 63. The data is replotted in Figure 64 to show the relative strengths for the different fabrication techniques. From Figures 63 and 64, the effects of phase changes and microcracking on fracture strength can be seen.

4.7.1.1.1 Reduced State

As was discussed in Section 4.4, phase analyses of the T_1 and T_2 series showed that in the reduced state, the low TiO_2 compositions were essentially monoclinic and the high compositions essentially cubic. Intermediate compositions were shown to be mixtures of the two phases. In the T_3 series, all but the 20 mol% composition were found to be monoclinic. With regard to fracture behavior, in Section 2.2.3.1 it was pointed out that pure cubic stabilized ZrO_2 had strengths which were approximately 32% lower than either pure monoclinic ZrO_2 or mixtures of the cubic and monoclinic phase. Figures 63 and 64a suggest that a similar situation occurs in the reduced compositions of the HZT system. Compositions having predominantly the cubic phase exhibited low strengths (<250 MPa) while those having predominantly the

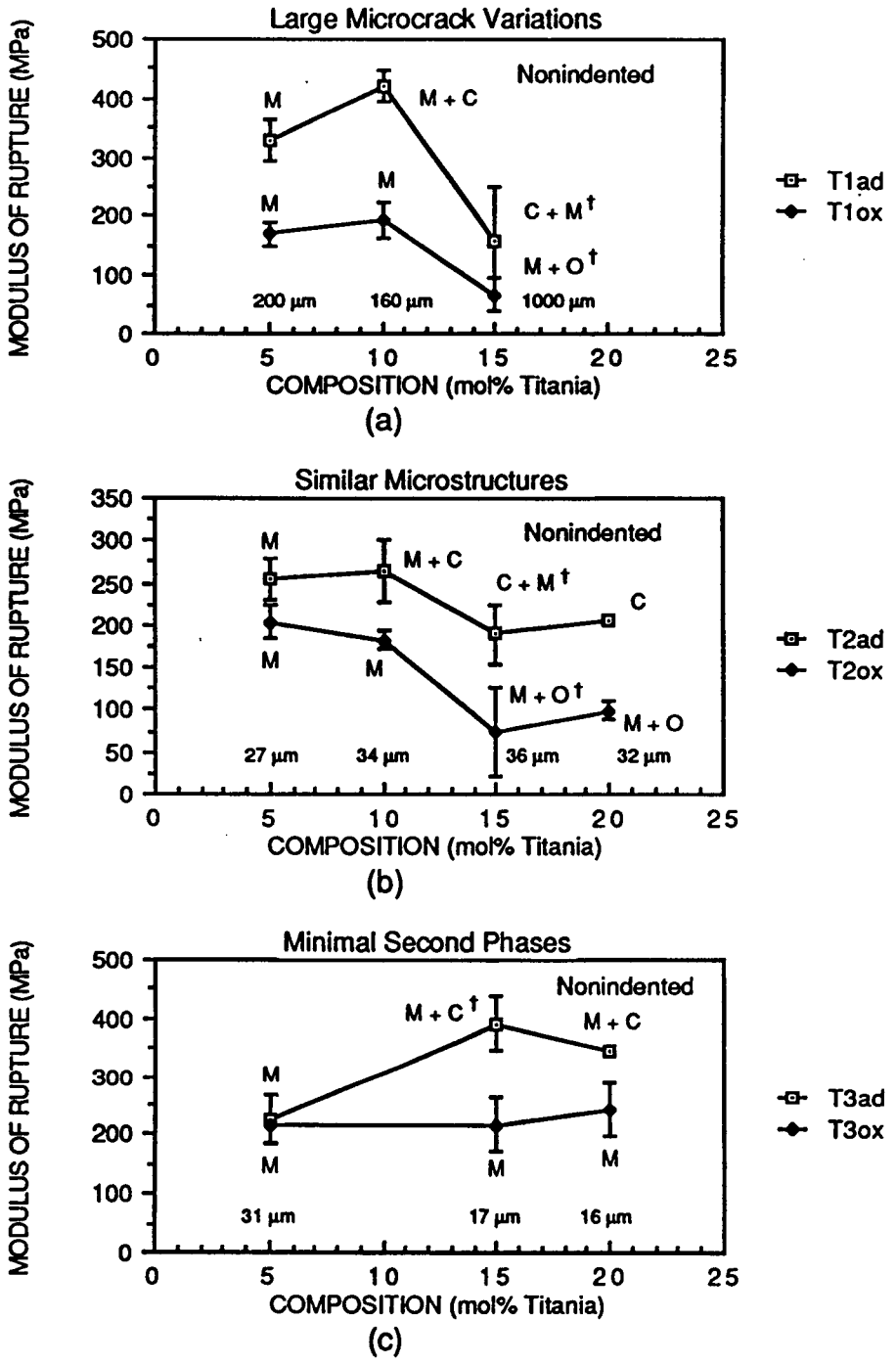

Figure 63. Fracture strengths of nonindented highly anion deficient (ad) and oxidized (ox) HZT compositions made from (a) reaction-sintered (T_1), (b) as-received (T_2), and (c) plasma-sprayed powders (T_3). Phases are indicated by the symbols M (monoclinic), C (cubic), and O (orthorhombic). (A † indicates trace amounts.) Average microcrack region sizes are placed above each composition.

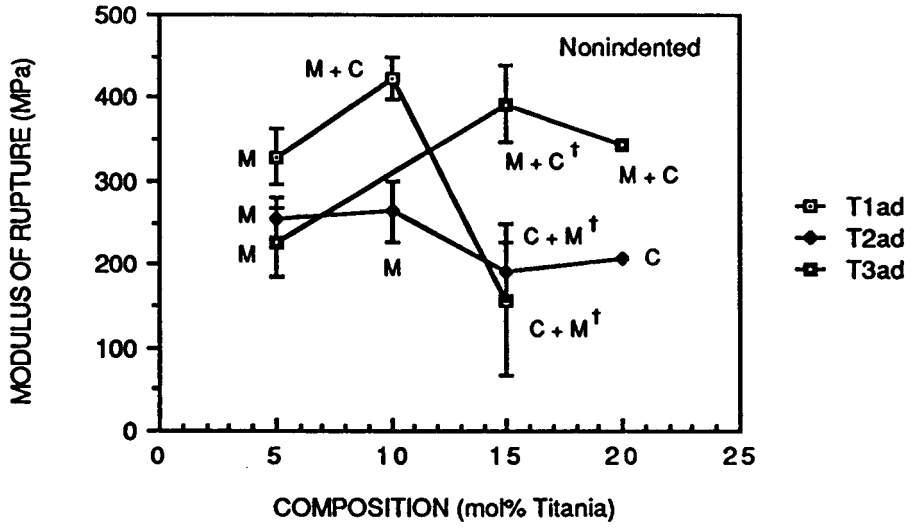

(a)

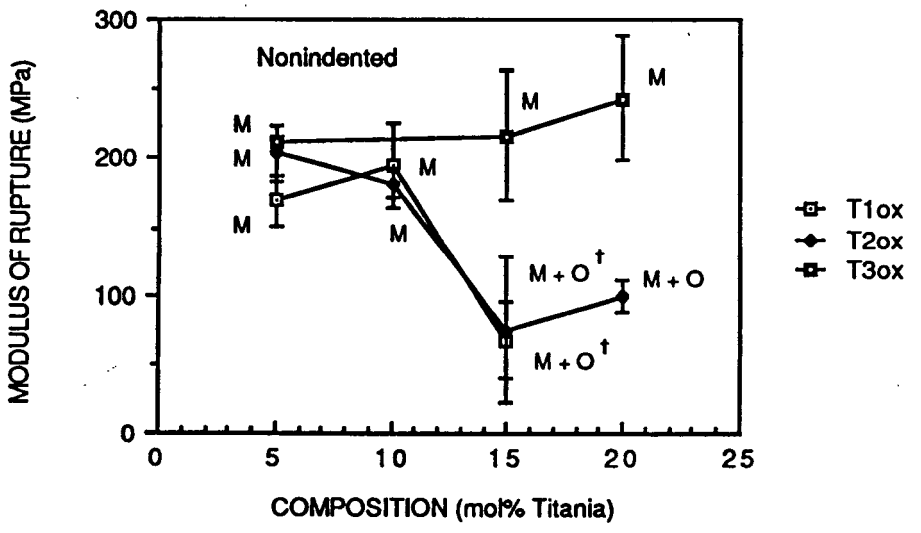

(b)

Figure 64. Fracture strengths of nonindented HZT compositions in the T_1, T_2, and T_3 series in the (a) reduced and (b) oxidized states. Phases are indicated by M (monoclinic), C (cubic), and O (orthorhombic).

monoclinic phase had relatively high strengths (>250 MPa).

The T_2ad series best illustrates the effects of the cubic phase on strength. In this series, the microstructure was essentially the same for all compositions (i.e., the grain size, microcrack region size, and porosity were basically identical). Consequently, the strength was primarily affected by compositional or phase effects. A very decisive decrease in strength was observed in the T_2ad series with increasing cubic phase concentration (see Figure 63b). Hence, the strength was determined to be inversely proportional to the amount of cubic phase present.

The T_3ad series best illustrates the effects that suppressing the cubic phase has on strength. In this series, concentrations of the cubic phase were minimal (i.e., essentially no cubic phase was observed in the $5T_3$ad and $15T_3$ad compositions, and only small concentrations were observed in the $20T_3$ad composition). Consequently, the effects of titania on the strength of HZT materials in the reduced state could be determined. Figure 63c shows that the resultant strengths of the materials were relatively high (>200 MPa) and increased with TiO_2 concentration. A decrease in strength occurred at the 20 mol% composition corresponding to the emergence of the cubic phase.

The T_1ad series also showed a decrease in strength with increasing cubic phase concentration (approximately a 61% reduction). More importantly though, the series illustrated the effects of microcracking on the strength. From microstructural analyses, the microcrack region sizes of all the compositions in the T_1 series were found to be high (>160 μm). A large amount of fluctuation in the sizes also occurred. From an examination of Figure 63a, a correlation between strength and microcrack region size can be seen. The compositions with large microcrack sizes tended to have low strengths. This correlation is further substantiated by the extremely low strength of the $20T_1$ad composition. (For this composition, all samples broke prior to testing due to the load exerted on them during polishing.) The $20T_1$ad compositions had very

large microcrack regions (of the order of 3000 μm) and tended to break readily along region boundaries.

4.7.1.1.2 Oxidized State

Phase analyses of the T_1 and T_2 series showed that for HZT compositions in the oxidized state, the low TiO_2 compositions were essentially monoclinic and the high compositions were a mixture of monoclinic and titanate phases. As was pointed out in Section 2.2.3.1, the titanate phase tends to drastically reduce the strength of materials in the HfO_2-TiO_2 system (e.g., the MOR drops to approximately 40 MPa when $HfTiO_4$ forms). This weakening effect can be associated with the low thermal expansion and the high degree of microcracking that occurs in the system when the titanate is present. The following conclusions were made: (1) The anisotropic expansion of the titanate phase leads to extensive microcracking which gives low thermal expansion. (2) The extensive microcracking makes the material weak.

The effects of the titanate phase on the thermal and mechanical properties of the present compositions in the HZT system were similar to those found in the HT system. Figures 50 and 51 show that a large degree of microcracking occurred in the high TiO_2 HZT compositions. Also, the thermal expansion coefficients were found to be moderately low (refer to Table 14). Consequently, the material was weak (Figures 63a and b).

The T_3ox series, illustrates the effects that suppressing the titanate phase has on the strength of oxidized compositions in the HZT system. In this series, all the compositions were essentially pure monoclinic solid solutions with the exception that trace amounts of the titanate phase were found in the $20T_3$ox composition. As pointed out in Sections 4.2 and 4.3, the bars approached 100% theoretical density and had no apparent impurities. Fracture surfaces suggest that indeed little porosity existed in these compositions (see Figures 65-68). Also, Figure 52 suggests that the severity of

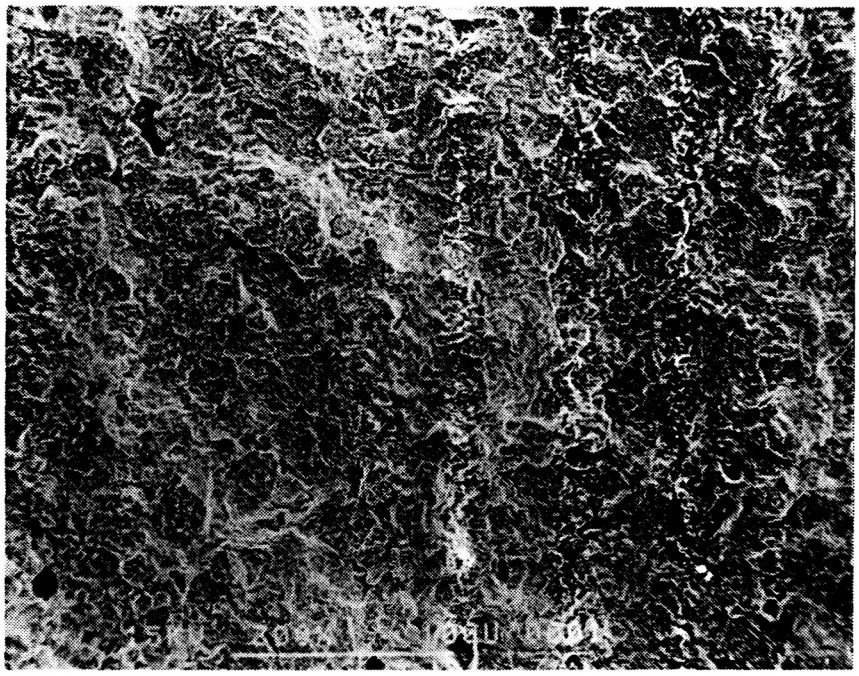

Figure 65. Scanning electron micrograph of the fracture surface of a $5T_3ox$ bar.

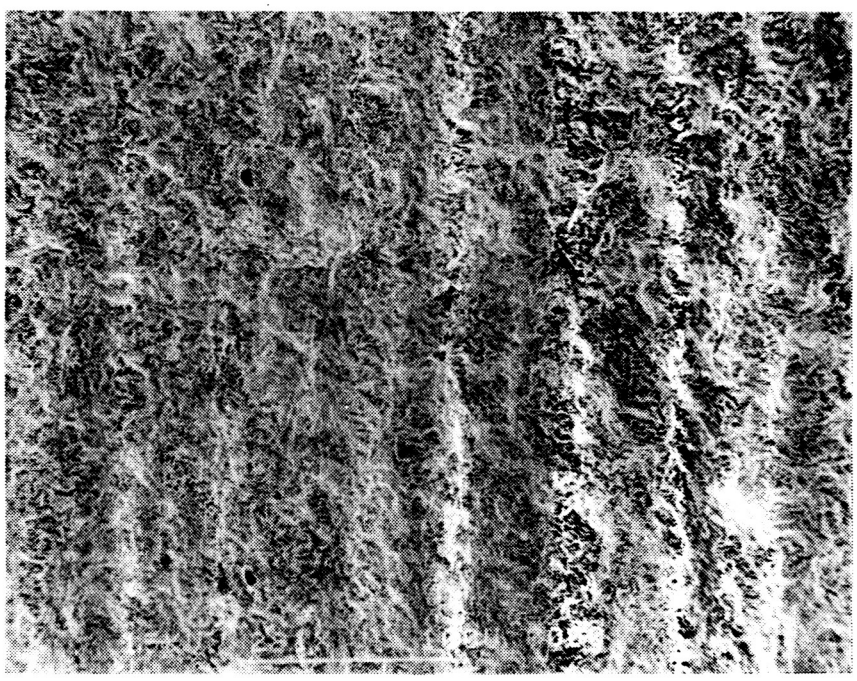

Figure 66. Scanning electron micrograph of the fracture surface of a $10T_3ox$ bar.

Figure 67. Scanning electron micrograph of the fracture surface of a $15T_3ox$ bar.

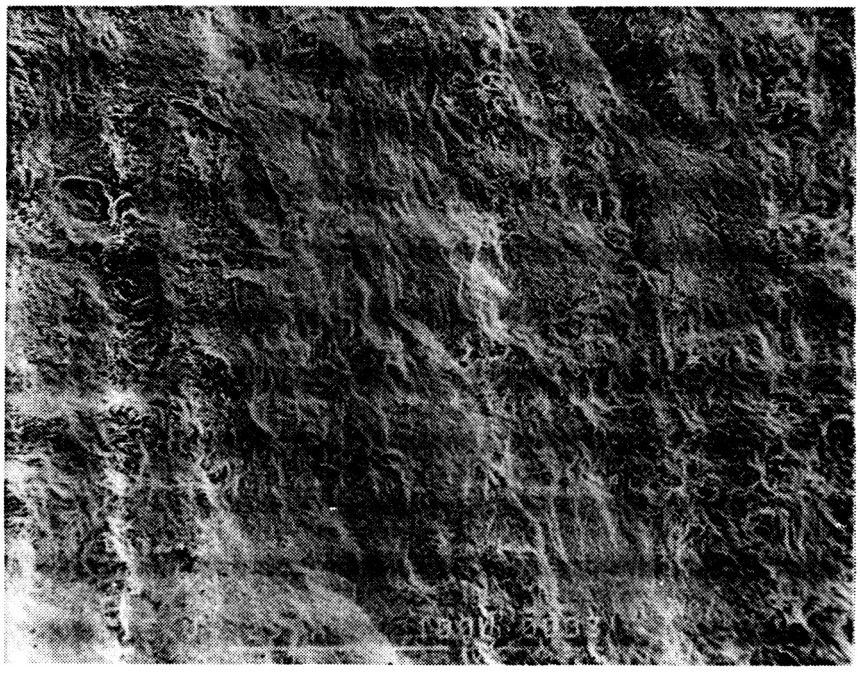

Figure 68. Scanning electron micrograph of the fracture surface of a $20T_3ox$ bar.

the microcracking was minimal. These factors imply that the resultant strengths are indicative of the true effect that TiO_2 has on the fracture strength of monoclinic solid solutions in the system. Figure 63c indicates that the effect of TiO_2 is to increase the strength as long as the titanate phase is suppressed.

4.7.1.2 Indented Bars

Modulus of rupture values of indented bars were determined for each composition in the T_1 and T_2 series. The T_3 series was not examined because not enough bars could be produced of each composition to give an adequate assessment of the indented strength. (The $10T_3$ and $15T_3$ compositions suffered thermal shock damage during the cooling cycle of the hot press runs such that only a few one inch bars could be cut from the two inch disks. The bars that were produced were used in the nonindented fracture study.) Room temperature measurements of strength were made for both the reduced and oxidized states. Figure 69 summarizes the results. Trends in the strength measurements of the indented samples were similar to those observed in the nonindented samples. That is, the fracture strengths of the highly anion deficient and oxidized bars decreased with increasing TiO_2 concentration due to the cubic and titanate phases, respectively.

The strengths of the indented bars were about half that of nonindented bars. Section 2.2.3.2 pointed out that in indentation techniques, a decrease in strength of this magnitude is expected. The reproducibility, however, was much better, as the error bars in Figure 69 suggest.

A difference in the nature of the indents for the T_1 and T_2 series resulted due to the difference in the method of indentation. In the T_1 series, indents were first made on the bars in the reduced state and subsequently, the bars were oxidized. In the T_2 series bars were first oxidized and then indented. The effect on strength, from Figure 69, was apparently minimal since the magnitudes of the MOR values of the T_1 and T_2

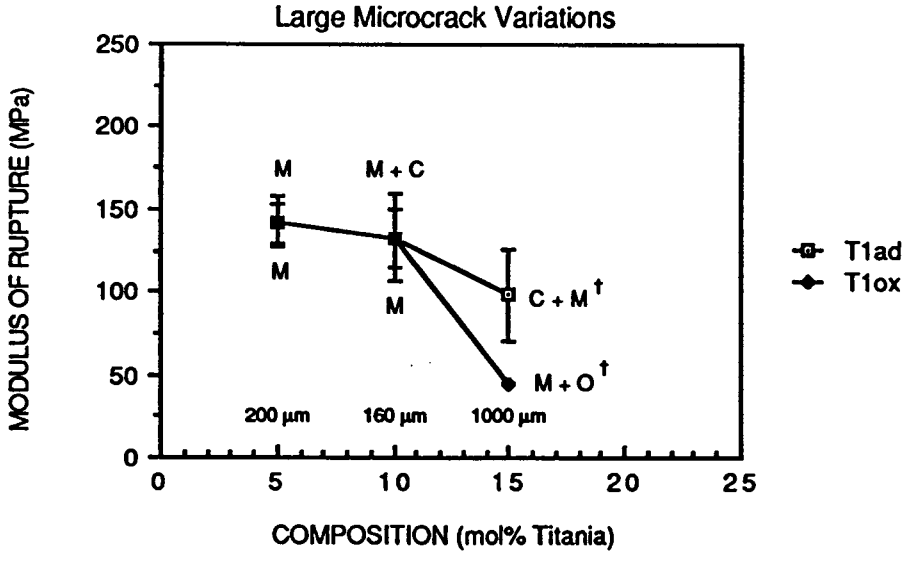

(a)

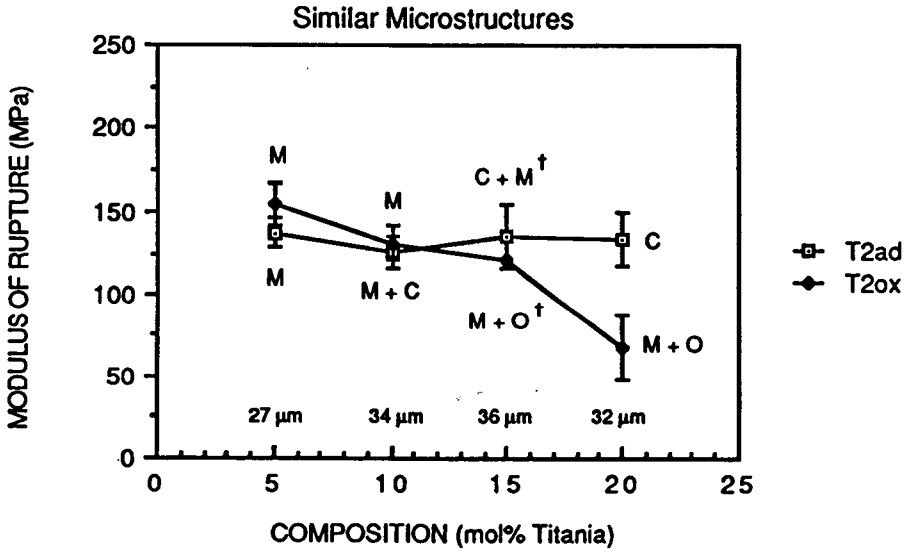

(b)

Figure 69. Fracture strengths of indented reduced and oxidized HZT compositions made from (a) reaction-sintered (T_1) and (b) as-received powders (T_2). Phases and microcrack region sizes for each composition are given.

series are about the same. The appearance of the indents, on the other hand, was not the same. In the T_2ox series, the indents and crack extensions appeared sharp and well defined whereas those in the T_1ox series were diffuse and irregular. Grain boundary etching and strain relief movement in the T_1 series due to annealing probably accounts for the difference in appearance.

All breaks occurred at one of the three indents for all the compositions except the 5T_1ox. For this composition, fractures never occurred at an indent and rarely occurred within the region where indents were placed. Both the appearance of the indented region and the fracture nature suggest that microcrack toughening occurred for this composition. A further examination of this material is warranted.

The fracture surfaces of the indented bars in the T_1 and T_2 ox series are shown in Figures 70-76. These figures confirm that a high degree of porosity was present in the compositions and that fracture occurred along grain boundaries. In the high TiO_2 compositions, evidence of fracture along microcrack region boundaries was apparent and microcracks within the inner regions of the bars could be seen (see Figure 76b).

4.7.2 Fracture Toughness

The fracture toughness was determined for indented bars in the T_1 and T_2 series. K_{1C} values were calculated using Equation (51) and using both the measured MOR values and surviving crack lengths of each sample. Plots of the results are given in Figure 77.

In general, the fracture toughness decreased with increasing TiO_2 for both the reduced and oxidized states. Trends similar to those found in the strength measurements were observed. In the reduced state, the toughness values of compositions possessing the cubic phase were found to be lower than those which were mostly or all monoclinic. In the oxidized state, the toughness was observed to decrease with increasing titanate phase concentration.

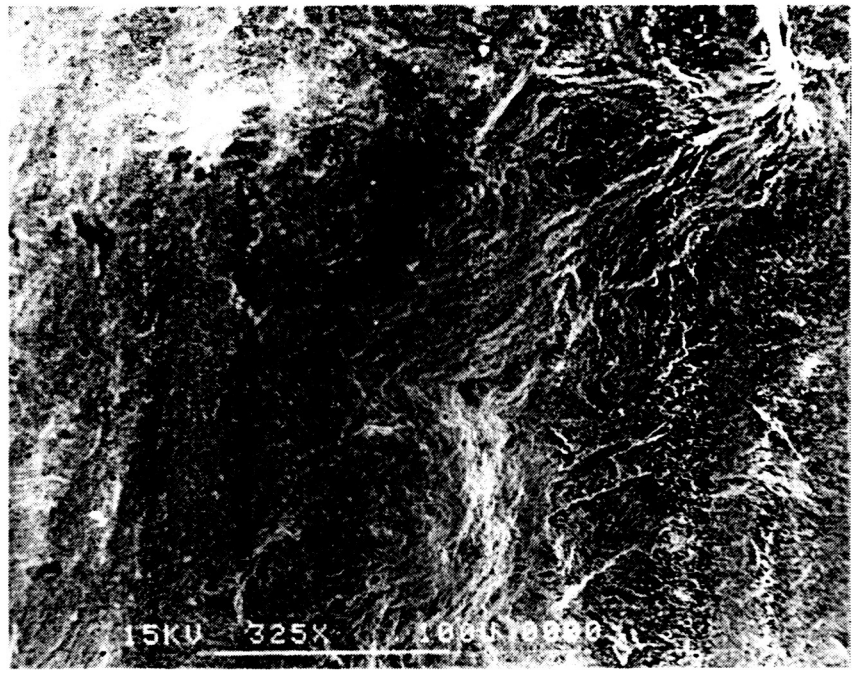

Figure 70. Scanning electron micrographs of the fracture surface of a $5T_1$ox bar.

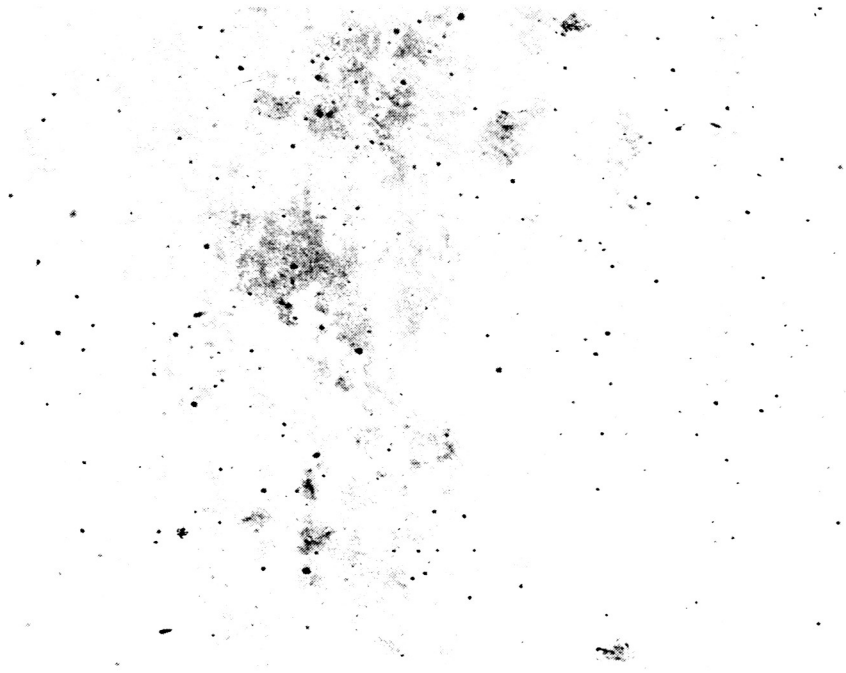

Figure 71. Scanning electron micrographs of the fracture surface of a $10T_1$ox bar.

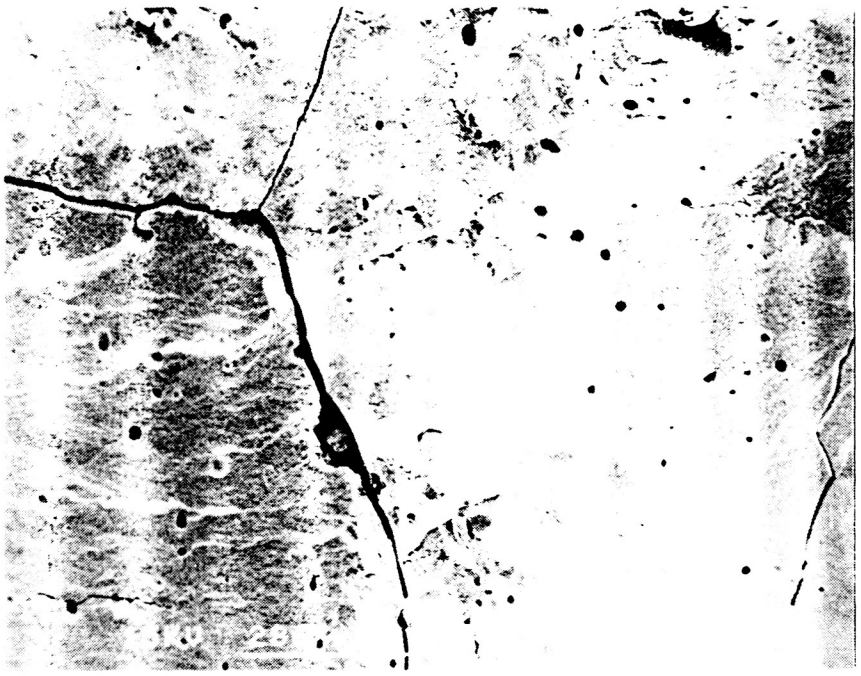

Figure 72. Scanning electron micrographs of the fracture surface of a $15T_1ox$ bar.

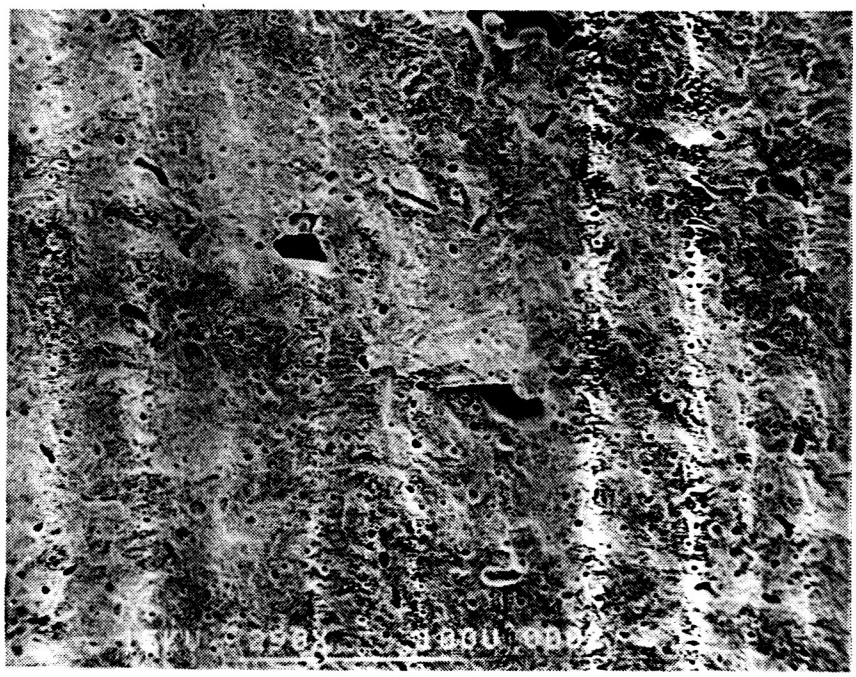

Figure 73. Scanning electron micrographs of the fracture surface of a $5T_2ox$ bar.

Figure 74. Scanning electron micrographs of the fracture surface of a $10T_2$ox bar.

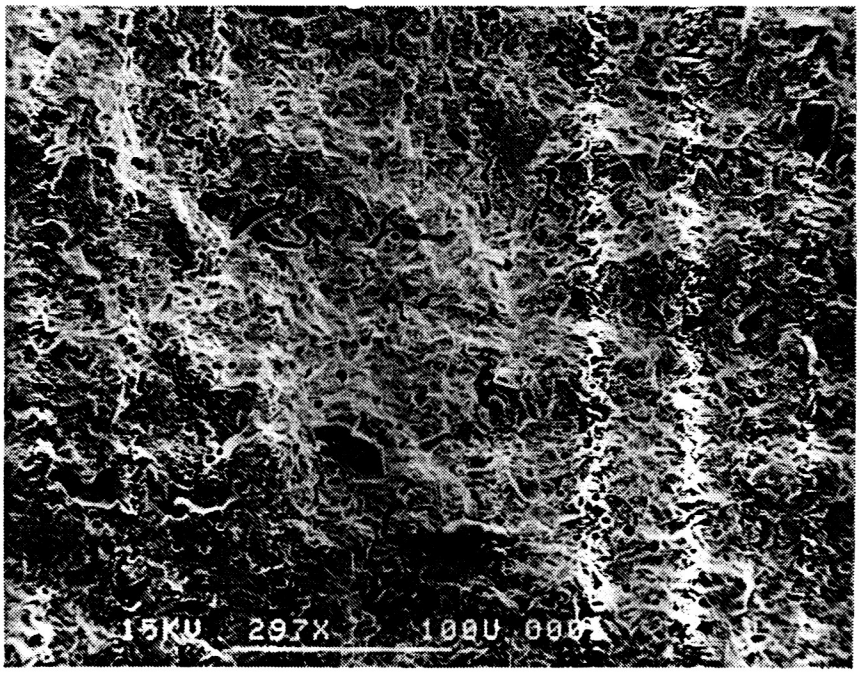

Figure 75. Scanning electron micrographs of the fracture surface of a $15T_2$ox bar.

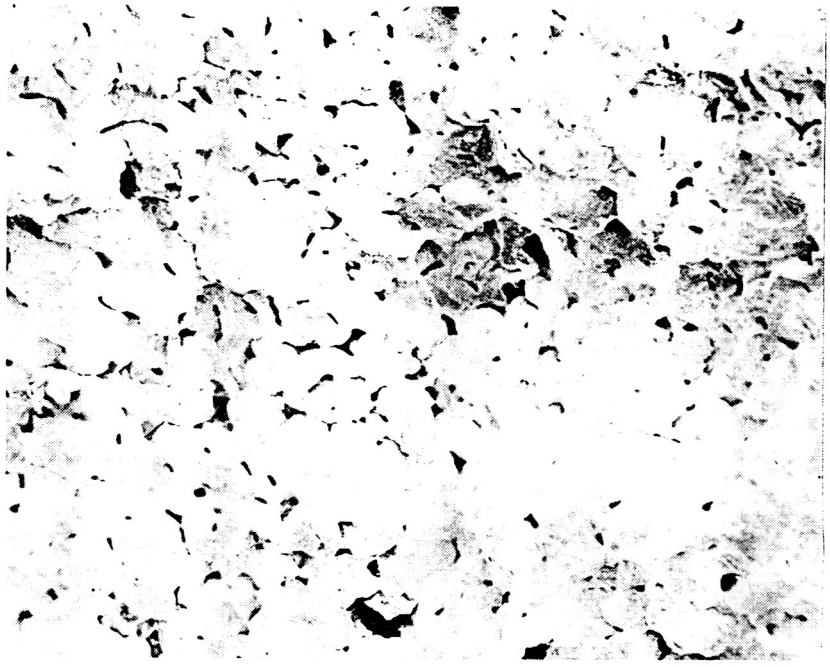

(a)

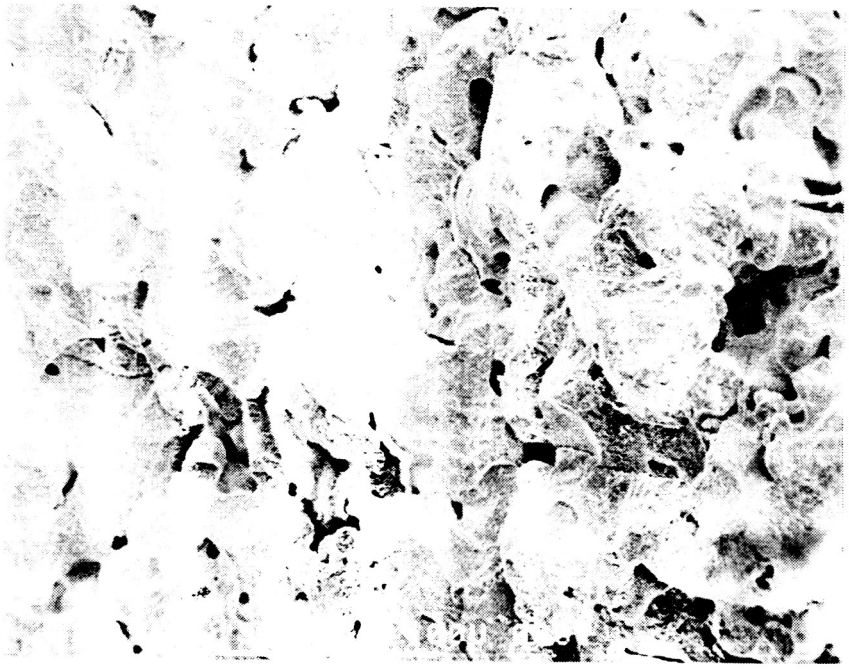

(b)

Figure 76. Scanning electron micrographs of the fracture surface of a $20T_2ox$ bar at (a) low magnification and (b) high magnification.

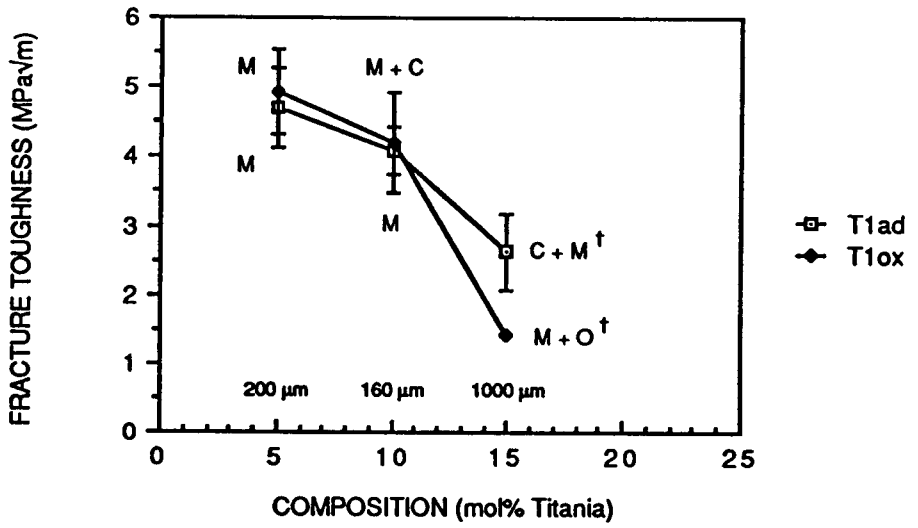

(a)

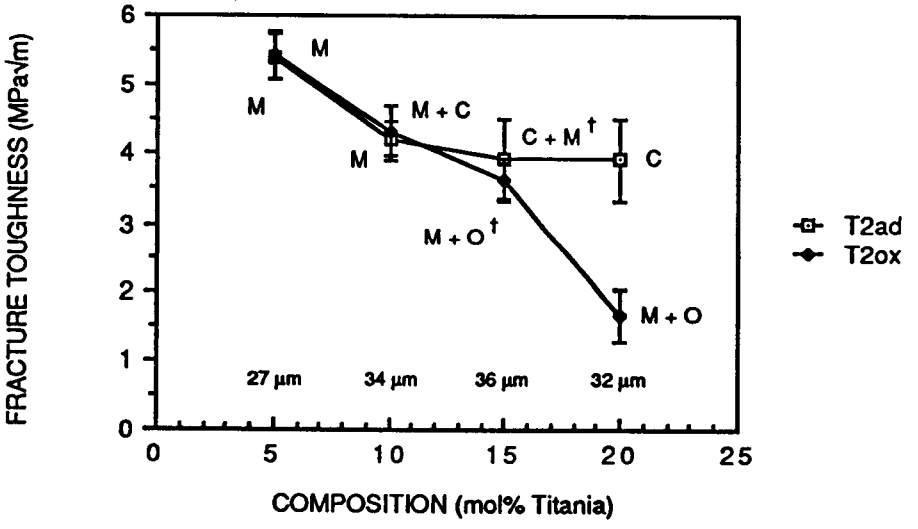

(b)

Figure 77. Fracture toughness of reduced and oxidized compositions in the (a) T_1 and (b) T_2 series. Phases and microcrack region sizes are given.

A comparison of the T_1 and T_2 series shows that the large microcracks in the high TiO_2 compositions of the T_1 series act to accelerate crack propagation thereby reducing the toughness. The high TiO_2 compositions of the T_2 series (which do not have large microcracks) have higher K_{1C} values. In the low TiO_2 compositions, microcracking had little effect on the K_{1C} except in the $5T_1ox$ composition. Annealing of the indents in this composition apparently led to microcrack hardening. Crack propagation was decelerated due to the stress relief which resulted from the alignment of microcracks. The bars never broke at indents and rarely broke within the indented region. Consequently, the measured strength as well as the measured fracture toughness values of this composition are most likely lower than the true material values.

A comparison with literature values suggests that the K_{1C} values for the highly cubic reduced HZT compositions were of the same order of magnitude as those of fully stabilized cubic zirconia (i.e., 2 to 4 $MPa \cdot m^{\frac{1}{2}}$ as compared to 1.8). The monoclinic HZT compositions had K_{1C} values of the order of 5 to 6 $MPa \cdot m^{\frac{1}{2}}$ which is comparable to monoclinic HfO_2 and ZrO_2.

4.7.3 Temperature Dependence of MOR and K_{1C}

The fracture strengths and toughnesses were determined as a function of temperature for each composition in the T_1 and T_2 series. Indented bars that were oxidized at 1200°C, were heated to 1000°C and to 1400°C in air and broken at temperature. Figures 78 and 79 show the results. In general, a decrease in strength and toughness occurred for samples fractured at 1000°C, as compared with room temperature values, and an increase occurred for bars fractured at 1400°C.

The literature suggests that a decrease in strength and toughness with increasing temperature is expected for HfO_2- and ZrO_2-based materials (refer to Figure 24). On the other hand, an initial increase in strength with temperature is expected for

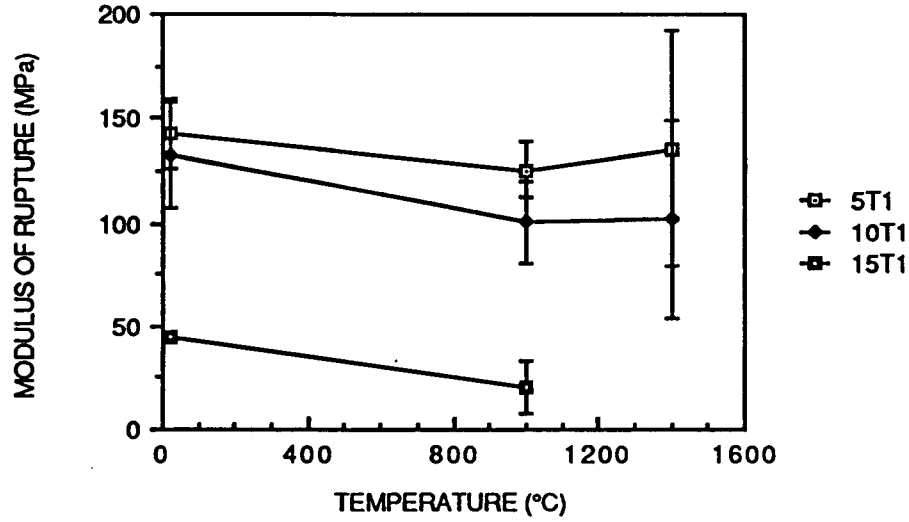

(a)

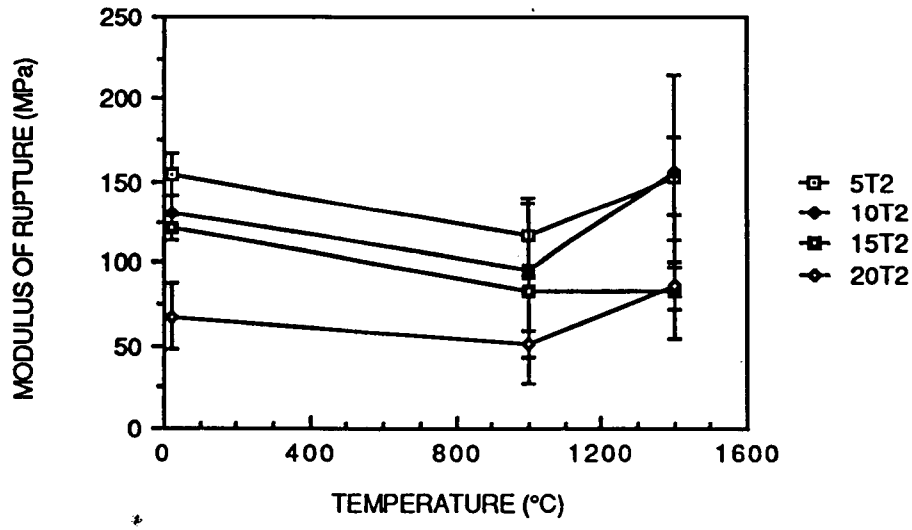

(b)

Figure 78. Temperature dependence of the fracture strength for compositions in the HZT system in the (a) T_1 and (b) T_2 series.

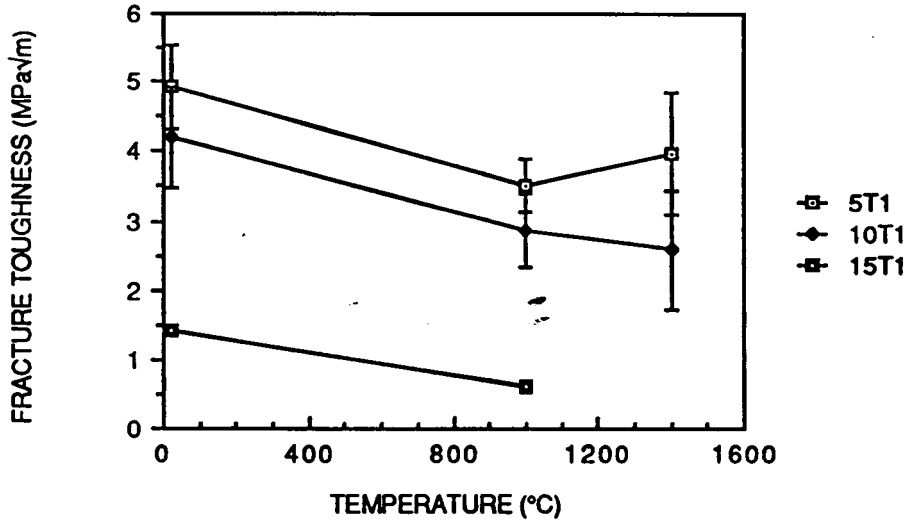

(a)

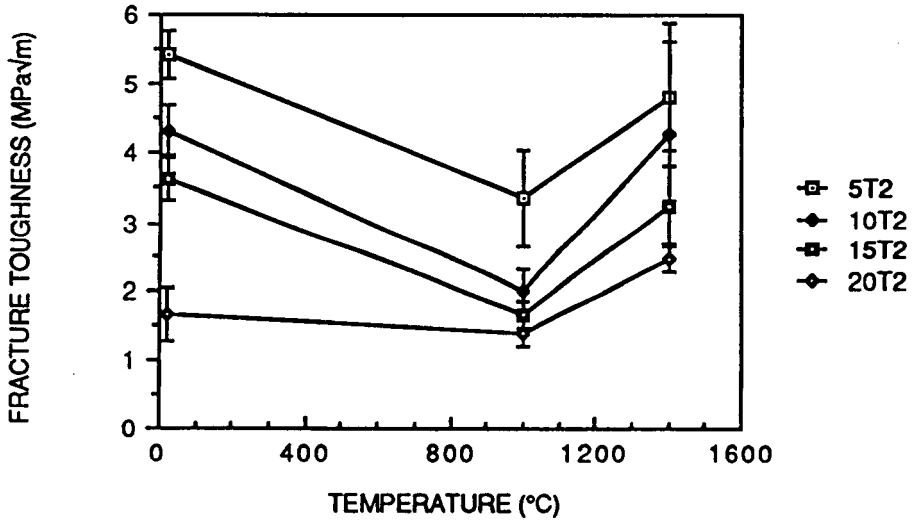

(b)

Figure 79. Temperature dependence of the fracture toughness for compositions in the HZT system in the (a) T_1 and (b) T_2 series.

materials which have microcracks (refer to Figure 25). In the present study of the HZT system, the results were mixed. A slight decrease in strength (several percent) occurred at 1000°C which was offset by an increase at 1400°C. As was pointed out in Section 2.2.3, strength tends to be invariant (or increase slightly) with temperature in the range where fracture is elastic. Preexisting flaws and microcracking dominate the fracture behavior in this temperature range.

The increased strengths at 1400°C suggest that microcracking effects (i.e., microcrack healing) are present in the HZT compositions. (The higher temperature elicits a material expansion that closes microcracks and consequently increases the strength.) The lowered strengths at 1000°C suggest a situation exists whereby microcracking does not dominate the fracture behavior.

The lower values of strength and toughness found in the T_1 series as compared with the T_2 series confirm the correlation between microcrack size and fracture behavior presented in the previous sections. In the T_2 series, microcracks were small (approximately 30 μm) giving high strength and toughness values. In the T_1 series, microcracks were larger giving slightly lower values.

The effects of microcrack healing on strength and toughness can be associated with microcrack size. Microcracks in the T_1 series were found to be many times wider than those in the T_2 series (refer to Figures 44-51). The enhancement in strength associated with the closing of the narrow cracks in the T_2 series was greater than that of the wider cracks in the T_1 series. A comparison of the curves in Figures 78 and 79 illustrates the magnitude of the strength improvement effects.

In addition to microcrack healing effects, oxidation effects were also involved. The materials studied in this investigation were initially oxidized at 1200°C. Subsequently, the materials were tested at temperatures above and below this temperature. The indentation procedures for the two series, however, were not the same. As was pointed out in Section 4.7.1.2, bars in the T_1 series were indented and

then oxidized, whereas bars in the T_2 series were oxidized then indented. An examination of Figures 78 and 79 shows that the severity of the reduction in strength and toughness with temperature is less in the T_1 series than in the T_2 series. This difference suggests that during the oxidation of the indented T_1 bars, an annealing or crack healing of the indents occurred. Furthermore, the indented T_2 bars which were not annealed prior to fracture did not experience crack healing.

In summary, microcrack healing in both the T_1 and T_2 series accounted for the increase in strength and toughness with temperature. Those compositions which had noticeable increases tended to be in the T_2 series where microcracks were relatively small. Large microcracks in the T_1 series led to less strength improvement.

5. CONCLUSIONS

(1) The solubility limit of TiO_2 in the studied HZT system was determined to be between 10 and 15 mol%. Phase analyses showed that below 15 mol%, the HZT compositions were monoclinic solid solutions, while above 15%, the materials were titanates in a monoclinic solid solution.

(2) The oxidation states and fabrication processes were found to significantly affect the final phases and microstructure of the compositions examined in the HZT system. X-ray analyses showed that as the titania concentration was increased, an increase in the concentration of the cubic phase in the reduced state was observed. The degree of anion deficiency produced during fabrication determined the amount of cubic phase present. In the oxidized state, an increase in the titanate phase concentration was observed. Incomplete oxidation tended to suppress the titanate phase and extend the monoclinic solid solution limit. Microstructural analyses showed that hot pressed materials were highly dense, whereas sintered materials had up to 8% porosity. While microcrack sizes varied greatly with composition and fabrication technique, grain sizes were approximately 1 μm for all compositions and varied only slightly.

(3) A model was proposed for the P_{O_2} dependence on the electrical conductivity of TiO_2 doped HfO_2-rich mixed oxides. In the model, the titanium was incorporated interstitially at high P_{O_2} and substitutionally at low P_{O_2}. The measured P_{O_2} dependence showed similar trends to those suggested by the model.

(4) An explanation of the low thermal expansion of materials in the HZT system was given. Depending on the oxidation state, materials had low thermal expansion coefficients due to either the presence of the titanate phase or the presence of the high TiO_2 monoclinic phase.

Thermal expansion coefficients were shown to decrease with increasing titania concentration for HZT compositions. Microcracks were also shown to reduce the

thermal expansion. Extensive microcracking (resulting from the anisotropic nature of the titanate phase) occurred in the high TiO_2 compositions leading to low thermal expansion coefficients and producing thermal cycle hystereses as well.

(5) Fracture strength and toughness increased with TiO_2 when the titanate phase was suppressed. When the titanate phase formed, the strength and toughness was reduced substantially. Microcracking also weakened the high TiO_2 compositions and strengthened the low compositions under certain oxidation conditions.

The temperature dependence of the strength and toughness went through a minimum and then increased. The increase in strength was attributed to microcrack healing at temperatures above the oxidation temperature.

6. SUGGESTIONS FOR FUTURE WORK

(1) Phase analyses of fully oxidized materials for a wider range of titania compositions need to be performed.

(2) Variations in the concentrations of hafnia and zirconia need to be made in order to more fully study the effects they have in the HZT system.

(3) A ternary phase equilibrium diagram of the HZT system needs to be constructed.

(4) The mechanism which inhibits sintering and grain growth in TiO_2 doped hafnia-rich mixed oxides needs to be determined.

(5) Electrical conductivity measurements at several more oxygen partial pressures need to be made in order to fully prove the defect model.

(6) Linear thermal expansion data needs to be taken to higher temperatures in order to accurately determine the tetragonal thermal expansion coefficient.

(7) Fracture strength and toughness measurements need to be made above 1400°C to fully determine the high temperature strength effects.

(8) The effects of various atmospheres (e.g., reducing) on the thermal expansion and strength of compositions in the HZT system need to be examined.

(9) The effect of titania on the thermal conductivity, creep, and elastic modulus in the HZT system needs to be determined.

APPENDICES

APPENDIX I. Impurity Content of Hafnia, Zirconia, and Titania Used in the HZT Experiments.

Table I.1 Impurity Content of Teledyne Wah Chang Albany HfO_2.

Lot Analysis in ppm	
Element	Results
Al	<35
B	0.4
Ca/HfO_2	<20
Cd	<0.2
Co	<5
Cr	<20
Cu	<25
Fe	<50
Mg	<10
Mn	<25
Mo	<25
Na/HfO_2	<20
Ni	<25
Pb	<10
Si	<100
Sn	<10
Ti	<25
U/HfO_2	12
V	<10
W	<10
Zn	<50
Zr	0.98%

Impurities on Hf metal basis unless otherwise noted.

Table I.2 Impurity Content of Magnesium Elektron ZrO_2 Development Grade XZ0544/1.

Analysis	
Properties	Results
SiO_2	0.12%
TiO_2	0.12%
Fe_2O_3	<0.02%
SO_3	0.07%
Particle Size (d_{50} Coulter)	1.9 μm
Surface Area (Quantasorb)	3.8 m^2/g

Table I.3 Impurity Content of J.T. Baker Chemical Company TiO_2 Baker Analyzed Reagent.

Analysis	
Element	Results
As	<.00005%
Fe	0.01%
Pb	0.005%
Zn	0.01%

APPENDIX II. Thermal Expansion of Standard Single Crystal Sapphire.

U.S. Department of Commerce
Juanita M. Kreps
Secretary
National Bureau of Standards
Ernest Ambler, Acting Director

National Bureau of Standards Certificate

Standard Reference Material 732

Single Crystal Sapphire - Thermal Expansion

T. A. Hahn

Thermal Expansion and Expansivity as a Function of Temperature (IPTS-68)

T	$\frac{L-L_{293}}{L_{293}}$	$\alpha = \frac{1}{L_{293}}\frac{dL}{dT}$	T	$\frac{L-L_{293}}{L_{293}}$	$\alpha = \frac{1}{L_{293}}\frac{dL}{dT}$
293 K	0×10^{-6}	5.38×10^{-6} K^{-1}	900 K	4608×10^{-6}	8.79×10^{-6} K^{-1}
300	38	5.48	1000	5500	9.05
350	328	6.12	1100	6417	9.29
400	647	6.61	1200	7357	9.52
450	987	7.00	1300	8320	9.74
500	1346	7.32	1400	9306	9.97
550	1719	7.59	1500	10314	10.20
600	2104	7.82	1600	11345	10.42
650	2500	8.02	1700	12399	10.66
700	2906	8.20	1800	13477	10.89
750	3320	8.37	1900	14578	11.14
800	3743	8.52	2000	15704	11.38

This single-crystal sapphire was grown from the melt, cut into 20 cm lengths, and centerless ground to 6.4 mm diameter. Back reflection Laue photographs of each rod gave an average orientation of the c-axis of the crystal relative to the rod axis equal to 59°. Several rods were checked for variations in orientation along their lengths, but none were found. Three specimens that were thought to have the greatest difference in orientation, ~1°, were selected for the thermal expansion measurements. The expansion of these three specimens from room temperature to 1000 K, however, did not differ by more than $4 \cdot 10^{-6}$. This is well within the precision of the measurement system, and indicates that no significant difference exists between any of the rods. The tabulated values were calculated from an equation whose parameters were determined by a least squares analysis of the pooled expansion data. Three-point interpolation of the tabulated data may be used to obtain values not listed. Descriptions of the experimental methods, the equation used to fit the data, and estimates of uncertainties are given in this certificate and in reference [1].

The technical and support aspects involved in the acquisition, preparation, certification, and issuance of this Standard Reference Material were coordinated through the Office of Standard Reference Materials by R. K. Kirby.

Washington, D.C. 20234
October 3, 1977

J. Paul Cali, Chief
Office of Standard Reference Materials

REFERENCES

1. F. H. Simpson, "High Temperature Structural Ceramics," *Mat. Design. Eng.*, **52** [2] 16-18 (1960).

2. T. F. Schroeder and O. E. Accountius, "Ceramic Throat Inserts," Rocketdyne Research Report No.: 63-29, Rocketdyne, Canoga Park, CA, October, 1963.

3. T. F. Schroeder, "Ceramic Throat Inserts," Rocketdyne Research Report No.: 64-46, Rocketdyne, Canoga Park, CA, October, 1964.

4. S. D. Brown, T. F. Schroeder, and E. E. Conabee, "Process and Article Comprising a Layer of a Ternary Composition of Hafnia, Zirconia, and Titania Bonded to a Silica Substrate," U.S. Patent 3,657,063, April 18, 1972.

5. S. R. Skaggs, "Zero and Low Coefficient of Thermal Expansion Polycrystalline Oxides," *Rev. Int. Hautes Temp. Refract.*, **16**, 157-67 (1979).

6. L. Pauling, Nature of the Chemical Bond, 3rd Edition. Cornell University Press, Ithica, New York, 1960.

7. A. H. Heuer and M. Rühle, "Phase Transformations in ZrO_2 Containing Ceramics: I, Instability of c-ZrO_2 and the Resulting Diffusion-Controlled Reactions;" pp. 1-13 in Advances in Ceramics, Vol. 12. Edited by N. Claussen, M. Rühle, and A. H. Heuer. The American Ceramic Society, Inc., Columbus, OH, 1984.

8. E. C. Subbarao, "Zirconia- an Overview;" pp.1-13 in Advances in Ceramics, Vol. 3. Edited by A. H. Heuer and L. W. Hobbs. The American Ceramic Society, Inc., Columbus, OH, 1981.

9. R. D. Shannon, "Revised Effective Ionic Radii and Systematic Studies of Interatomic Distances in Halides and Chalcogenides," *Acta Cryst.*, A**32**, 751-67 (1964).

10. G. M. Wolten, "Direct High-Temperature Single-Crystal Observation of Orientation Relationship in Zirconia Phase Transformation," *Acta Cryst.*, **17**, 763-5 (1964).

11. J. Adam and M. O'Rodgers, "Crystal Structure of ZrO_2 and HfO_2," *Acta Cryst.*, **12** [11] 951 (1959).

12. C. E. Curtis, L. M. Doney, and J. R. Johnson, "Some Properties of Hafnium Oxide, Hafnium Silicate, Calcium Hafnate, and Hafnium Carbonate," *J. Am. Ceram. Soc.*, **37** [10] 458-65 (1954).

13. S. M. Lang, "Axial Thermal Expansion of Tetragonal ZrO_2 Between 1150°C and 1700°C," *J. Am. Ceram. Soc.*, **33**, [5] 274 (1969).

14. P. Duwez and F. Odell, "Phase Relationships in the System Zirconia-Ceria," *J. Am. Ceram. Soc.*, **33**, 274-83 (1950).

15. H. E. Swanson, H. F. McMurdie, M. C. Morris, and E. H. Evans, "Standard X-Ray Diffraction Powder Patterns, Section 7.-Data for 81 Substances," *National Bureau of Standards,* Mono. 25, Sec. 7, Sept. 1969.

16. K. S. Mazdiyasni and L. M. Brown, "Preparation and Characterization of High-Purity $HfTiO_4$," *J. Am. Ceram. Soc.*, **53** [11] 585-9 (1970).

17. L. W. Coughanour, R. S. Roth, and V. A. DeProsse, "Phase Equilibrium Relations in the Systems Lime-Titania and Zirconia-Titania," *J. Res. Natl. Bur. Std.*, **52** [1] 37-42 (1954).

18. J. P. Coutures and J. Coutures, "The System HfO_2-TiO_2," *J. Am. Ceram. Soc.*, **70** [6] 383-7 (1987).

19. F. H. Brown, Jr., and P. Duwez, "The Zirconia-Titania System," *J. Am. Ceram. Soc.*, **37** [3] 129-32 (1954).

20. R. E. Newnham, "Crystal Structure of $ZrTiO_4$," *J. Am. Ceram. Soc.*, **50** [4] 216 (1967).

21. O. M. Stansfield, "Thermal Expansion of Polycrystalline HfO_2-ZrO_2 Solid Solutions," *J. Am. Ceram. Soc.*, **48** [8] 436-7 (1965).

22. R. Ruh, H. J. Garrett, R. F. Domagala, and N. M. Tallan, "The System Zirconia-Hafnia," *J. Am. Ceram. Soc.*, **51** [1] 23-7 (1968).

23. N. A. Godina, E. K. Keler, and V. S. Rudenko, "The Reaction Between Hafnium and Titanium Dioxides," *Rus. J. Inorg. Chem.*, **5** [12] 1349-50 (1960).

24. R. Ruh, G. W. Hollenberg, E. G. Charles, and V. A. Patel, "Phase Relations and Thermal Expansion in the System HfO_2-TiO_2" *J. Am. Ceram. Soc.*, **59** [11-12] 495-9 (1976).

25. A. V. Schevchenko, L. M. Lopato, A. I. Stegny, I. M. Maister, V. S. Dverniakov, and V. V. Passitchny, "Liquidus of the HfO_2-TiO_2 and HfO_2-Eu_2O_3 System," *Dokl. Akad. Nauk SSSR, Ser. A*, **87**, 58-85 (1979).

26. T. Noguchi and M. Mizuno, "Phase Changes in the ZrO_2-TiO_2 System," *Bull. Chem. Soc. Jap.*, **41** [12] 2895-9 (1968).

27. C. E. Holcombe, M. K. Morrow, D. D. Smith, and D. A. Carpenter, "Survey of Low Expanding High Melting Mixed Oxides," Union Carbide Corporation Y-12 Plant Research Report Y-1913, 1974.

28. C. B. Choudhary, H. S. Maiti, and E. C. Subbarao, "Defect Structure and Transport Properties;" pp.1-80 in Solid Electrolytes and Their Applications. Edited by E. C. Subbarao. Plenum Press, New York, 1980.

29. F. A. Kröger and H. J. Vink, "Relations Between the Concentrations of Imperfections in Solids," *J. Phys. Chem. Solids,* **5**, 208-23 (1958).

30. J. Patterson, "Conduction Domains for Solid Mixed Conductors and Electrolytic Domain of Calcia Stabilized Zirconia;" pp. 131-54 in Physics of Electronic Ceramics, Part A. Edited by L. L. Hench and D. B. Dove. Marcel Dekker, Inc., New York, 1971.

31. J. Rudolph, "Mechanism of Conduction in Oxide Semiconductors at High Temperatures, " *Z. Naturforsch. A,* **14** [8] 727-37 (1959).

32. P. Kofstad and D. J. Ruzicka, "On the Defect Structure of ZrO_2 and HfO_2," *J. Electrochem. Soc.,* **110** [3] 181-4 (1963).

33. R. W. Vest, N. M. Tallan, and W. C. Tripp, "Electrical Properties and Defect Structure of Zirconia: I, Monoclinic Phase," *J. Am. Ceram. Soc.,* **47** [12] 635-40 (1964).

34. R. W. Vest and N. M. Tallan, "Electrical Properties and Defect Structure of Zirconia: II, Tetragonal Phase," *J. Am. Ceram. Soc.,* **48** [9] 472-5 (1965).

35. L. A. McClaine and C.P. Coppel, "Electrical Conductivity Studies of Tetragonal Zirconia," *J. Electrochem. Soc.,* **113** [1] 80-5 (1966).

36. A. Kumar, D. Rajdev, and D. L. Douglass, "Effect of Oxide Defect Structure on the Electrical Properties of ZrO_2," *J. Am. Ceram. Soc.,* **55** [9] 439-45 (1972).

37. A. M. Anthony, "High Temperature Refractory Applications of Zirconia;" pp.437-54 in Advances in Ceramics, Vol. 3. Edited by A. H. Heuer and L. W. Hobbs. The American Ceramic Society, Inc., Columbus, OH, 1981.

38. D. L. Douglass and C. Wagner, "Oxidation of Oxygen Deficient Zirconia and Its Relationship to the Oxidation of Zirconium," *J. Electrochem. Soc.,* **113** [7] 671-6 (1966).

39. R. M. Dell and A. Hooper, "Oxygen Ion Conductors;" pp. 291-312 in Solid Electrolytes. Edited by P. Hagenmuller and W. van Gool. Academic Press, New York, 1978.

40. H. J. Rossell, "Ordering in Anion-Deficient Fluorite-Related Oxides;" pp. 47-63 in Advances in Ceramics, Vol. 3. Edited by A. H. Heuer and L. W. Hobbs. The American Ceramic Society, Inc., Columbus, OH, 1981.

41. J. F. Baumard and P. Abelard, "Defect Structure and Transport Properties of ZrO_2-Based Solid Electrolytes;" pp. 555-71 in Advances in Ceramics, Vol. 12. Edited by N. Claussen, M. Rühle, and A. H. Heuer. The American Ceramic Society, Inc., Columbus, OH, 1984.

42. F. A. Kröger, "Electronic Conductivity of Calcia-Stabilized Zirconia," *J. Am. Ceram. Soc.*, **49** [4] 215-8 (1966).

43. M. Kleitz, M. Levy, J. Fouletier, and P. Fabry, "Determination of Electronic Conductivity in ZrO_2-Y_2O_3 by Electrochemical Reduction;" pp. 337-48 in Advances in Ceramics, Vol. 3. Edited by A. H. Heuer and L. W. Hobbs. The American Ceramic Society, Inc., Columbus, OH, 1981.

44. W. L. Worrell and W. Weppner, "Ionic and Electronic Transport Properties of Titania Doped Zirconia Electrolytes," to be published.

45. W. D. Kingery, Property Measurements at High Temperatures. Wiley, New York, 1959.

46. S. C. Carniglia, S. D. Brown, and T. F. Schroeder, "Phase Equilibria and Physical Properties of Oxygen-Deficient Zirconia and Thoria," *J. Am. Ceram. Soc.*, **54** [1] 13-7 (1971).

47. B. Ohnysty and F. K. Rose, "Thermal Expansion Measurements on Thoria and Hafnia to 4500°F," *J. Am. Ceram. Soc.*, **47** [8] 398-400 (1964).

48. L. L. Fehrenbacher and L. A. Jacobson, "Metallographic Observation of the Monoclinic-Tetragonal Phase Transformation in ZrO_2," *J. Am. Ceram. Soc.*, **48** [3] 157-61 (1965).

49. R. N. Patil and E. C. Subbarao, "Axial Thermal Expansion of ZrO_2 and HfO_2 in the Range Room Temperature to 1400°C," *J. Appl. Crys.*, **2**, 281-8 (1969).

50. S. K. Filatov and V. A. Frank-Kamenetskii, "Anomalous Thermal Expansion of ZrO_2 and HfO_2 Over the Range 20-1200°C," *Soviet Phys. Cryst.*, **14** [5] 696-9 (1970).

51. D. W. Stacy, J. K. Johnstone, and D. R. Wilder, "Axial Thermal Expansion of HfO_2," *J. Am. Ceram. Soc.*, **55** [9] 482-3 (1972).

52. S. L. Dole, O. Hunter, Jr., F. W. Calderwood, and D. J. Bray, "Microcracking of Monoclinic HfO_2," *J. Am. Ceram. Soc.*, **61** [11-12] 486-90 (1978).

53. G. V. Samsonov, E. K. Fen', Ya. S. Malakhov, and V. Ya. Malakhov, "Dielectric and Thermophysical Properties of Transition-Metal Oxides," *Izv. Akad. Nauk. SSSR Neorg. Mater.*, **12** [8] 1404-10 (1976).

54. R. Ruh, G. W. Hollenberg, S. R. Skaggs, S. D. Stoddard, F. D. Gac, and E. G. Charles, "Axial and Linear Thermal Expansion of ZrO_2 and HfO_2," *Am. Ceram. Soc. Bull.*, **60** [4] 504-6 (1981).

55. C. E. Curtis, "Development of Zirconia Resistant to Thermal Shock," *J. Am. Ceram. Soc.*, **30** [6] 180-96 (1947).

56. G. A. Carlson, J. L. Anderson, R. A. Briesmeister, S. R. Skaggs, and R. Ruh, "Coefficient of Thermal Expansion and Dynamic Response to Pulsed Energy Deposition in HfO_2-TiO_2 Compositions," *J. Am. Ceram. Soc.*, **60** [11-12] 508-10 (1977).

57. R. W. Lynch and B. Morosin, "Thermal Expansion, Compressibility, and Polymorphism in Hafnium and Zirconium Titanates," *J. Am. Ceram. Soc.*, **55** [8] 409-13 (1972).

58. H. Ikawa, A. Iwai, K. Hiruta, H. Shimojima, K. Urabe, and S. Udagawa, "Phase Transformation and Thermal Expansion of Zirconium and Hafnium Titanates and Their Solid Solutions," *J. Am. Ceram. Soc.*, **71** [2] 120-27 (1988).

59. T. F. Schroeder, "Shock Resistant Ceramics," Rocketdyne Research Report No.: 66-26, Rocketdyne, Canoga Park, CA, 1966.

60. J. J. Gilman, p.240 in The Physics and Chemistry of Ceramics. Edited by C. Klingsberg. Gordon and Breach, New York, 1963.

61. C. E. Inglis, *Transactions of the Institute of Naval Architects*, **55**, Part 1, 219 (1913).

62. A. A. Griffith, "The Phenomena of Rupture and Flow in Solids," *Philosophical Transactions of the Royal Society of London*, **A221**, 163-98 (1921).

63. G. R. Irwin, Fracturing Metals. ASM, Cleveland, Ohio, 1949.

64. A. G. Evans, "Structural Reliability: A Processing Dependent Phenomenon," *J. Am. Ceram. Soc.*, **65** [3] 127-37 (1982).

65. J. P. Singh, "Effect of Flaws on the Fracture Behavior of Structural Ceramics: A Review," *Advanced Ceramic Materials*, **3** [1] 18-27 (1988).

66. R. M. McMeeking and A. G. Evans, "Mechanics of Transformation Toughening in Brittle Materials," *J. Am. Ceram. Soc.*, **65** [5] 242-46 (1982).

67. E. Ryshkewitch, "Compressive Strength of Porous Sintered Alumina and Zirconia-- 9th Communication to Ceramography," *J. Am Ceram. Soc.*, **36** [2] 65-8 (1953).

68. W. Duckworth, "Discussion of Ryshkewitch Paper," *J. Am. Ceram. Soc.*, **36** [2] 68 (1953).

69. F P. Knudsen, "Dependence of Mechanical Strength of Brittle Polycrystalline Specimens on Porosity and Grain Size," *J. Am. Ceram. Soc.*, **42** [8] 376-87 (1959).

70. S. D. Brown, R. B. Biddulph, and P. D. Wilcox, "A Strength-Porosity Relation Involving Different Pore Geometry and Orientation," *J. Am. Ceram. Soc.*, **47** [7] 320-22 (1964).

71. D. P. H. Hasselman, "Analysis of the Strain at Fracture of Brittle Solids with High Densities of Microcracks," *J. Am. Ceram. Soc.*, **52** [8] 458-9 (1969).

72. D. P. H. Hasselman and J. P. Singh, "Analysis of Thermal Stress Resistance of Microcracked Brittle Ceramics," *Am. Ceram. Soc. Bull.*, **58** [9] 856-60 (1979).

73. R. H. Hannick, K. A. Johnston, R. T. Pascoe, and R. C. Garvie, "Microstructural Changes During Isothermal Aging of a Calcia Partially Stabilized Zirconia Alloy;" pp. 116-36 in Advances in Ceramics, Vol. 3. Edited by A. H. Heuer and L. W. Hobbs. The American Ceramic Society, Inc., Columbus, OH, 1981.

74. N. Claussen, "Microstructural Design of Zirconia-Toughened Ceramics (ZTC);" pp. 325-51 in Advances in Ceramics, Vol. 12. Edited by N. Claussen, M. Rühle, and A. H. Heuer. The American Ceramic Society, Inc., Columbus, OH, 1984.

75. D. Michel, L. Mazerolles, and M. Perez y Jorba, "Polydomain Crystals of Single Phase Tetragonal ZrO_2; Structure, Microstructure, and Fracture Toughness;" pp. 131-8 in Advances in Ceramics, Vol. 12. Edited by N. Claussen, M. Rühle, and A. H. Heuer. The American Ceramic Society, Inc., Columbus, OH, 1984.

76. M. V. Swain and R. H. J. Hannik, "R-Curve Behavior in Zirconia Ceramics;" pp. 225-39 in Advances in Ceramics, Vol. 12. Edited by N. Claussen, M. Rühle, and A. H. Heuer. The American Ceramic Society, Inc., Columbus, OH, 1984.

77. N. Claussen and M. Rühle, "Design of Transformation Toughened Ceramics;" pp. 137-63 in Advances in Ceramics, Vol. 3. Edited by A. H. Heuer and L. W. Hobbs. The American Ceramic Society, Inc., Columbus, OH, 1981.

78. M. Rühle, N. Claussen, and A. H. Heuer, "Microstructural Studies of Y_2O_3-Containing Tetragonal ZrO_2 Polycrystals (Y-TZP);" pp. 352-70 in Advances in Ceramics, Vol. 12. Edited by N. Claussen, M. Rühle, and A. H. Heuer. The American Ceramic Society, Inc., Columbus, OH, 1984.

79. M. Matsui, T. Soma, and I. Oda, "Effect of Microstructure on the Strength of Y-TZP Components;" pp.371-81 in Advances in Ceramics, Vol. 12. Edited by N. Claussen, M. Rühle, and A. H. Heuer. The American Ceramic Society, Inc., Columbus, OH, 1984.

80. K. Tsukuma, Y. Kubota, and T. Tsukidate, "Thermal and Mechanical Properties of Y_2O_3-Stabilized Tetragonal Zirconia Polycrystals;" pp. 382-90 in Advances in Ceramics, Vol. 12. Edited by N. Claussen, M. Rühle, and A. H. Heuer. The American Ceramic Society, Inc., Columbus, OH, 1984.

81. R. P. Ingel, D. Lewis, B. A. Bender, and R. W. Rice, "Physical, Microstructural, and Thermomechanical Properties of ZrO_2 Single Crystals;" pp. 408-14 in Advances in Ceramics, Vol. 12. Edited by N. Claussen, M. Rühle, and A. H. Heuer. The American Ceramic Society, Inc., Columbus, OH, 1984.

82. O. Hunter, Jr., R. W. Schneidecker, and S. Tojo, "Characterization of Metastable Tetragonal Hafnia," *Ceramurgia International,* **5** [4] 137- 42 (1979).

83. R. P. Ingel, D. Lewis, B. A. Bender, and R. W. Rice, "Initial Characterization of Partially Stabilized HfO_2 Single Crystals," *Cer. Eng. Sci. Proc.,* **3** [9-10] 577-86 (1982).

84. R. G. Hoagland, C. W. Marschall, A. R. Rowenfield, G. Hollenberg, and R. Ruh, "Microstructural Factors Influencing Fracture Toughness of Hafnium Titanate," *Mater. Sci. Eng.,* **15**, 51-62 (1974).

85. U. Dworak, H. Olapinski, D. Fingerle, and U. Krohn, "ZrO_2 Ceramics for Internal Combustion Engines;" pp.480-7 in Advances in Ceramics, Vol. 12. Edited by N. Claussen, M. Rühle, and A. H. Heuer. The American Ceramic Society, Inc., Columbus, OH, 1984.

86. A. G. Evans, "Fracture Mechanics Determinations;" pp. 17-48 in Fracture Mechanics of Ceramics, Vol. 1. Edited by R. C. Bradt, D. P. H. Hasselman, and F. F. Lange. Plenum Press, New York, 1973.

87. G. D. Quinn, F. I. Baratta, and J. A Conway, "Commentary on U.S. Standard Test Method for Flexural Strength of High Performance Ceramics at Ambient Temperature," Army Materials and Mechanics Research Center, TR 85-21, 1-11 August 1985.

88. P. Kenny, "The Application of Fracture Mechanics to Cemented Tungsten Carbides," *Powder Metallurgy,* **14** [27] 22-38 (1971).

89. A. G. Evans and A. Charles, "Fracture Toughness Determinations by Indentation," *J. Am. Ceram. Soc.,* **59** [7-8] 371-2 (1976).

90. J. J. Petrovic and M. G. Mendiratta, "Fracture from Controlled Surface Flaws;" pp. 83-102 in Fracture Mechanics Applied to Brittle Materials. Edited by S. W. Freiman. Am. Soc. Test. Mater. Spec. Tech. Publ., No. 678, Philadelphia, PA, 1979.

91. R. H. Marion, "Use of Indentation Fracture to Determine Fracture Toughness;" pp. 103-11 in Fracture Mechanics Applied to Brittle Materials. Edited by S. W. Freiman. Am. Soc. Test. Mater. Spec. Tech. Publ., No. 678, Philadelphia, PA, 1979.

92. A. G. Evans, "Fracture Toughness: The Role of Indentation Technique;" pp. 112-35 in Fracture Mechanics Applied to Brittle Materials. Edited by S. W. Freiman. Am. Soc. Test. Mater. Spec. Tech. Publ., No. 678, Philadelphia, PA, 1979.

93. B. R. Lawn and D. B. Marshall, "Hardness, Toughness and Brittleness," *J. Am. Ceram. Soc.*, **62** [7-8] 347-50 (1979).

94. G. R. Anstis, P. Chantikul, B. R. Lawn, and D. B. Marshall, "A Critical Evaluation of Indentation Techniques for Measuring Fracture Toughness: I, Direct Crack Measurements," *J. Am. Ceram. Soc.*, **64** [9] 533-8 (1981).

95. P. Chantikul, G. R. Anstis, B. R. Lawn, and D. B. Marshall, "A Critical Evaluation of Indentation Techniques for Measuring Fracture Toughness: II, Strength Method," *J. Am. Ceram. Soc.*, **64** [9] 539-4 (1981).

96. D. B. Marshall and A. G. Evans, "Reply to "Comment on 'Elastic/Plastic Indentation Damage in Ceramics: The Median/Radial Crack System'"," *Comm. Am. Ceram. Soc.*, **64**, C182-C183 (1981).

97. B. R. Lawn, "The Indentation Crack as a Model Surface Flaw;" pp. 1-25 in Fracture Mechanics of Ceramics, Vol. 5. Edited by R. C. Bradt, A. G. Evans, D. P. H. Hasselman, and F. F. Lange. Plenum Press, New York, 1983.

98. D. B. Marshall, "Controlled Flaws in Ceramics: A Comparison of Knoop and Vickers Indentation," *J. Am. Ceram. Soc.*, **66** [2] 127-31 (1983).

99. R. F. Cook and B. R. Lawn, "A Modified Indentation Toughness Technique," *Comm. Am. Ceram. Soc.*, **66**, C200-C201 (1983).

100. R. F. Domagala and R. Ruh, "The Hafnium-Oxygen System," *Trans. of ASM*, **58**, 165-75 (1965).

101. E. G. Rauh and S. P. Garg, "The ZrO_{2-x} (cubic)-ZrO_{2-x} (cubic + tetragonal) Phase Boundary," *J. Am. Ceram. Soc.*, **63** [3-4] 239-40 (1980).

102. G.M. Wolten, "Diffusionless Phase Transformations in Zirconia and Hafnia," *J. Am. Ceram. Soc.*, **46** [9] 418-22 (1963).

103. M. Rühle and A. H. Heuer, "Phase Transformations in Zirconia-Containing Ceramics: II, The Martensitic Reaction in t-ZrO_2;" pp. 14-32 in Advances in Ceramics, Vol. 12. Edited by N. Claussen, M. Rühle, and A. H. Heuer. The American Ceramic Society, Inc., Columbus, OH, 1984.

104. S. Dowdy and S. Wearden, Statistics for Research. John Wiley and Sons, New York, 1983.

VITA

Paul Russell Staszak was born in Chicago, Illinois on February 21, 1960. He received a B.S. degree in 1982 and an M.S. degree in 1985 from the University of Illinois at Urbana-Champaign in Ceramic Engineering. He served as both a research and teaching assistant during his graduate career at the University of Illinois. His teaching duties included laboratory courses in ceramic x-ray analysis and glass. His graduate research work included studies of the structure of germanate glasses and high temperature ceramics. He also spent two summers as a student research assistant at Argonne National Laboratory working on the laser pyrolysis of amorphous metal powders. He has two publications, one on his work with laser pyrolysis, the other on a space group calculation of magnesium spinel.